Simulating Population III star formation

by

Lewis Prole

A Thesis submitted to Cardiff University
for the degree of Doctor of Philosophy

February 2023

Abstract

This thesis covers a number of numerical experiments exploring the first generation of Population III star formation. After briefly reviewing the field to date, we present a resolution test for primordial gas. We find that the gas fragments to a higher degree as the resolution of the simulations is increased, leading to lower mass stars than predicted by previous, lower resolution studies. A number of stars are ejected with masses capable of surviving until the present day, providing targets for observations. We continue to present a study exploring the effects of primordial magnetic fields on Population III star formation, finding that the small-scale, tangled fields are incapable of providing support against fragmentation or significantly altering the collapse. Lastly, we present the results of cosmological zoom-in simulations around halos exposed to Lyman-Werner (LW) radiation. While the LW fields result in higher halo masses, it has little effect on the Pop III IMF. The primordial IMF therefore likely remains constant during the transition from pure Pop III.1 stars to the Pop III.2 stars that form in the presence of their radiation.

Publications

First Author Publications

Prole, L. R., Clark, P. C., Klessen, R. S., Glover, S. C. (2022). Fragmentation-induced starvation in Population III star formation: a resolution study. Monthly Notices of the Royal Astronomical Society, 510(3), 4019-4030.

Prole, L. R., Clark, P. C., Klessen, R. S., Glover, S. C., Pakmor, R. (2022). Primordial magnetic fields in Population III star formation: a magnetized resolution study. Monthly Notices of the Royal Astronomical Society, 516(2), 2223-2234.

Prole, L. R., Schauer, A. T., Clark, P. C., Glover, S. C., Priestley, F. D., Klessen, R. S. (2023). From dark matter halos to pre-stellar cores: High resolution follow-up of cosmological Lyman-Werner simulations. Monthly Notices of the Royal Astronomical Society, 520, 2081-2093.

Contents

Acknowledgements

Funding Bodies and Affiliations

The work performed during this PhD was funded by the Science and Technology Facilities Council (STFC) as part of UK Research and Innovation (UKRI).

This work used the DiRAC@Durham facility managed by the Institute for Computational Cosmology on behalf of the STFC DiRAC HPC Facility (www.dirac.ac.uk). The equipment was funded by BEIS capital funding via STFC capital grants ST/P002293/1, ST/R002371/1 and ST/S002502/1, Durham University and STFC operations grant ST/R000832/1. DiRAC is part of the National e-Infrastructure.

The authors gratefully acknowledge the Gauss Centre for Supercomputing e.V. (www.gauss-centre.eu) for supporting this project by providing computing time on the GCS Supercomputer SuperMUC at Leibniz Supercomputing Centre (www.lrz.de).

We also acknowledge the support of the Supercomputing Wales project, which is part-funded by the European Regional Development Fund (ERDF) via Welsh Government.

RSK and SCOG acknowledge support from the Deutsche Forschungsgemeinschaft (DFG, German Research Foundation) via the collaborative research center (SFB 881, Project-ID 138713538) "The Milky Way System" (subprojects A1, B1, B2 and B8). They also acknowledge support from the Heidelberg Cluster of Excellence "STRUCTURES" in the framework of Germany's Excellence Strategy (grant EXC-2181/1, Project-ID 390900948) and from the European Research Council (ERC) via the ERC Synergy Grant "ECOGAL" (grant 855130).

We thank the referee of Prole et al. (2022a), Dr Christopher F. McKee, for recommendations that improved the manuscript.

Personal Thanks

I would like to thank my supervisor Dr Paul Clark for the inspiration for the projects covered in this thesis, as well as support throughout the PhD. I would also like to thank my collaborators during these projects, namely Anna T. P. Schauer, Simon C. O. Glover, Felix D. Priestley and Ralf S. Klessen.

Additionally, I would like to thank my family and friends for their continued support throughout my research career.

Chapter 1

Introduction

1.1 Motivation and outline

The *Cosmic Dark Ages* ended with the formation of the first generation of stars, known as Population III (Pop III) stars, at $z \sim 15$. In a cold dark matter model (ΛCDM) Universe, the formation of Pop III stars began with hierarchical structure formation, starting with the formation of low mass, dark matter (DM) halos (Couchman & Rees, 1986), at $z \sim 20$. Baryonic gas collapsed inside the DM potential well to form stellar cores. These stars impacted the Universe around them in many ways; their UV radiation heated and ionised the interstellar medium (ISM) around them (Bromm et al., 2001) at the epoch of *Reionisation*; the ISM was enriched with heavy elements for the first time when Pop III stars died as supernovae (Heger et al., 2003), directly effecting the composition of the next generation (Pop II) of stars; radiative feedback from Pop III stars may have given rise to the formation of direct collapse black holes (DCBHs) responsible for high redshift quasar observations (e.g. Regan et al. 2014); and finally the small-scale, tangled magnetic field present in the early Universe began its transformation into into the large-scale galactic magnetic field observed today during the formation of Pop III stars (e.g. Schober et al. 2015).

Despite their impact on the future of the Universe, there have been no observations of Pop III stars to date as the flux they produce is below the reachable limit with deep James Webb Space Telescope (JWST) imaging (Schauer et al., 2020; Merlin et al., 2022; Zackrisson et al., 2011). Their study is thus largely confined to numerical work. Through decades of Pop III research, the field has advanced from 1-dimensional calculations and one-zone models to fully 3-dimensional numerical simulations with live chemistry prescriptions and feedback mechanisms. The lack of observational evidence for Pop III stars is subject to change with the recent launch of the JWST through potential observations of gravitationally lensed Pop III galaxies (e.g. Vikaeus et al. 2022)

and supernova explosions (e.g. Whalen et al. 2013a,b; Smidt et al. 2015). The need for numerical predictions of Pop III characteristics (mass, accretion rate, luminosity ect.) is therefore crucial to guide future observational research in the early Universe.

Although considerable numerical work in the field has already been performed, a number of problems need to be addressed. Firstly, inconsistencies in the resolution employed in Pop III simulations has lead to discrepancies in the produced initial mass function (IMF). While it was originally proposed that a single, massive star formed at the center of each halo (Bromm et al., 1999; Haiman et al., 1996a), more recent investigations have found that primordial gas fragments to give a group of lower mass stars (Greif et al., 2011b; Smith et al., 2011; Clark et al., 2011a; Susa et al., 2014; Stacy et al., 2016; Wollenberg et al., 2019). However, as the resolution of these studies varies, the IMFs they produce do not agree. This warrants further investigation into the appropriate resolution to use when simulating Pop III star formation.

Furthermore, recent studies reveal that unlike present-day magnetic fields, the magnetic fields present in the early Universe were small-scale in nature due to a process known as the small-scale turbulent dynamo (Schober et al., 2012a, 2015; Federrath et al., 2011a). As the effects of these fields on Pop III star formation are largely unexplored, this also requires investigation.

Lastly (with respect to the work presented in this thesis), cosmological simulations have revealed that the required mass of primordial halos to form stars increases with the intensity of an external Lyman-Werner radiation field expected to be emitted by Pop III stars. As current cosmological simulations lack the resolution required to resolve star formation, follow-up simulations must be performed to investigate what knock on effects this has on the primordial IMF.

This thesis details a number of numerical experiments designed to further our knowledge on star formation in the early Universe. The main goals of the work presented here are to:

- Establish a resolution criteria for simulations in primordial chemistry set-ups.
- Assess the necessity of the inclusion of magnetic fields in Pop III star formation simulations.
- Investigate to what extent feedback from the first generation of stars affects ongoing star formation.

The structure of the thesis is as follows. An overview of present-day star formation will be given in Section 1.2 before shifting the discussion towards the primordial Universe in Section 1.3. The numerical techniques of simulation codes are discussed in Chapter 2 before the original work of this thesis is presented as 4 chapters; firstly, a resolution study in Chapter 3; a series of numerical tests involving magnetic fields in Chapter 4; a magnetised resolution study in Chapter 5;

and finally a chapter focused on high resolution, follow-up simulations of cosmological simulations in Chapter 6. A summary of the work covered in this thesis and future planned work is provided in Chapter 7.

1.2 Present-day star formation

While most of this thesis will focus on primordial star formation, this section will briefly cover a more general understanding of star formation in the setting of the present-day Universe. Much of the following is directly applicable to Pop III star formation, and the differences will serve as comparisons in later sections.

Today's Universe is filled with young spiral type galaxies which emit strongly in the optical and ultra-violet (UV) and older elliptical galaxies which emit in the infrared. The emission from these galaxies is largely due to the type of stars within them, with *bluer* spiral galaxies containing more massive young stars and *redder* ellipticals containing older low mass stars. The emission from stars depends on their mass, composition and age. Galaxies are threaded with large scale magnetic fields and typically have a massive black hole at their centre which can shape their evolution radiatively as an active galactic nucleus (AGN).

The composition of the Universe started out as mainly hydrogen and helium, but the various generations of stars that followed produced heavy elements or *metals* and dispersed them throughout the ISM when they exploded as supernovae. Supernova events also produce dust made from silicates and carbonaceous materials, which absorb light at shorter wavelengths i.e. optical-UV and re-emits it in the infrared (see Draine 2003) and has an important role in planet formation.

1.2.1 Formation and emission

Stars typically form in over-dense regions of supersonically turbulent, gravitationally bound giant molecular clouds (GMCs) (Larson, 1981). Gravitational collapse of isothermal gas is centrally concentrated, the density profile goes as $\rho \propto r^{-2}$ where r is the radius from the center of collapse (Larson, 1969). The central region gets denser until the gas becomes optically thick to dust emission at densities around 10^{-13} g cm^{-3}, above which the temperature rises to give a hydrostatic equilibrium, known as the 'first core'. The core accretes mass from the surroundings adiabatically until it reaches $\sim 10^{-8}$ g cm^{-3}, at which point the temperature reaches ~ 1800 K and hydrogen molecules begin to dissociate, causing the collapse to continue. This ends when all the hydrogen becomes atomic and the 'stellar core' forms at $\sim 10^{-4}$ g cm^{-3}.

Once the dense core begins to generate thermal energy through nuclear fusion, it takes its place on the main sequence of stars. The IMF is the probability distribution for the mass of stars as they enter the main sequence. The standard IMF for present-day star formation consists of a three-part power law of the form

$$\frac{dN_\star}{d\ \ln(m_\star)} \propto m_\star^{-a}. \tag{1.1}$$

where $N_\star$ is the number of stars per stellar mass interval in log space $\ln(m_\star)$. From Kroupa (2001), from 0.01 - 0.08$M_\odot$, $a = -0.7$, which switches to $a = 0.3$ for 0.08 - 0.5$M_\odot$ and again switches to $a = 1.3$ for 0.5 - 50$M_\odot$. There may be an upper limit to stellar mass at ~ 150 $M_\odot$ (e.g. Elmegreen 2000) set by the Eddington luminosity i.e. if the radiation pressure generated by the star exceeds the force of gravity, it will begin to shed its outer layers.

The emission from stars consists of a black body spectra with different absorption lines for different spectral types. For stars on the main sequence, higher stellar masses produce higher luminosities, which correspond to higher surface temperatures T_s through

$$L = 4\pi R^2 \sigma_B T_s^4, \tag{1.2}$$

where σ_B is the Stefan-Boltzmann constant and R is the stellar radius. Main sequence stars are classified by their surface temperatures into 7 main classes. From highest T_s to lowest, the classes are O, B, A, F, G, K and M. Higher surface temperatures shift the peak of the emission spectrum to shorter wavelengths (higher frequencies) as

$$\lambda_{\rm peak} = 2.9 \times 10^{-3} T_s, \tag{1.3}$$

so for main sequence stars, higher masses yield higher surface temperatures and produce a higher flux of high frequency, ionising radiation.

1.2.2 Discs

An important factor when considering the IMF in both present day and primordial star formation is disc fragmentation around the primary star and the subsequent formation of secondary stars. A gravitational collapse often results in the formation of a central dense object surrounded by a rotating disc which facilitates accretion onto the object. Neglecting self-gravity, the disc rotation at distance R from a central object of mass M is Keplerian, where the angular velocity is

$$\Omega_{\rm K} = \sqrt{\frac{GM}{R^3}}, \tag{1.4}$$

where G is the gravitational constant. However, this is not the case if the disc is self gravitating. Assuming the disc gravitational field dominates over the central object (e.g. Mestel 1963), the

angular velocity goes as

$$\Omega_\theta \propto \frac{1}{R}. \tag{1.5}$$

In order for the disc gravity to be comparable to that of the central object, the disc mass must be of the order of the central object (Bertin & Lodato, 1999). When $M_{\rm disc} << M_{\rm central}$, the Keplerian approximation applies. However, if the disc temperature is high enough, pressure forces in the disc can significantly alter the rotation.

The fragmentation of discs can result in the formation of binaries or multiple systems. For a disc in hydrostatic balance i.e. gravity and pressure are balanced in the vertical axis of the disc, the solution for stability against self-gravity is summarised in Lodato (2007). The thickness of non-self-gravitating and self-gravitating discs are

$$H_{\rm nsg} = \frac{c_{\rm s}}{\Omega_{\rm K}}, \tag{1.6}$$

$$H_{\rm sg} = \frac{c_{\rm s}^2}{\pi G \Sigma}, \tag{1.7}$$

respectively, where $v_{\rm K}$ is the Keplerian rotational velocity and Σ is the surface density of the disc. Discs are therefore affected by self-gravity if

$$Q = \frac{H_{\rm sg}}{H_{\rm nsg}} = \frac{c_{\rm s}\Omega_{\rm K}}{\pi G \Sigma} \sim 1, \tag{1.8}$$

where Q is the Toomre parameter (Toomre, 1964). The same result is achieved through linear perturbation analysis of conserved quantities (see Section 1.2.3) for tightly wound perturbations, giving a velocity dispersion where the outcome depends on the square of the frequency of the perturbation ω^2. For positive ω^2 the perturbation propagates as a wave, while for negative ω^2 an exponentially growing gravitational instability occurs, with the most unstable perturbation wavelength being of the order of the disc thickness. This corresponds to an instability condition of

$$Q < 1. \tag{1.9}$$

In the disc, pressure terms act to stabilise against gravitational instability at small spatial scales, while rotation acts to support at larger spatial scales. In general, the disc remains stable if the thermal pressure and shear force of the differential rotation overcome the force of gravity. Combining equations 1.8 and 1.9 we see that if the accretion rate onto the disc is higher than its ability to transfer the mass inwards, Σ increases and instability occurs. Even with no accretion onto the disc, instability can occur if the cooling timescale is shorter than the orbital time, as the sound speed decreases as the gas cools (Gammie, 2001).

Viscosity between the differentially rotating annuli of the disc transfer angular momentum outwards to slower regions and the loss of energy causes the gas to move to a smaller orbit. The lost gravitational potential energy is dissipated as heat and radiated away. The viscosity is parameterised by a dimensionless parameter α (e.g. Shakura & Sunyaev 1973; King et al. 2007) specifying the local rate that angular momentum is transported. If the value of α was set by collisions within the gas, the viscous timescale (the timescale for disc surface density to change) would be too long to transfer sufficient angular momentum. However, this allows for a high ratio of viscous to dynamical timescales i.e. a high Reynolds number. As gas with high Reynolds numbers is subject to non-laminar (turbulent) motions, viscosity can be caused by the mixing of fluid in the disc due to turbulence (Pringle, 1981), giving a higher effective α.

1.2.3 Fluid dynamics

A powerful tool to investigate star formation and other processes in the ISM is to model the gas with a set of equations that allow its dynamics to be simulated numerically. The Euler equations are conservation laws for mass, momentum and energy that take the form of a system of hyperbolic partial differential equations. Matter entering or leaving an arbitrary volume V through surface S via unit normal surface vector $\vec{n}$ has at the mass flux at the surface $\rho\vec{v}$, where ρ is the density of the matter and $\vec{v}$ is its velocity. If this inflow/outflow is the only cause of mass variation within V, the rate of change of mass within V is

$$\frac{\delta}{\delta t}\int \rho dV = -\int \rho\vec{v}\cdot\vec{n}dS. \tag{1.10}$$

This is re-arranged using Gauss's theorem to

$$\frac{\delta}{\delta t}\int \rho dV = -\int \bigtriangledown\cdot(\rho\vec{v})dV, \tag{1.11}$$

which is true for any arbitrary surface, so

$$\frac{\delta\rho}{\delta t} = -\bigtriangledown\cdot(\rho\vec{v}). \tag{1.12}$$

This is known as the continuity equation, and governs the changes in density due to inflowing/outflowing mass. Similar logic can be applied to derive the equations conserving momentum

$$\frac{\delta(\rho\vec{v})}{\delta t} = -\bigtriangledown\cdot(\rho\vec{v}\vec{v_i}) + \bigtriangledown P \tag{1.13}$$

where P is the pressure applied to the surface of the volume and i donates the component of the velocity parallel with $\vec{n}$. If the force of gravity is present, this becomes

$$\frac{\delta(\rho\vec{v})}{\delta t} = - \bigtriangledown \cdot(\rho\vec{v}\vec{v_i}) + \bigtriangledown P - \rho\frac{\delta\Phi}{\delta x_i} \tag{1.14}$$

where Φ is the gravitational potential. Lastly, by considering the inflow/outflow of kinetic and thermal energy, the energy equation can be derived as

$$\frac{\delta}{\delta t}[\rho(e + \frac{1}{2}v^2)] = - \bigtriangledown \cdot(\rho e + \frac{1}{2}v^2 + P)\vec{v} \tag{1.15}$$

where e is the thermal specific energy. For a more detailed derivation and description of the Euler equations, see Choudhuri (1998). For adiabatic gas e.g. within the first core and within a protostar, the energy equation can be replaced with

$$\frac{d}{dt}\left(\frac{P}{\rho^\gamma}\right) = 0, \tag{1.16}$$

where γ is the ratio of specific heats usually taken as 5/3. For an ideal gas, the temperature, density and pressure are related through the ideal gas law

$$P = \frac{k_B T\rho}{\mu m_p}, \tag{1.17}$$

where k_B, μ and m_p are the Boltzmann's constant, mean molecular weight and mass of a proton (e.g. Laugier & Garai 2007).

When a fluid is perturbed, the disturbance propagates as a wave at the sound speed of the fluid

$$c_s = \sqrt{\frac{P}{\rho}}. \tag{1.18}$$

In supersonic gas, shock fronts build up because the perturbations cannot propagate fast enough. For more detail on shocks, see Clarke & Carswell (2007).

Within a gravitational field, there exists a perturbation scale

$$\lambda_J = \sqrt{\frac{\pi c_s^2}{G\rho}}, \tag{1.19}$$

above which the solution changes from a propagating wave to an exponential growth of the perturbation. This scale is known as the Jeans length, above which gravitational instability occurs.

Magneto-hydrodynamics

The inclusion of magnetic fields in magneto-hydrodynamic (MHD) simulations is important as they change the way that perturbations are advected within a charged fluid or *plasma*. As explained in Choudhuri (1998), fluid with a current density within a electromagnetic field experiences the Lorentz force

$$m\frac{d\vec{v}}{dt} = q(\vec{E} + \vec{v} \times \vec{B}), \tag{1.20}$$

where $\vec{E}$ and $\vec{B}$ are the electric and magnetic field strengths. For a charged particle within a uniform magnetic field, the component of its velocity parallel to the magnetic field will be unaffected by the magnetic field, while the component perpendicular causes the particle to move in circular motion around a central point, resulting in a helical path. Interestingly, if an external force $\vec{F}$ is applied perpendicular to $\vec{B}$, the changes in motion as the forces move in and out of alignment causes the bulk motion of the particle to drift in a direction perpendicular to both $\vec{F}$ and $\vec{B}$. For example, if the field lines are curved with some radius of curvature $\vec{\mathrm{R}_\mathrm{c}}$ and the particle follows along the field line, its centrifugal force acts perpendicular to the field line, causing a drift perpendicular to $\vec{B}$ and $\vec{\mathrm{R}_\mathrm{c}}$.

The addition of a magnetic field adds additional terms to the momentum equation

$$\frac{\partial(\rho\vec{v})}{\partial t} = \rho F_i - \frac{\partial}{\partial x_i}(P_{ij} + \frac{B^2}{8\pi}\delta_{ij} - \frac{\vec{B}_i\vec{B}_j}{4\pi}). \tag{1.21}$$

The last two terms on the right hand side represent an isotropic outwards pressure $B^2/8\pi$ and an inwards tension aligned with the magnetic field $B_iB_j/4\pi$. Completing the dynamical theory is the induction equation

$$\frac{\partial\vec{B}}{\partial t} = \nabla \times (\vec{v} \times \vec{B}) + \lambda\nabla^2\vec{B}, \tag{1.22}$$

where

$$\lambda = \frac{1}{\mu\sigma} \tag{1.23}$$

is the magnetic diffusivity (a measure of the tendency of the magnetic field to diffuse through a conducting medium), μ is the permiability of free space (a measure of the magnetization that a material obtains in response to an applied magnetic field) and σ is the electrical conductivity (a material's ability to conduct electric current). The magnetic Reynolds number is defined as

$$\Re_M = \frac{Lv}{\lambda} \tag{1.24}$$

where L is the length characteristic of the plasma's structure and v is the plasma velocity. In most astrophysical settings with large L and low λ, $\Re_M > 1$. Ideal MHD covers this limit of a zero resistivity plasma, where Equation 1.22 can be replaced with

$$\frac{\partial \vec{B}}{\partial t} = \nabla \times (\vec{v} \times \vec{B}). \tag{1.25}$$

Within this limit, Alfvén (1942) showed that

$$\frac{d}{dt} \int \vec{B} \cdot dS = 0, \tag{1.26}$$

i.e. that magnetic fields deform with the movement of a plasma, a phenomenon known as *flux freezing*. As a consequence of flux freezing, if a column of plasma is bent, twisted or distorted, the magnetic field lines through the column will bend, twist or distort with it. Two points connected by a field line will remain connected by the field line, so when a cloud of gas collapses, the magnetic flux through the cloud remains constant, amplifying the magnetic field as the surface area decreases. Upon perturbing an ideal MHD plasma, the disturbance propagates as two waves. The first is called the *Alfven wave*, where the disturbance acts transverse to the wave direction, and moves parallel to the field line as a non compressive wave at the *Alfven speed*

$$v_a = \frac{B}{\sqrt{4\pi\rho}}, \tag{1.27}$$

driven by magnetic tension attempting to oppose the displacement. The second wave is split into *fast* and *slow magnetoaccoustic waves*. These waves are longitudinal and compressive, with the fast wave propagating perpendicular to the field lines, while the slow wave propergates parallel to the field.

The role of flux freezing is important in transferring angular momentum during a gravitational collapse. From *Ferraro's law of isorotation* (Ferraro, 1937), a rotating cloud with symmetry around the axis of ration in a uniform poloidal magnetic field can only be in a steady state if angular velocity is constant along the magnetic field lines. When the angular velocity is lower outside of the cloud, the field lines are distorted, creating toroidal field lines from the initially poloidal field. Magnetic tension acts to correct the distortion by transferring angular momentum to the slower regions, which is known as *magnetic braking*. Angular momentum can also be removed by jets. Blandford & Payne (1982) developed a hydro-magnetic jet model in which centrifugal forces drive the plasma out of the accretion disc and along magnetic field lines if they make an angle with the disc less than 60°. In this model, field lines are initially poloidal and frozen into the disc. The inertia of the gas above the disc bends the field lines into an increasingly toroidal field. The magnetic stress associated with the twisting forces then causes the outflow to

become collimated, where the final shape of the magnetic structure is determined by an equilibrium between the inward magnetic hoop stress and the outward magnetic pressure. Lynden-Bell (1996) explained that this 'pinching' effect is caused by the concentration of an external pressure by the toroidal field.

1.2.4 MHD in present-day star formation

The galactic magnetic field is uniform over the scales involved in star formation, so numerical work uses uniform magnetic fields in their initial conditions (e.g. Machida et al. 2005; Price & Bate 2007; Hennebelle & Fromang 2008; Hennebelle et al. 2011; Bürzle et al. 2011a,b; Machida 2014). Initial numerical calculations including MHD found that magnetic braking was so efficient at removing angular momentum from the system that rotationally supported Keplerian discs could not form in the presence of realistic magnetic fields. This was known as the *magnetic braking catastrophe*. Studies found that too much angular momentum was transferred away by outflows (Allen et al., 2003), magnetic braking disrupted rotationally supported discs (Mellon & Li, 2008) and that mass-to-flux ratios lower than 3 prevented disc formation (Hennebelle & Ciardi, 2009). This so-called magnetic braking catastrophe was overcome when simulations began to include turbulence in their initial conditions. Seifried et al. (2013) showed that the disordered field structure around the disc due to the turbulent motions prevents an effective coupling between regions close to the disc and the outer regions, reducing magnetic braking efficiency and allowing rotationally supported discs to form. Similarly, Wurster et al. (2019) showed that angular momentum required for disc formation originates from the turbulent velocity of the gas, and that any hindrance of disc formation by magnetic braking is relatively weak.

Magnetic fields can provide support against fragmentation of the gas in star forming regions (Machida et al., 2005; Price & Bate, 2007; Hennebelle et al., 2011; Bürzle et al., 2011a). For example, Machida et al. (2005) used three-dimensional MHD nested grid simulations to determine criteria for fragmentation in the first core. They varied the initial magnetic field strength B and angular momentum Ω of a molecular cloud and found that the outcome depended on the ratio of B/Ω, with magnetically dominated models forming one central object and rotation dominated models fragmenting. They also found that rotation models featured outflows from the core.

Magnetic outflows are produced in simulations with initially uniform magnetic fields. For example, Hennebelle & Fromang (2008) tested various magnetic field strengths threaded through the rotational axis of a supercritical cloud using a barotropic equation of state suitable for the initial isothermal collapse. They found that differential motions amplified radial and toroidal components of the magnetic field. For weak fields, a centrifugally supported disc was formed, and the rotation caused a magnetic tower to form, accompanied by an outflow. For stronger fields,

collapse instead occurred along the field lines, delivering less angular momentum to the centre, and strong magnetic braking extracted further angular momentum from the disc, resulting in no centrifugally supported disc being formed. An outflow emerged, initially at $\sim$45° from the disc, which quickly collimated, which they attributed to the magneto-centrifugal ejection model of Blandford & Payne (1982). A follow-up investigation by Bürzle et al. (2011b) confirmed that a $\sim$1.9 km s^{-1} outflow was indeed ejected from the disc after the formation of the first core within regions of strong toroidal magnetic field ($B_{toridal}/B_{poloidal} > 1$).

While this low velocity bipolar outflow is expected at the formation of the first core, numerical simulations predict a second high velocity outflow at the formation of the pre-stellar core. For example, Machida (2014) used a barotropic equation of state $P \propto \rho^{\gamma}$ (varying the polytropic exponent γ for different density regimes) to solve resistive MHD equations (non-ideal MHD). After producing the low velocity outflow around the first core, a second high-velocity (>10 km s^{-1}) collimated jet emerged around the pre-stellar core. Figure 1.1 shows the toroidal field structure responsible for the outflows as well as the evolution of the disc structure at the times of the low velocity outflow and collimated jet. Ohmic dissipation had dispersed the magnetic field and decoupled the field from the neutral gas inside the first core, allowing magnetic field lines around the second core to straighten. This caused a large magnetic pressure gradient in the region between outflow and inflow, which was speculated to be the driving mechanism of the jet. The high-velocity jet propagated into the low-velocity outflow, transferring momentum to the outflow and increasing its velocity. The weakened jet then proceeded to appear intermittently while embedded in the steadily driven lower velocity outflow. The mass and momentum of the outflow was shown to be much greater than that of the high velocity jet, showing that the outflow is more important at removing infalling gas than the high-velocity jet.

1.2.5 Radiative transfer

Before exploring the effects of stellar radiation on the surrounding ISM, it is important to understand how radiation interacts and transfers within the ISM. The following will briefly cover the emission and absorption of photons by molecules and atoms and how the intensity changes along beams of radiation as it travels.

Spectral lines

Bound-bound transitions result in spectral lines. When an atom or molecule is excited to a higher energy level via a collision or photon absorption, or de-excited via collisions or photon emission, it results in a discrete change in energy of frequency $h\nu = E_m - E_n$, where m and n are the energy

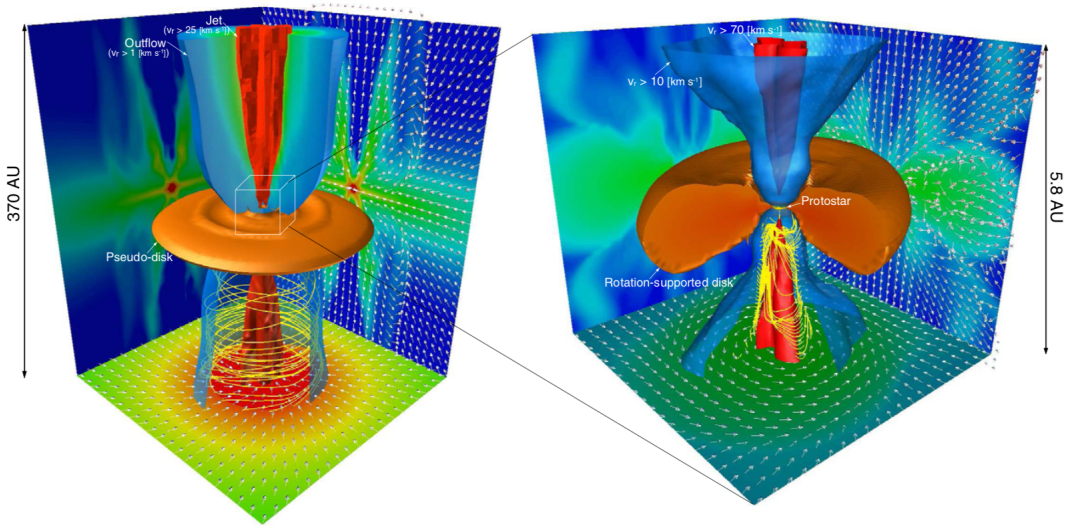

Figure 1.1. Three-dimensional structure on different scales (as specified next to the image). The right panel is a close-up view of the box outlined in the left panel. The low-velocity and high-velocity flows are depicted by blue and red volumes, respectively. The high density gas region, which corresponds to the pseudo disc (left) and rotation-supported disc (right), is plotted as an orange iso-density surface. The density and velocity distributions on the x = 0, y = 0, and z = 0 cutting planes are plotted on the corresponding wall surface. The magnetic field lines inside the z $<$ 0 region are shown by yellow streamlines.(Machida, 2014).

levels. These spectral lines appear as emission or absorption with respect to the local continuum. Spectral lines can be broadened by radiative damping from the uncertainty principle, collisional damping or Doppler broadening. The resulting wavelength distribution is called the line profile.

Continua

Bound-free transitions result in non-discrete absorption or emission of photons which result in a continua. Above the ionisation limit, the electron energy states are free and hence not discrete. Radiative ionization of a bound electron by a photon of higher energy than required for ionisation results in a gain in kinetic energy equivalent to the energy difference. Likewise, the recombination of a free electron of arbitrarily high kinetic energy into a bound state results in the emission of a photon of frequency corresponding to the energy difference.

Intensity

The specific intensity I_v of a beam which transports a quantity of energy dE_v in a specific direction through a surface dA placed perpendicular to that direction, with the spreading of the beam confined to a solid angle $d\Omega$ around that direction, during a time dt at a specific moment, and

limited to a frequency band dv at a specific frequency v is

$$I_v = \frac{dE_v}{dt\ dv\ dA\ d\Omega}, \tag{1.28}$$

in units of erg $cm^{-2}s^{-1}$ Hz^{-1} Str^{-1}. The is an associated radiation pressure given by

$$p_v = \frac{1}{c}\int I_v \cos^2\theta d\Omega, \tag{1.29}$$

where a force is exerted only along a photon pressure gradient.

Optical depth

The change in intensity by addition of local photon emission and extinction over a path ds is

$$dI_v(s) = j_v(s)ds - \alpha_v(s)I_v(s)ds, \tag{1.30}$$

where j_v is the monochromatic emission coefficient and α_v is the monochromatic linear extinction coefficient. The optical depth through a thickness D is given by

$$\tau_v = \int^D \alpha_v(s)ds. \tag{1.31}$$

For pure extinction (no sources or emission), the intensity drops as

$$I_v(s) = I_v(0)e^{-\tau_v(s)}. \tag{1.32}$$

The medium is optically thick if $\tau_v > 1$, photons can not pass through and an observer can not see through the medium at that frequency. Conversely, the medium is optically thin if it is transparent to radiation, when $\tau_v < 1$. For example, the first core of star formation occurs because the dust becomes optically thick to outgoing radiation, trapping the energy and resulting in a rapid increase in temperature. Conversely, Lyman-Werner band photons are able to escape stellar H_{II} regions because the gas is optically thin to radiation at that wavelength (see Section 1.3.7).

1.2.6 Stellar feedback

Once a star has formed, the radiation it emits interacts with the surrounding environment throughout its lifetime, often ending in a massive explosion upon its death. This section will

briefly summarise the mechanisms in which these interactions with the ISM occur.

H_{II} regions

Massive stars emit significant radiation which is ionising to hydrogen, producing a region of ionised hydrogen known as a H_{II} region (e.g. Franco et al. 2000), which expands out through an ionising front at supersonic speeds known as an R-type front. The ionisation front stops expanding when the rate of ionisation is balanced by the rate of recombination at its Strömgren radius (Strömgren, 1939; McCullough, 2000). The front may continue to expand after transitioning into a D-type front which travels at subsonic speeds, with the shock wave from the newly ionised gas overtaking the ionisation front and compressing the neutral gas ahead of it. Star formation is inefficient in H_{II} regions, making it a self-regulating mechanism of star formation.

Type II supernova

Stars with masses $> 8M_{\odot}$ are massive enough to create elements all the way up to iron. As creating elements heavier than iron absorbs energy instead of realising it, an iron core builds up in the center of the star. When the iron core becomes so massive that it cannot support itself against gravity, collapse of the core occurs. The core can be supported by electron degeneracy pressure up to masses of $1.4M_{\odot}$, above which the collapse continues until it is halted by neutron degeneracy pressure. The implosion rebounds off the core creating an expanding shock wave that accelerates stellar material to its escape velocity, known as a type II supernova (SN) explosion. The remnants of the cores of mass $< 3M_{\odot}$ remain rapidly rotating neutron stars while more massive cores collapse further into black holes.

Type I supernova

Solar mass stars can only produce elements up to oxygen and carbon. When low mass stars exhaust their fusion source, they become white dwarfs. If a white dwarf forms a binary with another star, it can accrete mass until it reaches the Chandrasekhar mass limit of $1.4M_{\odot}$, above which its core will reach the ignition temperature for carbon fusion resulting in a type 1a SN explosion (e.g. Mazzali et al. 2007). Type 1b and 1c SN are actually the same as type II SN, with the only difference being that 1b have already lost the outer hydrogen shell before core collapse and 1c have lost their hydrogen and helium shells.

Superbubbles

During the main sequence, a massive OB type star will lose a substantial fraction of its total mass via stellar winds (Abbott, 1982) driven by the radiative pressure of spectral lines. This creates an expanding bubble of hot, low density gas around the star. The growth of the bubble is added to when the star explodes as a SN, with the contribution from multiple supernovea events combining into a superbubble that can burst through the galactic disc (McCray & Kafatos, 1987). These superbubbles trap ionising radiation, although if the bubble bursts through the disc, a dynamical chimney of escaping ionising photons forms (Dove et al., 2000). Eventually the superbubble becomes gravitationally unstable and forms molecular clouds which are the sites of future star formation.

1.3 The Early Universe

In this section, the major observations that inform our understanding of the early Universe are briefly discussed alongside our theoretical model of cosmology, before discussing the formation of the first stars, the role of magnetic fields and radiative feedback.

1.3.1 An expanding, flat Universe

The standard model of Big Bang cosmology is the Lambda cold dark matter (ΛCDM) model, which predicts that the Universe contains three components, the least abundant of which is ordinary baryonic matter. The second component is cold dark matter (CDM). The existence of dark matter was first inferred when the mass of all the stars in the Coma cluster of galaxies only provided 1 percent of the mass required to keep the galaxies from escaping the gravitational pull of the cluster (Zwicky, 1933). CDM means that the DM moves slowly relatively to the speed of light and reacts very weakly with ordinary matter and electromagnetic radiation. The third component is a dark energy associated with a cosmological constant Λ, responsible for the acceleration of the expansion of the Universe.

The Universe was shown to be expanding after observations by Hubble (1929) showed that the radial velocity of extra-galactic nebulae increased with increasing distance from the Earth. In cosmological calculations, a stationary object within a coordinate space that expands with time remains at the same co-moving coordinate, but the space between the coordinates expands proportionally to a scale factor $a(t)$ that also increases in time. The light travelling between co-moving coordinates is stretched by the expanding space, defining the term redshift z by the ratio of the emitted wavelength to the observed wavelength

$$1 + z = \frac{\lambda_{\text{obs}}}{\lambda_{\text{emit}}} = \frac{a_{\text{obs}}}{a_{\text{emit}}} = \frac{1}{a_{\text{emit}}}, \tag{1.33}$$

where the convention is that the scale factor at the present time equals 1. Taking the initial values of physical distances, velocities, densities and magnetic field strengths as their value today and evolving them back in time to redshift z gives

$$L = \frac{L_0}{1+z}, \tag{1.34}$$

$$v = \frac{v_0}{\sqrt{1+z}}, \tag{1.35}$$

$$\rho = \rho_0(1+z)^3, \tag{1.36}$$

$$B = B_0(1+z)^2. \tag{1.37}$$

Observations have also given us insights into the curvature of the Universe. If ρ_{crit} is the mass energy required for a flat Universe, there is a density parameter Ω defined as the average density of the universe divided by ρ_{crit}, such that $\Omega > 1$ for positive curvature, < 1 for negative curvature and 1 for flat Euclidean geometry. Measurements of Ω are consistent with flat geometry (e.g. Efstathiou & Gratton 2020). Flat geometry was also found by the results of the BOOMERanG experiment (de Bernardis et al., 2001; Netterfield et al., 2002), which measured the cosmic microwave background (CMB) using high-altitude balloons and calculating that the sum of angles in a triangle equal 180.

1.3.2 CMB, structure formation and DM halos

Initially, the Universe was too hot and dense for ions and electrons to combine, matter existed as an ionised plasma. The temperature of the universe dropped for $\sim 3.7 \times 10^5$ yrs before it was cool enough (10^4 K) for atoms to form, this is known as recombination and occurred at a redshift of $z \sim 1100$. The primordial plasma was efficient at scattering radiation, so it is impossible to observe events before recombination. However, the neutral atoms resulting from recombination could not interact with radiation, allowing it to freely stream, forming the CMB. The CMB was first detected by Penzias & Wilson (1965) and has an almost perfect black-body spectrum, which tells us that the photons were in equilibrium. The anisotropies in the CMB are very small, which shows that the Universe at the point of last scatter was very smooth (Wilson & Penzias, 1967). However, the small perturbations in the plasma detected (Kogut et al., 1993; White et al., 1993) have fractional temperature fluctuations of 10^{-5}, indicating inhomogeneities in the smooth Universe.

These fluctuations in density grew through gravitational collapse to eventually form the first large structures in the Universe. However, this was not achieved through regular Jeans-style fragmentation and collapse, as the primordial baryonic mass fluctuations were smaller than the primordial Jeans mass and hence wiped out by pressure forces. On the other hand, primordial density fluctuations in the cold DM obey a power spectrum that decrease towards higher mass fluctuations, approaching $P(k) \propto k^{-3}$ asymptotically on small scales, where k is the wavenumber. Neighbouring DM over-densities or 'halos' interacted to gain angular momentum and collapse

linearly until the perturbation $\delta = (\rho_{\rm halo} - \rho_{\rm b})/\rho_{\rm b} \sim 1$ where $\rho_{\rm halo}$ and $\rho_{\rm b}$ are the density of the halo and background, respectively. These halos underwent non-linear collapse until reaching virial equilibrium through a process called violent relaxation (Lynden-Bel, 1967). Numerical work with initial conditions inspired by cosmological CDM models show that the first objects to form were dark matter halos of $\sim 10^5 - 10^6$ $M_\odot$, close to the cosmological Jeans mass at $z \sim 20 - 50$ (Couchman & Rees, 1986; Haiman et al., 1996a; Tegmark et al., 1997). Within the gravitational potential well of these DM halos, the trapped baryonic gas was heated by adiabatic compression until it reached its virial temperature of $\sim$ 5000 K (Bromm et al., 2002).

1.3.3 Population III star formation

For stars to form, the baryonic gas must cool to become gravitationally unstable and decouple from the DM. While cooling from metals and dust facilitates collapse in present-day gas, the composition of primordial gas was much simpler, containing mainly atomic hydrogen. From CMB calculations, Peebles (1966) showed that a large amount of 4He, along with smaller amounts of lighter elements were produced in the big bang, giving a primordial He abundance of $\sim 25\%$. Also present were Li and D, the evolution of all primordial chemical species was calculated by Galli & Palla (1998) and is shown in Figure 1.2. At around $z \sim 15$, gas falling into the gravitational potential of DM halos was shock heated up to 10^4 K where it could form H_2. It is this H_2 that allows the primordial gas to cool and begin to collapse, decoupling from the DM and beginning the journey towards star formation.

In present day star formation, the first core forms at $\sim 10^{-13}$ g cm^{-3} due to a rapid temperature increase when the gas becomes opaque to dust emission. (See bottom tack of Figure 1.4) There was no dust before the formation of Pop III stars, so there is no first core during their formation. Unlike present day star formation where the chemistry is largely unimportant to star formation (e.g. Glover & Clark 2012), understanding the chemical reactions that occur between the few chemical species available is crucial to understanding Pop III star formation.

H_2 formation

Before the first generation of stars, the only coolant present in significant quantities that is effective bellow 10^4 K was H_2 (e.g. Lepp & Shull 1984). In comparison, HD LiH, H_3^+ and HeH^+ do not significant affect the chemistry or provide significant cooling (e.g. Abel et al. 1997). As direct radiative association of atomic hydrogen is strongly prohibited (Gould et al., 1963), the formation of H_2 primarily occurred via the slow radiative association reaction forming H^-

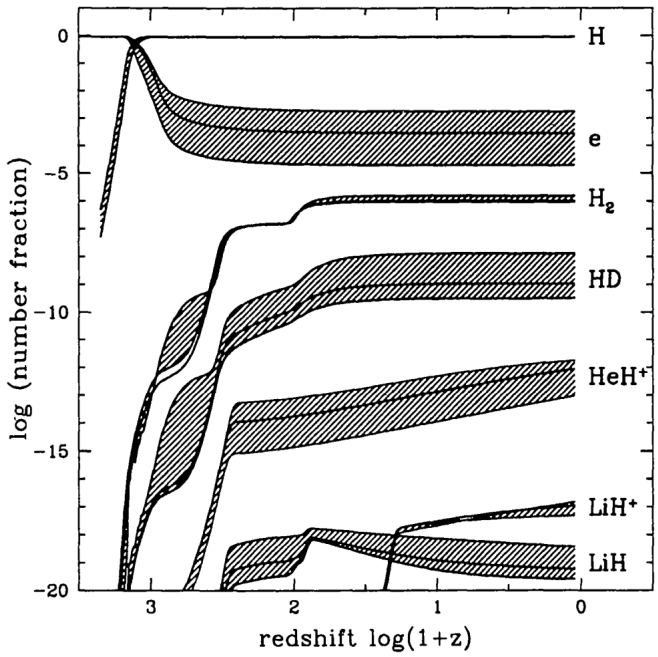

Figure 1.2. Evolution of primordial chemical abundances with redshift (Galli & Palla, 1998).

$$\mathrm{H} + \mathrm{e}^- \rightarrow \mathrm{H}^- + \gamma, \tag{1.38}$$

the rate of which depends on the ionization of the gas. This is followed by the fast associative detachment reaction

$$\mathrm{H}^- + \mathrm{H} \rightarrow \mathrm{H}_2 + \mathrm{e}^-. \tag{1.39}$$

Equation 1.39 competes with the mutual neutralisation of H^- by protons

$$\mathrm{H}^- + \mathrm{H}^+ \rightarrow \mathrm{H} + \mathrm{H}, \tag{1.40}$$

or photodetachment by infrared/optical photons

$$\mathrm{H}^- + \gamma \rightarrow \mathrm{H} + \mathrm{e}^-. \tag{1.41}$$

For $z > 100$, the CMB temperature is high enough to give a high photodetachment rate of H^-, so H_2 has to form via

$$\begin{aligned} \mathrm{H} + \mathrm{H}^+ &\rightarrow \mathrm{H}_2^+ + \gamma \\ \mathrm{H} + \mathrm{H}_2^+ &\rightarrow \mathrm{H}_2 + \mathrm{H}^+. \end{aligned} \tag{1.42}$$

However, as the Universe expands, the CMB temperature decreases and the H^- pathway of H_2 formation dominates.

Once H_2 forms, it can be destroyed by charge transfer with H^+ as

$$\mathrm{H_2 + H \rightarrow H_2^+ + H}, \tag{1.43}$$

or by collisional association with free electrons or atomic hydrogen

$$\begin{aligned} \mathrm{H_2 + e^- &\rightarrow H + H + e^-} \\ \mathrm{H_2 + H &\rightarrow H + H + H}, \end{aligned} \tag{1.44}$$

or by photodissociation via the soloman process

$$\mathrm{H_2 + \gamma \rightarrow H + H}. \tag{1.45}$$

Glover et al. (2006) showed that the uncertainties in associate detachment and mutual neutralisation rate coefficients introduce large uncertainties in the H_2 abundance and cooling rate of hot ionised gas during the collapse.

At these temperatures, rotational transitions can only occur via electrical quadrupole radiation with small transition probabilities because H_2 possesses no determinant dipole moment. The maximum cooling rate of H_2 is set by the transition to local thermal equilibrium (LTE) from non-LTE, at the critical density of $\sim 10^3$-10^4 cm^{-3}. The minimum temperature attainable due to H_2 cooling is then 500K, but the Maxwellian velocity distribution tail allows real minimum temperatures of $\sim$100-200K. Figure 1.3 shows the temperature and chemical abundance profiles of these halos during this heating and cooling cycle.

HD cooling

While HD cooling has little effect on the outcome of regular Pop III star formation (e.g. Bromm et al. 2002), gas cooling from an ionised state e.g. in relic primordial H_{II} regions, will form significant HD which can cool the gas down to the temperature of the CMB (e.g. Nakamura & Umemura 2002). The dominant mechanism of HD formation in this scenario is

$$\mathrm{H_2 + D^+ \rightarrow HD + H^+}, \tag{1.46}$$

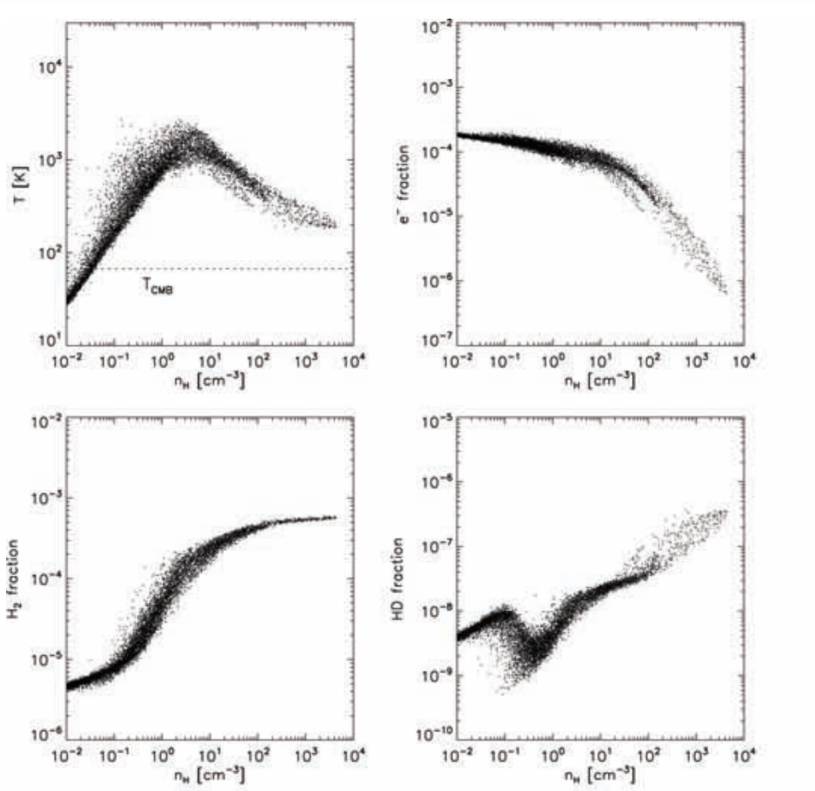

Figure 1.3. Temperature and chemical abundacne profiles of gas falling into the gravitational potential well of a DM halo (Greif et al., 2008).

while destruction primarily occurs by

$$\mathrm{HD} + \mathrm{H}^+ \rightarrow \mathrm{H}_2 + \mathrm{D}^+. \tag{1.47}$$

As HD can cool the gas down to lower temperatures that H_2 and remains an effective coolant up to densities of 10^{-18} g cm^{-3}, the characteristic mass of Pop III stars was initially expected to drop to $\sim 10M_\odot$ (Yoshida et al., 2007b) down from the regular Pop III characteristic mass of $\sim 100M_\odot$ (e.g. Yoshida et al. 2006). However, Smith et al. (2011) showed that significant HD cooling resulted in smoothing of small-scale structure when it was reheated by compression, yielding less fragmenting that regular Pop III formation. Glover & Abel (2008) showed that correct HD modeling in primordial gas requires cooling via collisions between H_2 and photons or electrons to be included in primordial chemistry packages, as neglecting it produces too much HD that can significantly effect the thermal evolution of the gas.

Three-body H_2 formation

As the H_2 formation rate depends on the free electron abundance, which decreases as the gas gets denser due to recombination, H_2 formation is dominated by three-body formation above $\sim 10^{-16}$ g cm^{-3}. The reaction is

$$\mathrm{H} + \mathrm{H} + \mathrm{H} \rightarrow \mathrm{H_2} + \mathrm{H}, \tag{1.48}$$

the rate of which increases with increasing density. Turk et al. (2011) showed that uncertainties in the three-body formation rate drastically changes the chemical abundances, morphology and velocity structure of the gas in high density regions. Decreasing the rate causes the molecular region in the centre to shrink, display less small-scale structure and take longer to collapse. The importance of this rate is contributed to by the heating produced by the three-body H_2 formation, which can become the dominant heating source in high density regions.

Collision-induced emission

H_2 line cooling becomes optically thick above densities of $\sim 10^{-14}$ g cm^{-3} (Ripamonti & Abel, 2004). Although H_2 has no electric dipole, during a collision with either H_2, He or H the pair act as a supermolecule with a non-zero electric dipole, with a high probability of emitting/absorbing a photon. Collisions happen on a very small timescale, which means the collision-induced lines broaden to form a continuum. This continuum emission provides efficient cooling of the gas until it becomes optically thick to the continuum at 10^{-8} g cm^{-3} (Yoshida et al., 2008). Above this density, dynamical heating of the gas during its collapse causes hydrogen molecules to collisionally dissociate, providing cooling until the molecular hydrogen is fully dissociated and the gas cannot transfer energy out. The collapse continues adiabatically, resisting fragmentation as the temperature increases rapidly to above 10,000 K where it becomes pressure supported and the protostar forms. The top tack of Figure 1.4 shows the thermal evolution of metal-free, primordial gas.

1.3.4 Fragmentation of primordial gas

Early simulations of primordial gas collapsing in dark matter minihalos suggested that Pop III stars were massive (>100M$_\odot$: e.g. Bromm et al. 1999) and formed in isolation (e.g. Haiman et al. 1996a). However, Clark et al. (2011a) studied the effects of turbulence on primordial gas clouds, finding that even subsonic turbulence caused fragmentation, indicating that Pop III stars formed in groups. Since then, many studies have investigated the fragmentation behaviour of primordial gas.

A potential major factor to consider when assessing the fragmentation of primordial gas is accretion luminosity as mass is accreted onto primordial protostars, which provides additional

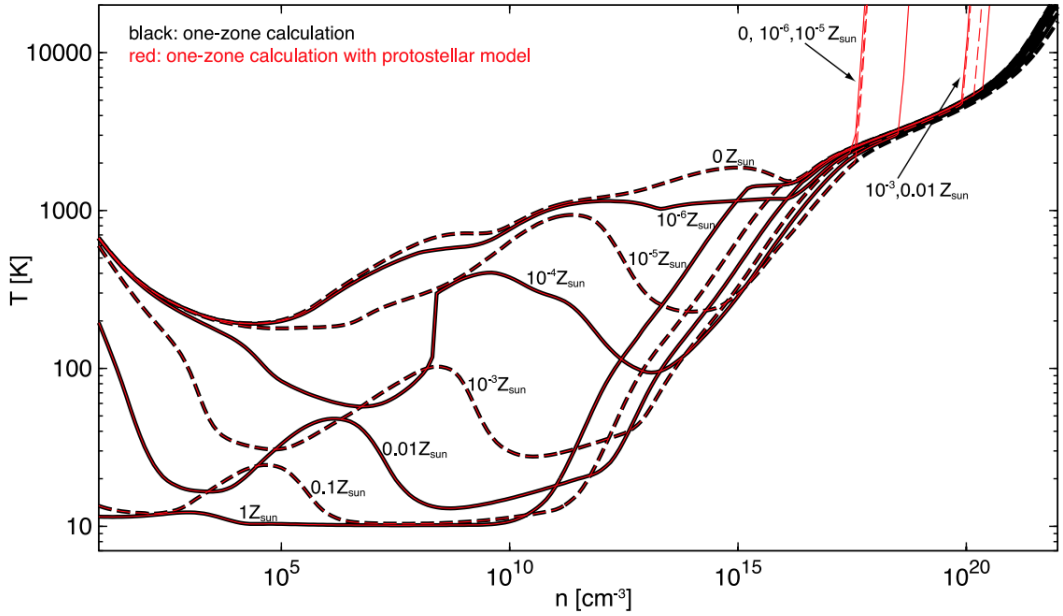

Figure 1.4. One-zone calculations by Machida & Nakamura (2015) for gas collapse with different metallicities, with and without a protostellar model.

heating to the disc. However, when it was implemented into GADGET-2 (Springel, 2005) in Smith et al. (2011), accretion feedback was revealed to not be a dominant factor affecting fragmentation of primordial gas. They found that accretion feedback could reduce the number of fragments formed in halos that were already slow at forming low numbers of protostars, but was negligible in halos forming many protostars rapidly.

Another factor to consider stems from one of the most prominent alternative hypotheses for the nature of dark matter are weakly interacting massive particles (WIMPs) (Kimball & Budker, 2023). WIMPs can self-annihilate at high densities, releasing a cascade of photons which could act to halt gas collapse and fragmentation. The effects of WIMPs on Pop III star formation were investigated by Stacy et al. (2014), who used a 'live' gravitational potential of N-body DM particles to show that the centrally peaked DM density profile was gradually flattened by gravitational interactions with gaseous disc particles, suppressing dark matter annihilation (DMA). They concluded that DMA was insufficient to prevent gas collapse and fragmentation of primordial gas in DM minihalos.

Less exotic factors have been shown to affect the fragmentation behaviour of primordial gas. Just as Clark et al. (2011a) showed that subsonic turbulence causes disc fragmentation, rotation has been shown to cause fragmentation by Wollenberg et al. (2019). Interestingly, while they showed that that any level of rotation or turbulence resulted in fragmentation of the disc, they found that when applied together, the rotation acted to stabilise the disc against fragmentation.

They also found that neither turbulence or rotation affected the accretion rate onto the protostar, instead the high accretion rates were controlled by density and temperature of the infalling material.

Throughout the various simulations of Pop III star formation, a common outcome is a top-heavy IMF i.e. the high mass slope is less steep than the Salpeter value (e.g. Schneider et al. 2006; Susa et al. 2014; Stacy et al. 2016; Wollenberg et al. 2019; Sharda et al. 2020). While solar-like metallicities have a bottom-heavy IMF with most of the mass in low-mass stars as discussed in Section 1.2.1, it has recently been explicitly shown that the mass spectrum becomes logarithmically flat and top-heavy as the metallicity of simulations is decreased towards primordial chemistry (Chon et al., 2021). This paints the picture that as each generation of stars chemically enriched the ISM to higher metallicities, the distribution of stellar masses shifted towards lower mass stars.

1.3.5 Primordial magnetic fields

Uniform magnetic fields

While it was shown in Section 1.2.4 that magnetic fields play an important role in present-day star formation, they were neglected in the Pop III studies discussed in Section 1.3.4. While present-day magnetic fields come in the form of the large-scale galactic field, the properties of magnetic fields in the early Universe and their role in primordial star formation were not immediately obvious. While recent studies have investigated a process of magnetic field amplification in the early Universe known as the *small-scale turbulent dynamo* that results in a small-scale, tangled magnetic field (e.g. Sur et al. 2010; Federrath et al. 2011a; Schober et al. 2012a), many studies have instead opted to study the effects of uniform fields on Pop III star formation.

The effects of uniform magnetic fields on Pop III star formation are comparable to that of uniform fields in present-day star formation, acting to prevent fragmentation and launching jets when sufficiently strong magnetic fields are applied. For example, three-dimensional MHD nested grid simulations by Machida et al. (2008) showed that fragmentation and jet behaviour depended on the ratio of the initial rotational to magnetic energy. Magnetically-dominated scenarios resulted in jets without fragmentation while rotationally-dominated models resulted in fragmentation without jets. Similarly, Machida & Doi (2013) performed resistive MHD simulations with an initially uniform magnetic field, finding that for initial field strengths above 10^{-12} G, angular momentum around the protostar is transferred by both magnetic braking and protostellar jets. In this case, the gas fell directly on to the protostar without forming a disc, forming a single massive star.

Small-scale turbulent dynamo

While Section 1.3.5 shows that uniform magnetic fields can change the outcome of Pop III star formation, the magnetic fields present during the formation of Pop III stars likely were highly disordered, unlike the large-scale fields present in the galactic ISM today. Multiple mechanisms of generating magnetic fields in the early Universe are covered in literature. Generation of magnetic fields is predicted by Faraday's law if an electric field caused by electron pressure gradients has a curl, which is known as the Biermann battery (Biermann, 1950). Alternatively, an anisotropic distribution of electron velocities in a homogeneous, collisionless plasma supports unstable growth of electromagnetic waves, known as the Weibel instability (Weibel, 1959). Magnetic fields may have also been produced by cosmological density fluctuations (Ichiki et al., 2006) or by cosmic rays from Pop III supernovae which induce currents, the curl of which are capable of generating magnetic fields (Miniati & Bell, 2011).

Irrespective of their origin, magnetic seed fields are believed to have eventually grown into the large scale galactic magnetic fields observed today (e.g. Kulsrud 1990). It is suggested that the amplification begins during the collapse of the gas that formed the first stars (e.g. Kulsrud et al. 1997; Schleicher et al. 2010; Silk & Langer 2006), which form within low mass DM halos (Couchman & Rees, 1986). Along with the natural $\propto \rho^{2/3}$ amplification from flux freezing, the small-scale turbulent dynamo (Vainshtein et al., 1980) converts the kinetic energy of an electrically conductive medium into magnetic energy through stretching and folding the field lines (see Figure 1.5), amplifying the magnetic field when turbulence is generated during the collapse of the DM minihalo. Magnetic fields amplified by turbulent motions produce $P(k) \propto k^{3/2}$ power spectra (Kazantsev, 1968), where the energy increases for smaller spatial scales, in contrast to the standard turbulent velocity power spectrum which has more energy on larger spatial scales.

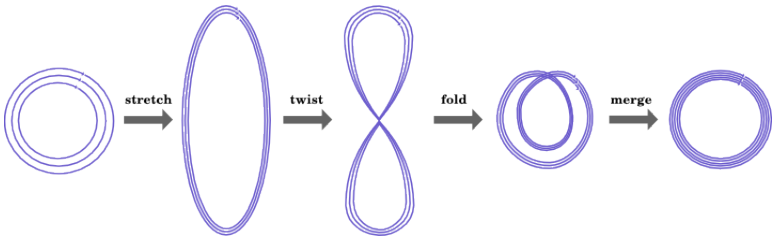

Figure 1.5. Mechanism of magnetic field amplification during the small-scale turbulent dynamo (taken from https://jennifer-schober.com).

The turbulent dynamo ends once the field has saturated at an equilibrium between kinetic and magnetic energy. This is expected to happen on timescales shorter than the collapse time of the halo (e.g. Schober et al. 2012a). While these fields are small scale and chaotic, they can still assist in resisting fragmentation due to the isotropic nature of the magnetic pressure, which

contributes to a quasi-isotropic acoustic-type wave along with the gas pressure. The magnetic field strength resulting from the small-scale turbulent dynamo depends on the efficiency of the dynamo process, which depends on the Reynolds number (Sur et al., 2010) and hence, in simulations, the resolution used (Haugen et al., 2004). This results in underestimated dynamo amplification of the magnetic fields in numerical simulations. Despite underestimated amplification, Schleicher et al. (2010) showed that magnetic fields are significantly enhanced before the formation of a protostellar disc, where they can change the fragmentation properties of the gas and the accretion rate. The dependence of the amplification process on resolution is shown in Federrath et al. (2011a), who ran MHD dynamo amplification simulations testing the effects of varying the Jeans refinement criterion from 8-128 cells per Jeans length on the field amplification during collapse. They ran their simulations up to density $\sim 10^{-13}$ g cm^{-3}, finding that dynamo amplification was only seen when using a refinement criteria of 32 cells per Jeans length and above. The resulting power spectrum was of the $k^{3/2}$ Kazantsev type. The field was still amplified for smaller refinement criteria as $\rho^{2/3}$ i.e. due to flux freezing during the gravitational collapse. They found that the scale where magnetic energy peaks shifts to smaller scales as resolution was increased. The velocity power spectra indicated that gravity-driven turbulence exhibits an effective driving scale close to the Jeans scale. For the 128 cells per Jeans length run, the magnetic field strength reached ~ 1mG when the central region of collapse reached 10^{-13} g cm^{-3}.

As the field amplifies, the peak of the energy spectrum is expected to shift to larger spatial scales until reaching a peak scale at saturation (Schober et al., 2015), after which amplification occurs due to flux freezing alone (Schober et al., 2012b). The peak energy scale at saturation depends on the driving scale of the turbulence, which in turn depends on the slope of the velocity spectrum. The ratio of magnetic to kinetic energy E_B/E_k at dynamo saturation is a useful value for estimating magnetic fields strengths in the early Universe, however its value varies between studies. Schober et al. (2015) found that $E_B/E_k = 0.0134$ for pure Burgers compressible turbulence ($P(k) \propto k^{-2}$), increasing to 0.304 as the turbulence was mixed more with incompressible modes into pure incompressible Kolmogorov turbulence ($P(k) \propto k^{-5/3}$), while Federrath et al. (2011b) found values in the range 0.001 to 0.6, and Haugen et al. (2004) found a value of 0.4. The theoretical upper limit is a ratio of 1 i.e. equipartition between the velocity and magnetic field.

While most Pop III MHD simulations have implemented unrealistic uniform magnetic fields, recently Sharda et al. (2020) performed MHD simulations with a Kazantsev $k^{3/2}$ spectrum, finding suppressed fragmentation in the presence of strong magnetic fields, resulting in a reduction in the number of first stars with masses low enough that they might be expected to survive to the present-day. However, they only ran the simulations up to a maximum density of $\sim 10^{-11}$ g cm^{-3} and spatial resolution of 7.6 au. If primordial gas becomes adiabatic and hence stable to fragmentation at densities of 10^{-4} g cm^{-3} at T$\sim 10^4$ K corresponding to a Jeans scale of 0.024

au, the study can not sufficiently resolve the degree of fragmentation primordial gas experiences. Furthermore, the limited resolution means that the smallest scale magnetic fields are artificially uniform on scales roughly 300 times larger than the stellar cores. Also, collision-induced emission kicks in to become the dominant cooling process at $\sim 10^{-10}$ g cm^{-3} and dissociation of H_2 molecules provides effective cooling after $\sim 10^{-8}$ g cm^{-3} (Omukai et al., 2005), so the study has not included a full chemical treatment. There are further concerns that an under-resolved initial magnetic field would lead to collapse within a region that does not properly sample the $k^{3/2}$ power spectrum. In the worst case scenario the collapse could occur within a region of uniform field, significantly increasing the ability of the field to suppress fragmentation.

1.3.6 Pop III H_{II} regions

The factors effecting the escape fractions of UV photons from Pop III stars are widely different from present day H_{II} regions. Pop III stars are not thought to have line driven stellar winds (Vink et al., 2001), so the wind bubbles around OB type stars that can trap UV photons likely do not exist around them. Additionally, the lack of dust means that UV photons are not impeded from escaping. The uncertainty in the mass of Pop III stars also effects their ionising photon output.

As Pop III stars ionise their environments, the region of high pressure ionised gas spreads out as a subsonic (D-type) ionisation front to ∼1 pc before evolving into a supersonic (R-type) ionisation front and escaping the halo on timescales much shorter than the main sequence lifetime, giving an escape fraction of 0.7-0.95 (Whalen et al., 2004; Kitayama et al., 2004; Alvarez et al., 2006). Most of the gas surrounding the Pop III star evacuates the halo due to the ionisation front even if the star does not produce a supernovae. Only halos with masses $> 10^7$ $M_\odot$ can confine the D-type shock inside their virial radius, giving an escape fraction of essentially zero (Kitayama et al., 2004). Despite this, escaping ionisation fronts can not ionise the center of nearby halos (Alvarez et al., 2006).

Once the star has died, filamentary structures surrounding the halo shield the gas from ionisation and allow gas to stream into the halo. Large amounts of molecular hydrogen form in the relic H_{II} regions, allowing further star formation (Abel et al., 2007). HD cooling in relic H_{II} regions allows the gas to cool to ~ 10 K, where run-away collapse of $\sim 40 M_\odot$ clumps occurs, leading to lower mass Pop III stars compared to the $200 - 300 M_\odot$ primordial gas clouds (Yoshida et al., 2007a). However this result is challenged by Smith et al. (2011) who found that significant HD cooling resulted in smoothing of small-scale structure, leading to less fragmenting that regular Pop III formation.

More recent simulations suggest that H_{II} regions around Pop III stars may not even break out

of the accretion disc (Jaura et al., 2020, 2022). The simulations show that ionising radiation from these stars is trapped in the dense accretion disc surrounding them, hence radiative feedback has no significant impact on either the number or the total mass of protostars. They argue that unlike their simulations, previous studies did not inject photons from the star on scales smaller than the local scale height of the accretion disc. Clearly the topic of primordial H_{II} is an ongoing field, with more studies required to understand their impact on the inner and exterior environments of the halo.

1.3.7 Lyman-Werner radiation and atomic halos

While so-called Pop III.1 stars form from purely cosmological initial conditions, the radiation they produce effects Pop III.2 stars that form in its presence. As the masses of Pop III stars are predicted to be larger than present-day counterparts (due to the lack of dust and metals), they are expected to emit highly ionising radiation (Schaerer, 2002). Ionizing photons above the Lyman limit (13.6 eV) create H_{II} regions around the stars up to the boundary of their Strömgren spheres (Strömgren, 1939; McCullough, 2000), while photons below the Lyman limit escape their Strömgren sphere. These far-ultraviolet (FUV) photons can dissociate H_2 via the two-step Solomon process (Field et al., 1966; Stecher & Williams, 1967)

$$H_2 + \gamma \rightarrow H_2^* \rightarrow 2H, \tag{1.49}$$

where H_2^* represents an excited state of H_2. Photons with energy above 0.76eV can also photodissociate H^- via

$$H^- + \gamma \rightarrow H + e^-, \tag{1.50}$$

reducing H_2 formation via Equation 1.39 (e.g. Chuzhoy et al. 2007). This stellar feedback provides a potential obstacle for Pop III.2 stars to overcome during formation. Investigations into the effects of these far UV fields typically categorise the field strength by the intensity in Lyman-Werner (LW) bands J_{21}, in units of 10^{21} erg s^{-1} Hz^{-1} sr^{-1}.

Calculations by Haiman et al. (1997) found that before the Strömgren spheres of Pop III stars overlap, the UV background below the ionization threshold was able to penetrate large clouds and suppress their H_2 abundance. They also found that the flux necessary for H_2 photodissociation is several orders of magnitude smaller than the flux needed to reionize the universe. Haiman et al. (2000) showed that this photodissociation of H_2 suppresses further star formation inside small halos and delays reionization until larger halos form.

Collapse is not impossible without sufficient H_2 for cooling. Omukai (2001) showed that if the LW field is sufficient to keep the cloud free of molecular hydrogen, they can collapse via atomic

hydrogen line cooling if they are massive enough to reach virial temperatures of ~ 8000 K. The collapse occurs almost isothermally, possibly resulting in direct collapse black holes (DCBH) (e.g. Bromm & Loeb 2003; Spaans & Silk 2006; Latif et al. 2013a) which could explain high redshift quasar observations (e.g. Mortlock et al. 2011; Matsuoka et al. 2019). However, for a T = 10^5 K blackbody spectrum expected from Pop III stars, a field strength of $J_{21} \sim 10^4$ is required to keep the gas atomic during the collapse (Glover, 2015; Agarwal & Khochfar, 2015; Agarwal et al., 2016; Sugimura et al., 2014), while the average exposure is expected to be $J_{21} < 0.1$ at $z \sim 15$ (Ahn et al., 2009; Trenti & Stiavelli, 2009; Wise et al., 2012; Agarwal et al., 2012; Skinner & Wise, 2020). Dijkstra et al. (2008) showed that only a fraction of $10^{-8} - 10^{-6}$ of DM halos with temperatures $> 10^4$ K have a close luminous neighbour within < 10 kpc, and are exposed to an LW flux $J_{21} > 10^3$. The occurrence of atomically cooled halos is therefore expected to be rare.

Studies have shown that values of J_{21} orders of magnitude lower than the critical intensity required to form atomic halos can still drastically affect halo collapse. Typically, the critical mass for efficient molecular hydrogen cooling and subsequent star formation increases with increasing J_{21} (e.g. Machacek et al. 2001; Yoshida et al. 2003; O'Shea & Norman 2008; Visbal et al. 2014; Schauer et al. 2021). Cosmological simulations by Yoshida et al. (2003) found gas cooling was suppressed for $J_{21} = 0.1$, predicting that star formation would not occur. Conversely, O'Shea & Norman (2008) found that for as high as $J_{21} = 1$, H_2 cooling leads to collapse despite the depressed core molecular hydrogen fractions. They also noted that higher LW background fluxes resulting in higher accretion rates. High resolution cosmological simulations by Schauer et al. (2021) showed that both the average and minimum minihalo mass M_{av} and M_{min} required to form enough H_2 to form stars increased with increasing J_{21}. However, they found that increasing streaming velocities between baryons and dark matter had a larger increases M_{av} and M_{min}. In contrast, cosmological simulations by Skinner & Wise (2020) found no relationship between the LW intensity and host halo mass.

The true average J_{21} intensity is expected to vary with redshift. Hirano et al. (2015) followed the formation and evolution of 1540 star-forming gas clouds. The characteristic mass of Pop III stars shifted to lower masses with decreasing redshift due to the radiative feedback of previous generations of stars. For $z > 20$, half of the star-forming gas clouds were exposed to intense FUV radiation, with an average exposure of $J_{21} \sim 0.07$. Due to smaller stellar masses and the expanding distance between stars, the FUV background is weaker at lower redshifts. For $15 < z < 25$, almost all the clouds have nonzero intensity $J_{21} > 0.01$. The average LW intensity in Skinner & Wise (2020) increased stochastically from 10^{-3} at $z \sim 25$ to 10 at $z \sim 10$. For redshifts above $\sim$12, J_{21} remained > 0.1.

When H_2 forms at the center of a DM halo, the outer layers can shield the inner H_2 from photodissociation. This self-shielding allows further H_2 production and H_2 cooling (Shang et al.,

2010; Agarwal et al., 2014; Regan et al., 2014; Hartwig et al., 2015a). The large non-equilibrium abundance of electrons in gas cooling from above $T > 10^4$ K also boosts H_2 formation (Oh & Haiman, 2002). Early attempts to model self shielding (e.g. Shang et al. 2010) multiplied the intensity in the LW band by a self-shielding factor given by Draine & Bertoldi (1996). Wolcott-Green et al. (2011) showed that this method underestimated the numerically calculated self-shielding rate by more than an order of magnitude in low-density regions by overestimating shielding by a large factor at temperatures above a few hundred kelvin. They modified the method of Draine & Bertoldi by estimating of the shielding factor based on the Sobolev length using local properties of the gas. This modification was computationally inexpensive and used in many subsequent investigations into the aforementioned critical intensity required to form atomic halos, typically producing values an order of magnitude lower than those using the original Draine & Bertoldi shielding (e.g. Glover 2015; Agarwal & Khochfar 2015; Agarwal et al. 2016). Clark et al. (2012) improved on this method further with their introduction of the TreeCol algorithm, which calculates maps of the column density distribution seen by each computational element in a simulation in a computationally efficient fashion with the help of an oct-tree. Hartwig et al. (2015b) took this approach further by accounting for the relative velocities between different computational elements. This Doppler-shifts the spectral lines, reducing the effectiveness of self-shielding (since molecules shifted by more than the linewidth do not contribute to the effective column density).

1.3.8 Pop III supernovae

Findings that Pop III stars were massive lead to investigations into the SN that massive stars produce. For stars between 140-260$M_\odot$, after central helium burning, electron/positron pairs are created, converting internal gas energy into rest mass of the pairs without contributing much to the pressure. The star contracts rapidly until implosive oxygen and silicon burning produces enough energy to revert the collapse, accompanied by SN-like mass ejection. This is known as a pair-instability SN (e.g. Heger & Woosley 2002), which are the the most energetic and the brightest thermonuclear explosions in the Universe. However, no elements heavier than zinc are produced. The star eventually produces a large iron core in hydrostatic equilibrium, which likely collapses to form a black hole. For stars of mass $> 260 M_\odot$, the energy released is not sufficient to reverse the implosion, leading to the formation of a massive black hole (Fryer et al., 2001).

The efficiency of gas evacuation by SN is determined by the initial halo mass, the ability of the progenitor star to ionize the halo and drive out gas in its inner region prior to the SN, and the stellar mass or injection energy of the SN. The halo's gas density profile is largely dependent on the radiative feedback prior to the explosion. In the case of $10^7 M_\odot$ halos where the gas remains

dense prior to the explosion, a pair-instability SN shock is heavily confined and the thermal energy of the remnant is quickly radiated away by free-free emission, whereas for $< 10^6 M_\odot$ halos where the ambient gas density is significantly reduced by stellar radiation prior to the SN explosion, the blast wave quickly propagates over the halo's virial radius, resulting in complete evacuation of the gas (Kitayama & Yoshida, 2005). The shock radius can extend out to 2.5 kpc and terminate star formation in these halos for at least 200 Myr (Greif et al., 2007). The shock becomes highly anisotropic once it leaves the host halo and encounters filaments and neighboring halos, where it exerts a positive mechanical feedback on neighboring minihalos by shock-compressing their cores.

Pair-instability SN are capable of injecting over 90% of their stellar metals into a ∼1 kpc region surrounding the star, suggesting that a large region of the Universe was enriched with metallicity $> 10^{-4} Z_\odot$ by $z = 15$ (Bromm et al., 2003). This enrichment behaviour changes if the Pop III stellar masses are lower, as seen by the fragmentation behaviour seen in previous Pop III studies (e.g. Stacy et al. 2010; Clark et al. 2011b; Greif et al. 2011b; Hosokawa et al. 2011). SN from lower mass 40$M_\odot$ Pop III stars produce standard Type II SN, where the remnant remains partially trapped within the minihalo with roughly half of the ejecta turning around and falling back toward the center of the halo (Ritter et al., 2012). This enriches the host minihalo with metals and triggers Population II star formation within them. The nucleosynthetic yields of Joggerst et al. (2009) are in good agreement with the abundances observed in larger samples of extremely metal-poor stars, suggesting that 15-40$_\odot$ core-collapse SN with moderate explosion energies contributed the bulk of the metals to the early universe.

Small-scale magnetic fields can be converted into well-ordered magnetic fields by pair-instability SN (Seifried et al., 2014). Here the coherence length of the field grows linearly with the expansion of the SN bubble that forms up to a extrapolated radius of 1.5 kpc. This could explain how primordial magnetic fields transition into the large-scale galactic fields present today.

1.3.9 DM streaming velocities

Prior to recombination, baryons were tightly coupled to photons. As DM does not experience Thomson scattering (elastic scattering of electromagnetic radiation by a free charged particle), there should have been a relative velocity between the DM and baryons (e.g. Ma & Bertschinger 1995). At recombination, the relative velocity was $\sim$ 30 km s^{-1} and was coherent over several Mpc/$\sqrt{1+z}$. Recombination resulted in a drop in the sound speed to $\sim$ 6 km s^{-1} as the gas transitioned from plasma to a neutral state, meaning the relative velocities were highly supersonic. Tseliakhovich & Hirata (2010) showed that the presence of these large-scale streaming velocities suppresses the abundance of the first bound objects by advecting small-scale perturbations near the baryonic Jeans scale. Moving-mesh calculations by Greif et al. (2011a) found that the additional

momentum and energy from the streaming velocities reduces the gas fractions and central densities of halos, increasing the typical virial mass required for efficient cooling by a factor of three. They also noted that the turbulent velocity dispersion increased in the presence of streaming velocities.

Simulations by Hirano et al. (2017) showed that due to the prevention of gas collapse in $10^5 M_\odot$ halos, halos grew hierarchically through mergers and accretion until a $10^7 M_\odot$ halo assembled at $z = 30.5$, whose gravity could overcome the energy of the streaming velocities and facilitate collapse. The trapped gas was shock heated to 10^4 K where atomic hydrogen cooling and later H_2 cooling resulted in a DCBH without the need for a LW field. Similarly, cosmological simulations using the moving mesh code AREPO by Schauer et al. (2019) showed that in regions with streaming velocities $> 3\sigma_{\rm rms}$, cooling of gas in minihalos is completely suppressed, implying that the first stars in these regions form within atomic cooling halos.

1.3.10 Observing Pop III stars

Observations of Pop III stars with masses $<$ 1000 $M_\odot$ are not possible, as the $\sim 10^4$ nJy flux they produce (Schauer et al., 2020) is below the reachable limit with deep JWST imaging (Merlin et al., 2022). Similarly, a cluster of Pop III would need to have 10^5 $M_\odot$ in massive stars to be observable (Zackrisson et al., 2011), corresponding to a star formation efficiency of nearly 100% in most Pop III producing minihalos.

While observations of the stars may be impossible, an alternative is to detect the SN explosions of Pop III stars. In the case of core-collapse SN resulting from 15-40$M_\odot$ Pop III, Whalen et al. (2013a) found that these events are observable out to $z \sim$10-15. For 25-50 $M_\odot$ Pop III hypernovae, Smidt et al. (2014) calculates the signal will be visible at z = 10-15 to JWST and z = 4-5 to the Wide-Field Infrared Survey Telescope. For 90-140 $M_\odot$ Pop III pair-instability SN, Smidt et al. (2015) found that the signals are visible to JWST and 30m class telescopes in the near-infrared (NIR) out to $z \sim$ 7-10, and to Pan-STARRS and LSST in the optical out to $z \sim$ 1-2. For 150-250$M_\odot$ Pop III pair-instability SN, Whalen et al. (2013b) found that JWST will detect the signal out to $z >$ 30, while WFIRST will detect them in all-sky surveys out to $z \sim$ 15-20, and LSST and Pan-STARRS will find them at $z <$ 7-8.

Another alternative observation method are long-duration gamma-rays resulting from the explosions of massive stars (e.g. Tanvir et al. 2009; Cucchiara et al. 2011). While current gamma-ray telescopes can probe up to $z \sim$10 (e.g. Ghirlanda et al. 2015), future gamma-ray facilities will reach z$\sim$20 to probe Pop III SN (e.g. THESEUS: Amati et al. 2018).

Indirect observations of epoch of Pop III star formation are possible due to the 21 cm line, which corresponds to the energy difference between two hyperfine states in the ground state of

atomic hydrogen, split by the interaction between the electron spin and the nuclear spin. This radiation penetrates dust clouds and probes atomic hydrogen. The spin temperature $T_{\rm s}$ is defined by

$$\frac{n_1}{n_0} = 3e^{\frac{0.068}{T_s}}, \tag{1.51}$$

where n_0 and n_1 are the populations of the triplet and singlet ground state. The 21 cm line is shown in emission if $T_{\rm s} > T_{\rm CMB}$ where $T_{\rm CMB}$ is the CMB temperature $2.73(1+z)$ K, or in absorption if $T_{\rm s} < T_{\rm CMB}$ (e.g. Nusser 2005). Prior to the formation of Pop III stars, $T_{\rm s} \sim T_{\rm CMB}$, after which Lyman-$\alpha$ photons emitted by the Pop III stars are absorbed/emitted by the hydrogen, inducing transitions between hyperfine states (Wouthuysen-Field effect: Wouthuysen 1952; Field 1958). As a result, $T_{\rm s}$ shifts to the colour temperature of the Lyman-α photons, which approaches the thermal temperature of the gas through scattering with hydrogen. This transition into 21 cm viewed as emission tells us when and how quickly Pop III stars formed and has begun to put constraints on the early Universe (e.g. Liu et al. 2019; Li et al. 2019; Park et al. 2020; Reis et al. 2020,CHIME Collaboration et al. 2022).

Chapter 2

Numerical methods

2.1 SIMULATION CODES

Typically, there are two methods for evolving the fluid properties within the simulation box; the Eulerian approach is to consider a fluid flowing in/out through the boundaries of a stationary finite volume, while the Lagrangian approach is to follow individual fluid elements as they move around in a larger enclosing volume. This small change is the basis behind the differences between the two classic simulation code types, namely adaptive mesh refinement (AMR: Berger & Colella 1989) and Smoothed particle hydrodynamic (SPH: Monaghan 1992). The cells of an AMR simulation make up a stationary Cartesian grid that conserve fluid quantities flow through. The mesh is adaptive, allowing patches of finer grid spacing to be placed in areas suffering from high errors or wherever necessary. Figure 2.1 shows an example of how an AMR grid uses higher resolution in regions with steep density gradients and lower resolution in regions where it is not required. Examples of AMR codes include Enzo (Enzo Collaboration et al. 2014) and RAMSES (Teyssier, 2010). Conserved quantities flow in and out of cells and are calculated using a finite volume solver. Failure to conserve conserved quantities like density and momentum leads to non-physical results. For a given cell, finite volume solvers evolve conserved quantities in time based on the flux of those quantities at the boundaries to the cells around them. For a conserved quantity q_x^t at position x and time t, the fluxes f_x^t are calculated at the boundaries $f_{i-1/2}$ and $f_{i+1/2}$, evaluated at a half-time step $f^{n+1/2}$, the flux-conserving continuity equation becomes

$$q_i^{n+1} = q_i^n + \frac{\Delta t}{\Delta x}(f_{i-1/2}^{n+1/2} - f_{i+1/2}^{n+1/2}) \tag{2.1}$$

where

$$f_{i+1/2}^{n+1/2} = q_{i+1/2}^{n+1/2} u_{i+1/2} \tag{2.2}$$

and $u_{i+1/2}$ is the advection velocity at the boundary. This requires an estimate of q at the boundary. A popular choice is the Donor-cell advection scheme, which assumes that q is constant across the cells, and the cell boundary adopts either q_n if $u_{n+1/2}$ is positive or $q_{n+1/2}$ if $u_{n+1/2}$ is negative. A more involved method is the Piecewise linear scheme, which assumes that q is a linear function from the center of a cell to the next. A sub-grid is created and the distribution of q is reconstructed with the new linear variation within the original cells.

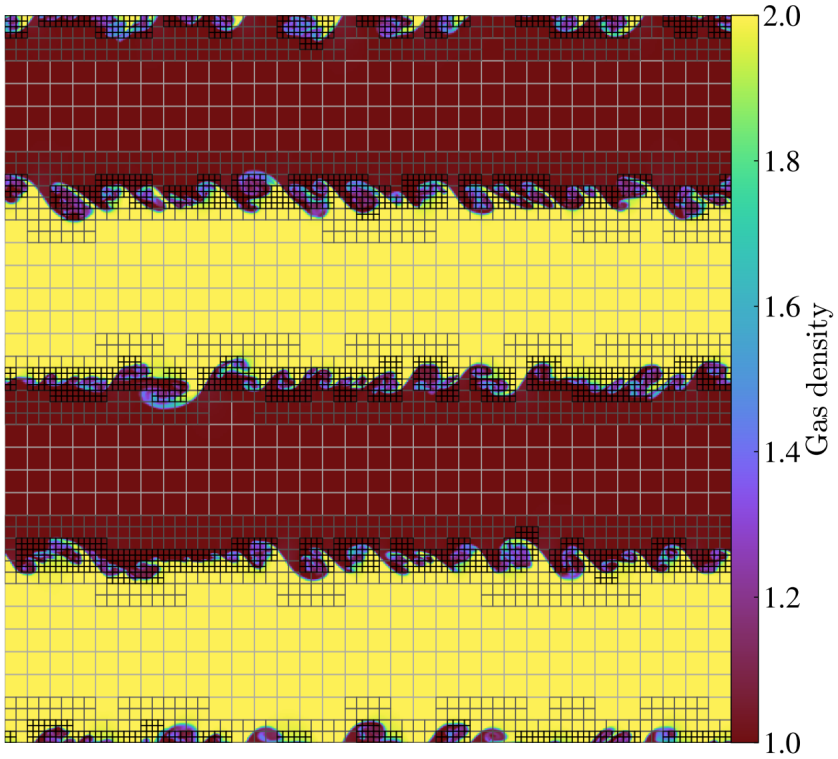

Figure 2.1. Example of AMR on a Kelvin-Helmholtz instability set-up (Schive et al., 2018).

In contrast, SPH simulations follow individual moving fluid elements and calculate gas properties of individual particles by smoothing over its nearest neighbours. Figure 2.2 shows how a kernel is used to extrapolate properties of the gas in-between SPH particles. To make use of the Euler equations with this method, they must first be altered to fit the Lagrangian approach. To achieve this, the comoving derivative is introduced as

$$\frac{D}{Dt} = \frac{\delta}{\delta t} + \vec{u} \cdot \vec{\nabla}, \tag{2.3}$$

to convert the equations into the frame of the moving gas element. Examples of SPH codes

include GADGET-2 Springel (2005) and GASOLINE2 Wadsley et al. (2017).

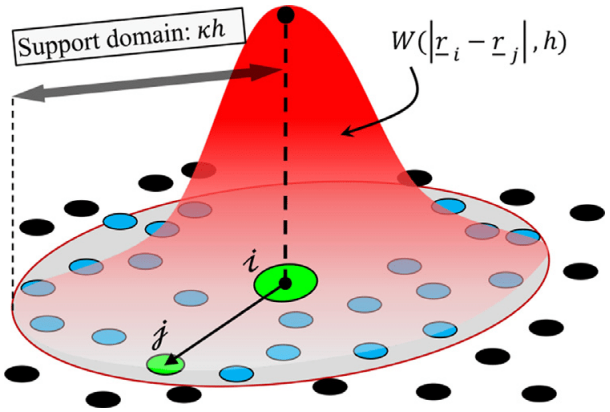

Figure 2.2. SPH convolution using a smoothing kernel W in 2D space (Afrasiabi et al., 2021).

Both methods have been widely used in astrophysical settings, and both have their advantages. AMR has the advantage that entropy is implicitly produced when fluxes of different thermodynamic states are mixed in a cell. It typically handles steep density gradients (Agertz et al., 2007) and captures shocks (Moore et al., 2000) more effectively than SPH. SPH has better treatment of advection of complex density fields and handles gravitational instability driven structure formation more effectively (e.g. Heitmann et al. 2008).

Boundary conditions

The space that simulations occupy is known as the simulation box, which has finite spatial dimensions. As such, a choice must be made as to how the gas is treated at the boundaries of the box. Boundary conditions are non-physical and an author's choice may affect the results. Periodic boundary conditions assume that the simulation box is surrounded by identical boxes, where the gas evolved in time exactly the same in each. In this way, gas exiting through the one boundary will reappear at the other with the same velocity. These conditions work best with a large simulation box where the properties around the boundaries are not important compared to the center of the box. In contrast, reflective boundary conditions assume that gas will undergo an elastic collision with the boundary. Upon contact with the boundary, the sign on the velocity component orthogonal to the boundary is reversed, sending the gas back into the box. This method works well when the gas is supposed to be enclosed within walls. Other examples of boundary conditions include outflow boundaries, where material leaving the box completely disappears, and vacuum boundaries, where the region outside the box is assumed to be empty.

2.1.1 Arepo

The simulations presented in the original work of this thesis were performed with the code Arepo (Springel, 2010), which displays both Eulerian and Lagrangian properties, in that it is a mesh code, but that the mesh is a moving, unstructured, Voronoi tessellation of discrete points (see Figure 2.3). Arepo solves hyperbolic conservation laws of ideal hydrodynamics with a finite volume approach, based on a second-order unsplit Godunov scheme with an exact Riemann solver. Automatic and continuous refinement overcome the challenge of structure growth associated with AMR, yet the Eularian properties overcome poor shock capturing resolution associated with SPH, while remaining Galilean-invariant.

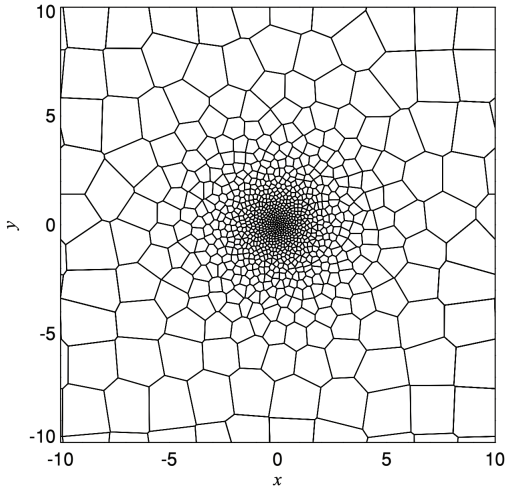

Figure 2.3. Unstructured, Voronoi tessellation of discrete points with Arepo (Springel, 2010)

Ideal MHD is implemented in Arepo by converting the ideal MHD equations into a system of conservation laws as

$$\frac{\delta \vec{U}}{\delta t} + \nabla \cdot (\vec{F}) = 0, \tag{2.4}$$

$$U = \begin{pmatrix} \rho \\ \rho\vec{v} \\ \rho e \\ \vec{B} \end{pmatrix} \quad F(U) = \begin{pmatrix} \rho\vec{v} \\ \rho\vec{v}\vec{v}^T + p - \vec{B}\vec{B}^T \\ \rho e\vec{v} + p\vec{v} - \vec{B}(\vec{v}\cdot\vec{B}) \\ \vec{B}\vec{v}^T - \vec{v}\vec{B}^T \end{pmatrix}, \tag{2.5}$$

where ρ, $\vec{v}$ and $\vec{B}$ are the local gas density, velocity and magnetic field strength, $p = p_{\text{gas}} + \frac{1}{2}B^2$ is the total gas pressure, $e = u + \frac{1}{2}\vec{v}^2 + \frac{1}{2\rho}B^2$ is the total energy, where u is the thermal energy per unit mass. These conservation laws reduce to ideal hydrodynamics when $B = 0$. The equations are solved with a second-order accurate finite-volume scheme (Pakmor et al., 2011).

Numerical schemes tend to suffer from $\nabla \cdot \vec{B}$ errors, which is an issue as electric charges have no magnetic analogues, so the net outflow of the magnetic field through a closed surface is zero. Magnetic fields are therefore solenoidal vector fields, i.e.

$$\nabla \cdot \vec{B} = 0. \tag{2.6}$$

When $\nabla \cdot \vec{B}$ errors arise in numerical simulations it can result in non-physical results, such as plasma transport orthogonal to the magnetic field lines. Constrained transport methods have been developed to restrict $\nabla \cdot \vec{B}$ to 0, but these are restricted to codes with structured grids, unlike the voronoi mesh of AREPO. To solve this, we use hyperbolic divergence cleaning for the MHD equations whereby the divergence constraint is coupled with the conservation laws by introducing a generalized Lagrange multiplier (Dedner et al., 2002). This has the negative effect of removing magnetic energy from the system as a result.

2.1.2 CHEMISTRY

Collapse of primordial gas is closely linked to the chemistry involved (e.g. Glover et al. 2006; Yoshida et al. 2007b; Glover & Abel 2008; Turk et al. 2011). We therefore use a fully time-dependent chemical network to model the gas. We use the same chemistry and cooling as Wollenberg et al. (2020), which is described in the appendix of Clark et al. (2011a), but with updated rate coefficients, as summarised in Schauer et al. (2019). The network has 45 chemical reactions to model primordial gas made up of 12 species: H, H^+, H^-, H_2^+ , H_2, He, He^+, He^{++}, D, D^+, HD and free electrons. Optically thin H_2 cooling is modelled as described in Glover & Abel (2008): we first calculate the rates in the low density ($n \rightarrow 0$) and local thermodynamic equilibrium (LTE) limits, and smoothly interpolate between them as a function of $n/n_{\rm cr}$, where $n_{\rm cr}$ is the H_2 critical density. To compute the H_2 cooling rate in the low density limit, we account for the collisions with H, H_2, He, H^+ and electrons. To calculate the H_2 cooling rate in the optically thick limit, we use an approach introduced by Yoshida et al. (2006), as described in detail in Clark et al. (2011a). Prior to the simulation, we compute a grid of optically thick H_2 cooling rates as a function of the gas temperature and H_2 column density. During the simulation, if the gas is dense enough for the H_2 cooling to potentially be in the optically thick regime ($\rho > 2 \times 10^{-16} \, {\rm g \, cm^{-3}}$), we interpolate the H_2 cooling rate from this table, using the local gas temperature and an estimate of the effective H_2 column density computed using the Sobolev approximation. In addition to H_2 cooling, we also account for several other heating and cooling processes: collisionally-induced H_2 emission, HD cooling, ionisation and recombination, heating and cooling from changes in the chemical make-up of the gas and from shocks, compression and expansion of the gas, three-body H_2 formation and

heating from accretion luminosity. For reasons of computational efficiency, the network switches off tracking of deuterium chemistry* at densities above 10^{-16} g cm^{-3}, instead assuming that the ratio of HD to H_2 at these densities is given by the cosmological D to H ratio of 2.6×10^{-5}. The adiabatic index of the gas is computed as a function of chemical composition and temperature with a Harten-Lax-van Leer with contact and Alfvén mode (HLLD) Riemann solver.

For simulations where an external radiation field is used (see Chapter 6) we use the radiation field expected from massive Pop III stars. As in Schauer et al. (2021), we use a blackbody spectrum at temperature 10^5 K for energies below 13.6 eV. Above this energy, the flux is expected to drop due to absorption in the intergalactic medium, so we set the value of the radiation field to 0 above 13.6 eV. We model the effects of H_2 self-shielding using the TreeCol algorithm (Clark et al., 2012).

2.1.3 Sink particles

The Jeans length λ_J of a structure of given density and temperature marks the maximum size it can achieve before thermal pressure cannot prevent gravitational collapse. Artificial fragmentation occurs in hydrodynamic codes if the local λ_J falls below the size of mesh cells Δx. The Truelove condition (Truelove et al., 1997) requires a Jeans number $\Delta x/\lambda_\text{J}$ of 0.25 or less, corresponding to at least 4 cells spanning across any λ_J, to prevent artificial fragmentation. This requirement is increased to 30 cells per Jeans length for magneto-hydrodynamical (MHD) simulations, in order to capture dynamo amplification of the magnetic field (Federrath et al., 2011a). AMR codes can refine the mesh based on the local λ_J to meet this resolution criteria.

Another condition for numerical stability is known as the Courant condition (Courant et al., 1952), which states that information must not be allowed to travel further than the cell length during a timestep, such that information from a cell can only be communicated to its immediate neighbours. As a result, the timestep has to decrease as the mesh becomes more refined.

Numerical simulations cannot refine indefinitely. As the gas gets denser (decreasing λ_J), the number of cells increases. These new cells are smaller and require smaller timesteps to satisfy the Courant condition, making it increasingly computationally expensive to run to higher densities. Sink particles (Bate et al., 1995; Federrath et al., 2010) provide an alternative to indefinite refinement. They are non-gaseous particles that contain all of the mass within the volume they occupy and can accrete matter from their surrounding cells. As they cannot fragment – either naturally or artificially – their implementation at high densities overcomes the problem posed by the Jeans refinement criterion.

*Note that HD cooling continues to be included in the model.

The sink particle implementation we use in AREPO was introduced in Wollenberg et al. (2019) and Tress et al. (2020). Briefly, a cell is converted into a sink particle if it satisfies three criteria: 1) it reaches a threshold density; 2) it is sufficiently far away from pre-existing sink particles so that their accretion radii do not overlap; 3) the gas occupying the region inside the sink is gravitationally bound and collapsing. Likewise, for the sink particle to accrete mass from surrounding cells the gas must meet two criteria: 1) the cell lies within the accretion radius; 2) it is gravitationally bound to the sink particle. A sink particle can accrete up to 90% of a cell's mass, above which the cell is removed and the total cell mass is transferred to the sink.

The sink particle treatment also includes the accretion luminosity feedback from Smith et al. (2011). However, we do not include a treatment for internal luminosity, so our simulations are only valid until a time when the core is expected to begin propagating its accumulated heat as a luminosity wave.

2.1.4 Sink mergers

As part of the original work presented in this thesis, sink particle merging has been implemented into AREPO. This addition was motivated by previous Pop III studies which have shown that merging of dense objects is important to the outcome of the system. For example, Greif et al. (2012) found that about half of the secondary protostars which formed in the disc migrated to the centre of the cloud in a free-fall time, where they merge with the primary protostar, boosting its mass to five times higher than the second most massive protostar. Hirano & Bromm (2017) found that fragments efficiently migrate to the primary protostar until the central star evacuates the surrounding gas by its radiation. Fragments large enough to form black holes may even merge generating an observable gravitational wave signal. More recently Susa (2019) noted a rapid merging phase once the disc fragments.

Similarly to Federrath et al. (2010), we allow sinks to merge if they fulfil four criteria: 1) they lie within each other's accretion radius; 2) they are moving towards each other; 3) their relative accelerations are < 0; and 4) they are gravitationally bound to each other. Since sink particles carry no thermal data, the last criteria simply requires that their gravitational potential well exceeds the kinetic energy of the system. When these criteria are met, the larger of the sinks gains the mass and linear momentum of smaller sink, and its position is shifted to the center of mass of the system. We allow multiple mergers per time-step, based on mass hierarchy; for example, if sink A is flagged to merge into sink B, and sink B is flagged to merge into sink C, then both A and B will be merged into sink C simultaneously.

We have tested sink merging routine with a set-up inspired by Burkert & Bodenheimer (1993)

and Boss & Bodenheimer (1979). A rotating sphere of pure hydrogen at density 1.44×10^{-17} g cm^{-3} of radius 3.2×10^{16} cm and temperature 10 K is given angular velocity 1.6×10^{-12} s^{-1} and density perturbations to trigger fragmentation. We repeat the simulation for 2 and 4 fragments. The density perturbations around the azimuthal angle about the rotational axis ϕ for 2 and 4 fragments are given by

$$\begin{aligned} \rho &= \rho_0[1 + 0.5\cos 2\phi] \\ \rho &= \rho_0[1 + 0.5\cos 4\phi] \end{aligned} \tag{2.7}$$

respectively. We repeated the simulations with and without sink mergers enabled. The results are shown in Figure 2.4. In the 2 fragment case with sink mergers enabled, the 2 fragments quickly form sinks and merge when they meet in the center. Likewise, without sink mergers enabled, the 2 sink particles lie on top of one another, indicating that merger was legitimate. For the 4 fragment case, the sinks form 2 binaries and do not merge regardless of if sink mergers is enabled, indicating that the sink merger routine correctly assesses when and when not to merge.

2.2 Random field generator

It is often useful to generate random 3D vector fields which are statistically similar to physical fields in the Universe. This can be done if the power spectrum of the desired field is known. A power spectrum represents the energy of a field at different spatial scales as a function of k, which typically represents the number of wavelengths that can fit within the simulation box side length L. For example, to generate a velocity field with the characteristics of pure compressible Burgers turbulence, the power spectrum goes as k^{-2} (Burgers, 1948), while pure incompressible Kolmogorov turbulence goes as $k^{-5/3}$ (Kolmogorov, 1941). Similarly, to generate a magnetic field which has undergone the small-scale turbulent dynamo process (see Section 1.3.5), the power spectrum goes as $k^{3/2}$ (Kazantsev, 1968).

The method of generating a 3D field $B_{x,y,z}$ from a 1D power spectrum P_k is as follows; the 1D spectrum is converted to 3D k-space, where k is the number of cycles per boxsize, spanning from 0-N in 3 dimensions, where N is the number of desired modes. The energies of each $k_{\alpha,\beta,\gamma}$ coordinate are given by dividing P_k by the shell volume $4\pi|k_{\alpha,\beta,\gamma}|^2 dk$ to give $P_{\alpha,\beta,\gamma}$. These energies are the squared amplitudes of the waves i.e. $\sqrt{P_{\alpha,\beta,\gamma}} = |B_{\alpha,\beta,\gamma}|$, which are split between the 3 spatial dimensions to give a vector field in k-space $\vec{B}_{\alpha,\beta,\gamma}$. Spatial dimensions split the energy

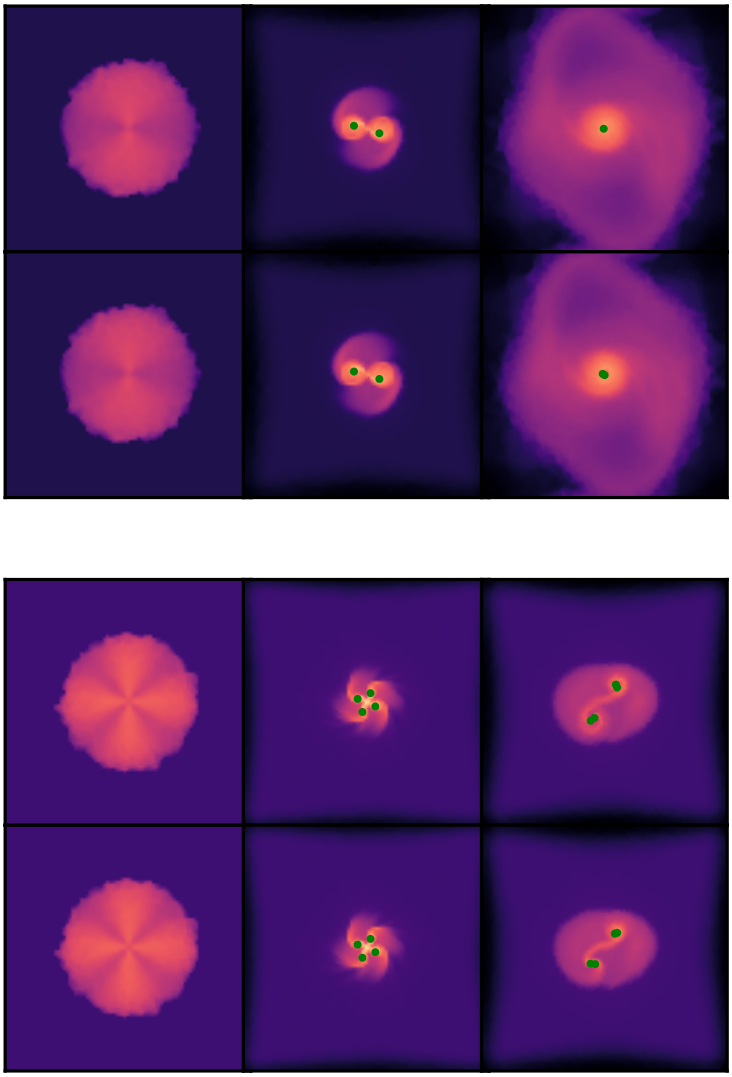

Figure 2.4. Comparison between merging behaviour with sink mergers enabled (upper panel) versus disabled (lower panel) for binary perturbations encouraging 2 (top) and 4 (bottom) fragments. Sink particles are shown as green dots.

equally, each having amplitude $\sqrt{1/3\ P_{\alpha,\beta,\gamma}}$. The modes are given random phase offsets $\phi_{\alpha,\beta,\gamma}$ as

$$B_{\alpha,\beta,\gamma} = |B_{\alpha,\beta,\gamma}|[\cos(\phi_{\alpha,\beta,\gamma}) + \sin(\phi_{\alpha,\beta,\gamma})i] \tag{2.8}$$

and converted into 3D real space as $B_{x,y,z}$ via inverse Fourier transform. The field is then interpolated onto the AREPO cell coordinates and rescaled to give the desired rms strength.

Chapter 3

Resolution study

As the amount of ionising radiation a star emits and its eventual fate is dependent on its mass, the IMF of Pop III stars has a huge effect on the evolution of the Universe. Existing attempts to produce the primordial IMF differ considerably in terms of the maximum density their simulations run to, which is directly linked to the maximum resolution of the simulation. The work presented in this section is presented in Prole et al. (2022a) and explores the effects of increasing the maximum density of Pop III star formation simulations, starting from a point where H_2 cooling renders the cloud $\sim$200 K at scales of $\sim$1 pc.

3.1 Mesh refinement

In present day star formation simulations, the sink creation density is chosen to be that of the first adiabatic core. As laid out in Larson (1969), the initial isothermal collapse of a cloud is halted in the central region when the gas becomes opaque to outgoing radiation. At $\rho \sim 10^{-10}$ g cm^{-3}, the central temperature and density are such that collapse stops in the central region, forming the first adiabatic core, while the material outside the core continues to freefall isothermally. At this point the core is stable to further fragmentation. The radial density profile inside the core is flat and extends out to $\lambda_{\rm J}$, so the radius of the of sink particle is chosen to be the Jeans length at the creation density and temperature.

The most important source of the opacity that halts collapse and prevents fragmentation in the first core is dust grains (Low & Lynden-Bell, 1976), which are not present in primordial star formation. In this regime, there is no clear 'first core', as is apparent from the thermal evolution described in e.g. Omukai et al. (2005). Referring to Figure 3.1, primordial gas is cooled to $\sim$200 K at $\sim 10^{-20}$g cm^{-3} by molecular hydrogen cooling (A). Gravitational collapse allows the gas

temperature to rise from 200 K to 1000 K by 10^{-15}g cm^{-3} (B). Here three-body reactions convert most of the hydrogen into molecules. At 10^{-12}g cm^{-3}, the H_2 cooling rate decreases due to gas opacity (C), but collision-induced emission kicks in to become the dominant cooling process at 10^{-10}g cm^{-3} (D). Once the temperature reaches 2000 K at 10^{-8}g cm^{-3}, dissociation of H_2 molecules provides effective cooling (E) until it is depleted and the collapse becomes almost adiabatic at 10^{-4}g cm^{-3} (F).

Running simulations up to this density with a full chemical treatment lies beyond current computational capabilities. The appropriate density to replace gas with a stable sink particle is unclear, but the gas must be stable to fragmentation. Gammie (2001) suggested that discs become stable to fragmentation when heating from turbulence is balanced by cooling. Smith et al. (2011) studied the stability of Pop III collapses against fragmentation during the early period of protostar formation, before ionising radiation from the star becomes important, where accretion luminosity feedback is the main opposition to fragmentation. They found that accretion luminosity delays fragmentation but does not prevent it.

The sink particle creation density varies between different studies. For example, Stacy et al. (2010), Stacy et al. (2012), Clark et al. (2011a), Susa et al. (2014) and Sharda et al. (2020) all introduce sinks at densities $\sim 10^{-12}$–$10^{-11}\ \mathrm{g\,cm^{-3}}$, in analogy with present day star formation, while Smith et al. (2011), Stacy et al. (2016) and Wollenberg et al. (2019) introduce them at $\sim$$10^{-9}$g cm^{-3}, above which there are no chemical heating terms that can prevent the gas from collapsing. Among the highest resolution Pop III studies, Greif et al. (2011b), Clark et al. (2011b) and Hartwig et al. (2015b) introduce their sink particles at $\sim$$10^{-7}$g cm^{-3}.

Sink particles are not a perfect solution to the indefinite refinement problem, and an author's choice of sink particle creation density may change the morphology of the resulting cluster. Therefore, some authors have used other approaches to address this problem. For example, Greif et al. (2012) ran several simulations without sinks by simply following the collapse of the gas up to the density of $10^{-4}\ \mathrm{g\,cm^{-3}}$ at which the further collapse becomes adiabatic. The disadvantage of this approach is that despite a considerable investment of computing time, the simulations could only follow the first 10 yr of the evolution of the system after the formation of the first protostar. Hirano & Bromm (2017) avoided this difficulty by artificially suppressing cooling above a pre-chosen threshold density, resulting in the gas evolving adiabatically above this density. They examined several different threshold densities ranging from $\sim 10^{-14}\ \mathrm{g\,cm^{-3}}$ to $\sim 10^{-9}\ \mathrm{g\,cm^{-3}}$, and showed that this allowed them to run the simulations for periods of several hundred years (in the high threshold case) to several tens of thousands of years (in the low threshold case) after the formation of the first protostar. However, a disadvantage of this suppressed-cooling approach is that the pressure-supported clumps that form in these simulations have sizes that are much larger than those of real Pop III protostars. For example, the clumps formed in their simulations with

Table 3.1. Sink creation density, temperature (Figure 3.1), sink radius, minimum cell volume and minimum gravitational softening lengths used in the study.

$\rho_{\rm sink}$ [g cm^{-3}]	T [K]	$R_{\rm sink}$ [cm]	$V_{\rm min}$ [cm^3]	$L_{\rm soft}$ [cm]
10^{-10}	3050	1.37×10^{14}	5.10×10^{39}	1.72×10^{13}
10^{-9}	3350	4.56×10^{13}	1.86×10^{38}	5.70×10^{12}
10^{-8}	3750	1.53×10^{13}	6.95×10^{36}	1.91×10^{12}
10^{-7}	4100	5.05×10^{12}	2.51×10^{35}	6.31×10^{11}
10^{-6}	4460	1.67×10^{12}	9.03×10^{33}	2.08×10^{11}

the highest threshold density have sizes of $\sim$ 10–60 AU, much larger than the physical size of ~ 0.5 AU that we expect for massive pre-main sequence Pop III stars. How well the behaviour of these artificially large clumps represents the behaviour of real Pop III protostars remains unclear.

In view of these limitations of current sink-free approaches, sink particles remain an essential tool for exploring Population III star formation past the point of the initial collapse and assessing the resulting primordial IMF.

3.1.1 Sink particles

Sink particles are point masses inserted into the mesh to prevent artificial collapse when the local Jeans length falls below the minimum cell size of the mesh. The accretion radius of a sink particle $R_{\rm sink}$ is chosen to be $\lambda_{\rm J}$ corresponding to the sink creation density, given by

$$\lambda_{\rm J} = \sqrt{\frac{k_B T}{G\rho_{\rm sink}(\mu m_{\rm p})}}. \tag{3.1}$$

where k_B is the Boltzmann constant, T is the temperature, $\rho_{\rm sink}$ is the sink creation density, μ is the mean molecular weight and $m_{\rm p}$ is the mass of a proton. To estimate $\lambda_{\rm J}$ before running the simulation, a realistic value of T at $\rho_{\rm sink}$ is needed. To achieve this, a non-turbulent version of the simulations described in Section 3.3 was run, resulting in a single star. The simulation was run up until the maximum density reached 10^{-4}g cm^{-3}. Figure 3.1 shows the resulting relationship between density and temperature. This gives an effective relationship between ρ and $\lambda_{\rm J}$ using Equation 3.1. The sink radius $R_{\rm sink}$ is given by $\lambda_{\rm J}$. We set the minimum cell length to fit 16 cells across the sink particle in compliance with the Truelove condition, giving a minimum cell volume $V_{\rm min} = (R_{\rm sink}/8)^3$. The minimum gravitational softening length for cells and sink particles $L_{\rm soft}$ is set to $R_{\rm sink}/8$. The values of $\rho_{\rm sink}$, T, $R_{\rm sink}$, minimum cell volume and minimum gravitational softening lengths are given in Table 3.1.

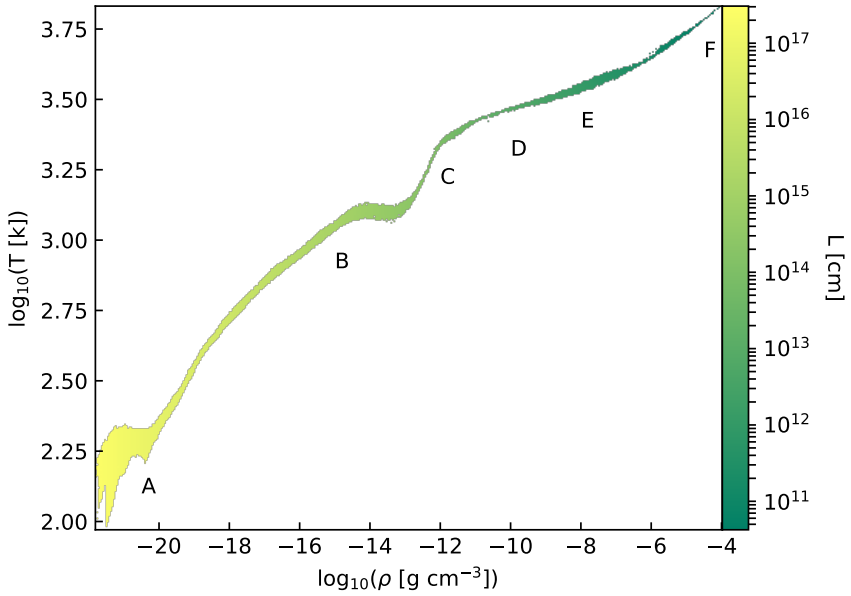

Figure 3.1. Relationship between density and temperature during a purely gravitational collapse, resulting in a single central dense object. The temperatures were used to calculate the parameters in Table 3.1. Shown in colour are the cell lengths as dictated by the chosen refinement criterion of 16 cells per Jeans length.

3.2 Chemistry

We use the same chemistry and cooling as Wollenberg et al. (2019), which is based on the fully time-dependent chemical network described in the appendix of Clark et al. (2011a), but with updated rate coefficients, as summarised in Schauer et al. (2017). The network has 45 chemical reactions to model primordial gas made up of 12 species: H, H^+, H^-, H_2^+ , H_2, He, He^+, He^{++}, D, D^+, HD and free electrons. Included in the network are: H_2 cooling (including an approximate treatment of the effects of opacity), collisionally-induced H_2 emission, HD cooling, ionisation and recombination, heating and cooling from changes in the chemical make-up of the gas and from shocks, compression and expansion of the gas, three-body H_2 formation and heating from accretion luminosity. For reasons of computational efficiency, the network switches off tracking of deuterium chemistry* at densities above 10^{-16} g cm^{-3}, instead assuming that the ratio of HD to H_2 at these densities is given by the cosmological D to H ratio of 2.6×10^{-5}. The adiabatic index of the gas is computed as a function of chemical composition and temperature with the Arepo HLLD Riemann solver.

*Note that HD cooling continues to be included in the model.

3.3 Initial conditions

Primordial cloud collapse simulations were performed for 3 initial turbulent velocity seed fields (hereafter referred to as A, B and C) and 2 initial ratios of kinetic to gravitational energies α. A resolution study was performed for the lower α set-up, where we ran simulations with 5 different values for the sink particle creation density (see Table 3.1) for each of the different seed fields. In these simulations, the rms turbulent velocity was scaled to give a ratio of kinetic to gravitational energy of $\alpha = 0.05$, to give a weak velocity field which encourages a more straightforward collapse onto a central object. We also performed higher velocity ($\alpha = 0.25$) versions of the highest resolution runs, giving 18 simulations in total. We generate random velocity fields from the turbulent power spectrum $P(k) \propto k^{-2}$. The initial conditions are similar to those of Wollenberg et al. (2019), consisting of a stable Bonner Ebert sphere (Ebert, 1955; Bonnor, 1956), categorised by radius $R_{\mathsf{BE}} = 1.87$ pc and central density $\rho_c = 2{\times}10^{-20}$g cm^{-3}, which was enhanced by a factor of 1.87 to promote collapse, giving a total mass of 2720M$_\odot$ enclosed. The sphere was placed in a box of side length $4R_{\mathsf{BE}}$ with an initial temperature of 200 K and the simulations were performed with refinement criteria of 16 cells per Jeans length. The chemistry used was the same as Clark et al. (2011a), with initial abundances for H_2, H^+, D^+ and HD of $x_{H_2} = 10^{-3}$, $x_{H^+} = 10^{-7}$, $x_{D^+} = 2.6{\times}10^{-12}$ and $x_{\mathsf{HD}} = 3{\times}10^{-7}$, respectively.

3.4 Fragmentation behaviour

Density projections for seed field A are shown at 0, 100, 200 and 400 years after the formation of the first sink in Figure 3.2. The increase in structure and fragmentation is clear as the simulation resolution is increased. Figure 3.3 shows the evolution of N_{sink} and M_{tot} with time in the simulations making up our resolution study. We see that for all three seed fields, the total number of sinks formed increases with increasing ρ_{sink} without achieving numerical convergence.

Higher maximum gas density lowers the minimum Jeans scale and allows gravitational instabilities on smaller spatial scales, resulting in more fragmentation of the gas. As there are no new chemical reactions introduced for densities above 10^{-8}g cm^{-3}, this implies that fragmentation will continue to increase with increasing resolution until the gas becomes almost adiabatic at 10^{-4}g cm^{-3}, at which point it should be stable to fragmentation assuming the parallels with present day star formation hold. This means that all Pop III studies to date have underestimated the number of stars formed in their halos. However, the total mass of the system is unaffected by increased resolution, so estimates of the mass in stars within dark matter halos can be made with fairly low resolution simulations.

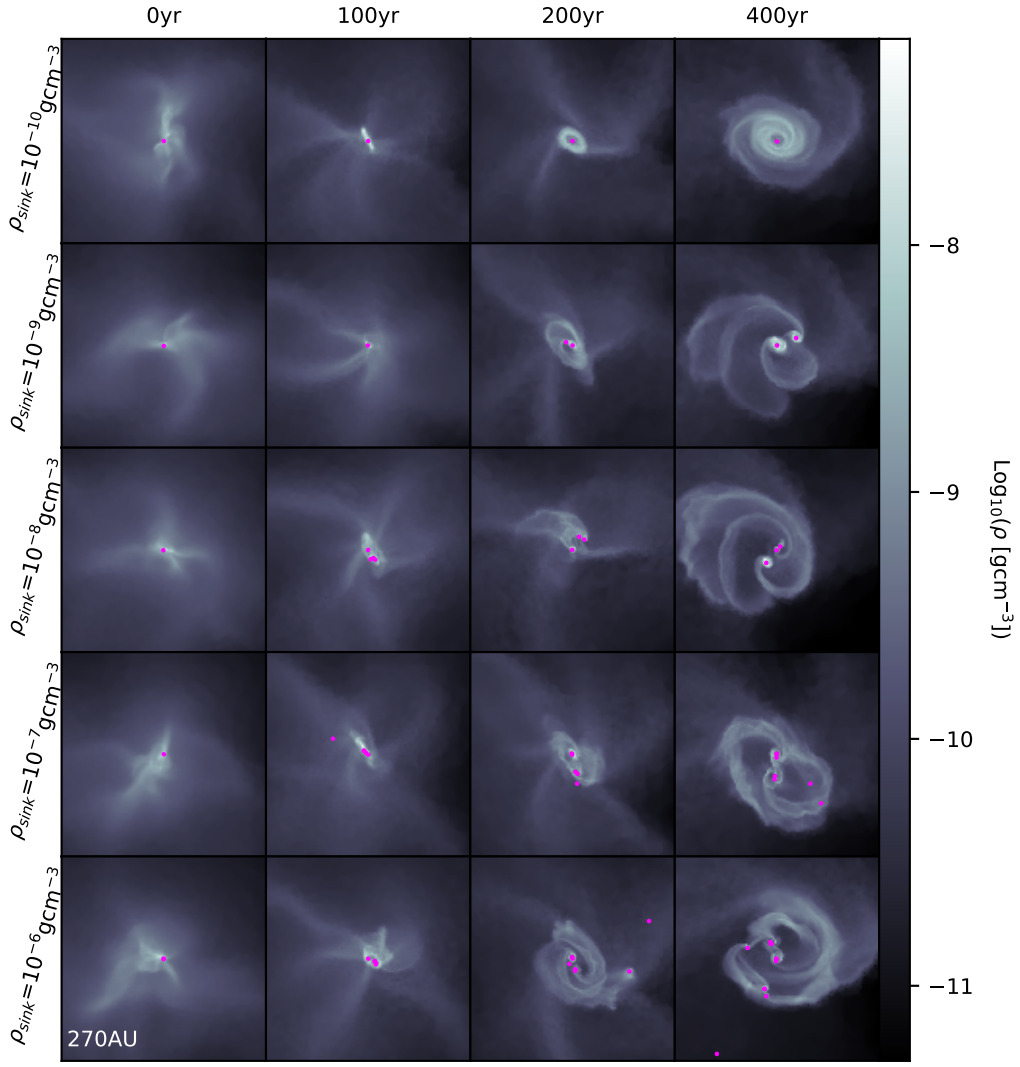

Figure 3.2. For initial velocity field A, the inner 270 AU of the AREPO unstructured density distributions projected onto uniform 500^3 grid cubes, flattened by summing the density over the z-axis. From left to right, we show snapshots taken at 0, 100, 200 and 400 years after the formation of the first sink particle, for sink creation densities ranging from $\rho_{\rm sink} = 10^{-10}\,{\rm g\,cm^{-3}}$ (top row) to $10^{-6}\,{\rm g\,cm^{-3}}$ (bottom row). Sink particles are shown as magenta dots.

Figure 3.4 compares the outcome of the $\alpha = 0.05$, $\rho_{\rm sink} = 10^{-6}$ g cm^{-3} simulations with that of the corresponding runs with $\alpha = 0.25$. Seed field B shows that the structure of the systems can be drastically different (likely due to the sudden burst in star formation at 100 yr in the low

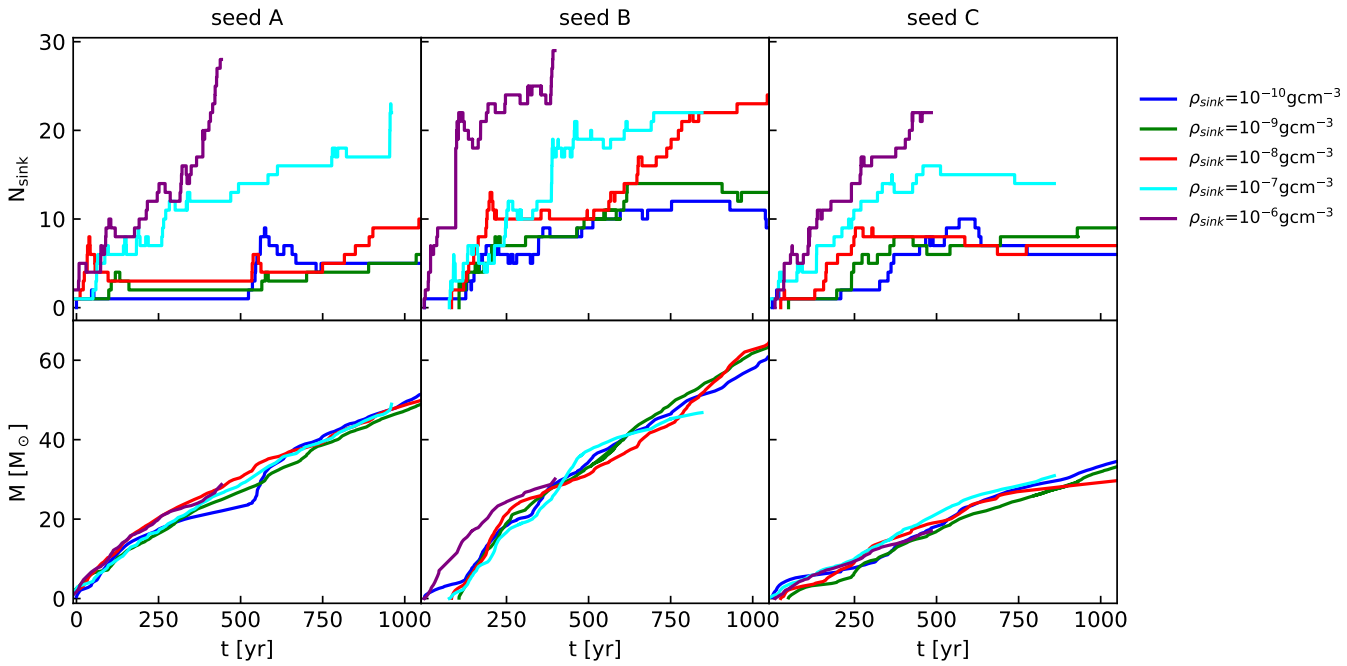

Figure 3.3. Time evolution of the number of sinks ($N_{\rm sink}$) and the total mass M in sinks for $\rho_{\rm sink} = 10^{-10}$-$10^{-6}$g cm^{-3}. Note that decreasing $N_{\rm sink}$ indicates sink merging.

velocity case), while seed C shows that the ejection history can change. Despite these differences, it is clear that the high degree of fragmentation seen in the low velocity runs remains when the velocity fields are boosted to higher strengths. This demonstrates that the lack of convergence in the fragmentation in the resolution test was not a product of our choice of α, but rather is a general result.

Figure 3.5 shows the IMF at ∼400 yr after the formation of the first sink. The systems are compared at the same time so that their total mass in sinks are the same, as this does not vary with resolution (see Figure 3.3). The IMFs show that the group shifts to a lower mass population with increasing resolution. The shaded regions represent ejections, which are discussed in Section 3.4.1. Since accretion onto ejected sinks is halted due to a lack of dense gas, their position on the IMF is fixed. The remaining sinks will continue to accrete, as only a small fraction of the total mass of the cloud has been accreted at 400 yr.

Figure 3.6 shows the time evolution of the IMF and normalised cumulative mass distribution for $\rho_{\rm sink} = 10^{-6}\,{\rm g\,cm^{-3}}$, combining the sinks from the $\alpha = 0.05$ and $\alpha = 0.25$ runs. By 400 yr, the shape of the IMF appears to be showing convergence.

The present day IMF is bottom-heavy, with most of its mass in low mass stars (e.g. Kroupa & Jerabkova 2019). The primordial IMFs produced in this study span a similar range to the present

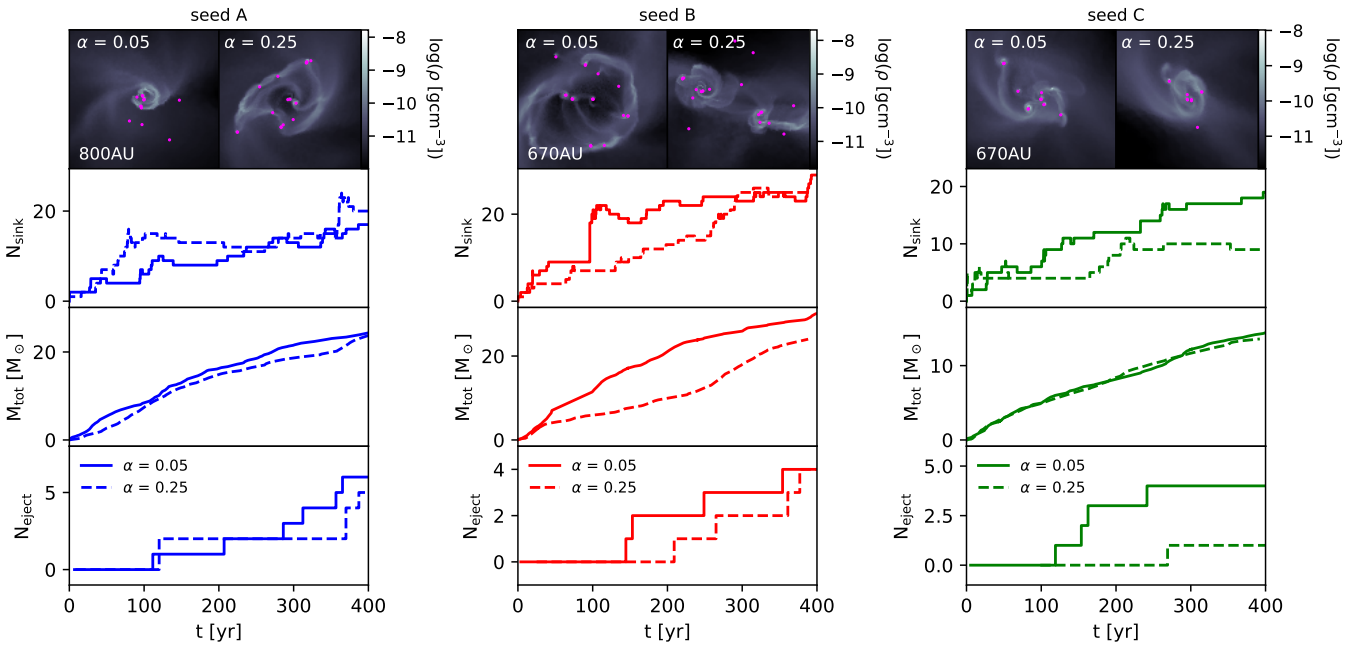

Figure 3.4. Top to bottom: Comparisons of the system for $\alpha = 0.05$ and $\alpha = 0.25$ at 400 yr after the formation of the first sink for seeds A, B and C. We compare the number of sinks formed, the total mass in sinks, and the number of sinks ejected from the system as a function of time, for $\alpha = 0.05$ (solid lines) and $\alpha = 0.25$ (dashed lines).

day IMF, but most of the mass is in high mass stars. This top-heavy IMF has been produced in many other Pop III studies (e.g. Schneider et al. 2006; Susa et al. 2014; Stacy et al. 2016; Wollenberg et al. 2019; Sharda et al. 2020).

More sink particles means more competition for mass accretion, hence lower accretion rates onto the central sink. Figure 3.9 shows the mass and accretion rate onto the most massive sink. As the maximum resolution increases, the central sink is starved by the increasingly large number of secondary stars which compete to accrete material that would otherwise fall onto the primary star, resulting in a lower mass central star. This process has been termed 'fragmetnation-induced starvation' (Peters et al., 2010). It is not seen perfectly in all of our simulations, as major merger events are capable of boosting the mass of the most massive sink to converge with, or surpass the mass of its lower resolution counterpart. For example, within the seed field A runs, the highest resolution run converges due to a major merger.

Even within this small set of initial velocity fields, the mass of the largest sink particle shows natural variance. The IMFs of Wollenberg et al. (2019) indicate that turbulent set-ups with lower initial rotation produce higher mass stars. Figure 3.8 illustrates the initial ratio of angular to total velocity around the region where the first sink particle later forms. Although we do not explicitly introduce rotation in our simulations, the turbulent velocity field generates some non-zero amount

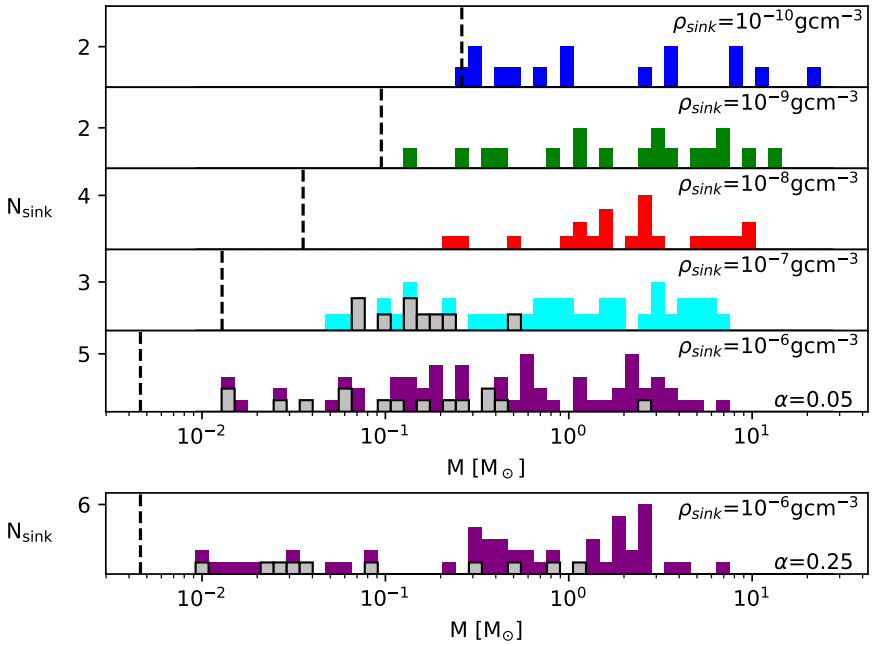

Figure 3.5. Initial mass functions at $t \sim 400$ years after the formation of the first sink. The distribution of masses shifts towards lower values with increasing $\rho_{\rm sink}$. The shaded sections of the IMFs represent sinks ejected from the group, given by the criteria described in Section 3.4.1. The black vertical dashed lines show the Jeans mass at the sink particle creation density. The IMF for the high velocity ($\alpha = 0.25$) run is given in a separate panel at the bottom. Note that for $\rho_{\rm sink} = 10^{-10} - 10^{-8}$ g cm^{-3} there are no ejections.

of angular momentum, and we see from the figure that the runs with lower rotational velocity components indeed produce more massive central sink particles.

3.4.1 Ejections

Previous Pop III studies have shown that ejections from the system due to close encounters are common (e.g. Smith et al. 2011; Greif et al. 2012; Machida & Doi 2013; Wollenberg et al. 2019). Typically once a protostar is ejected from the cloud, it is removed from its accretion source and its ejection mass represents the final mass. We systematically identify ejected sinks by calculating the escape velocity of all sinks, as given by

$$v_{\rm esc} = \sqrt{\frac{2GM}{R}}, \tag{3.2}$$

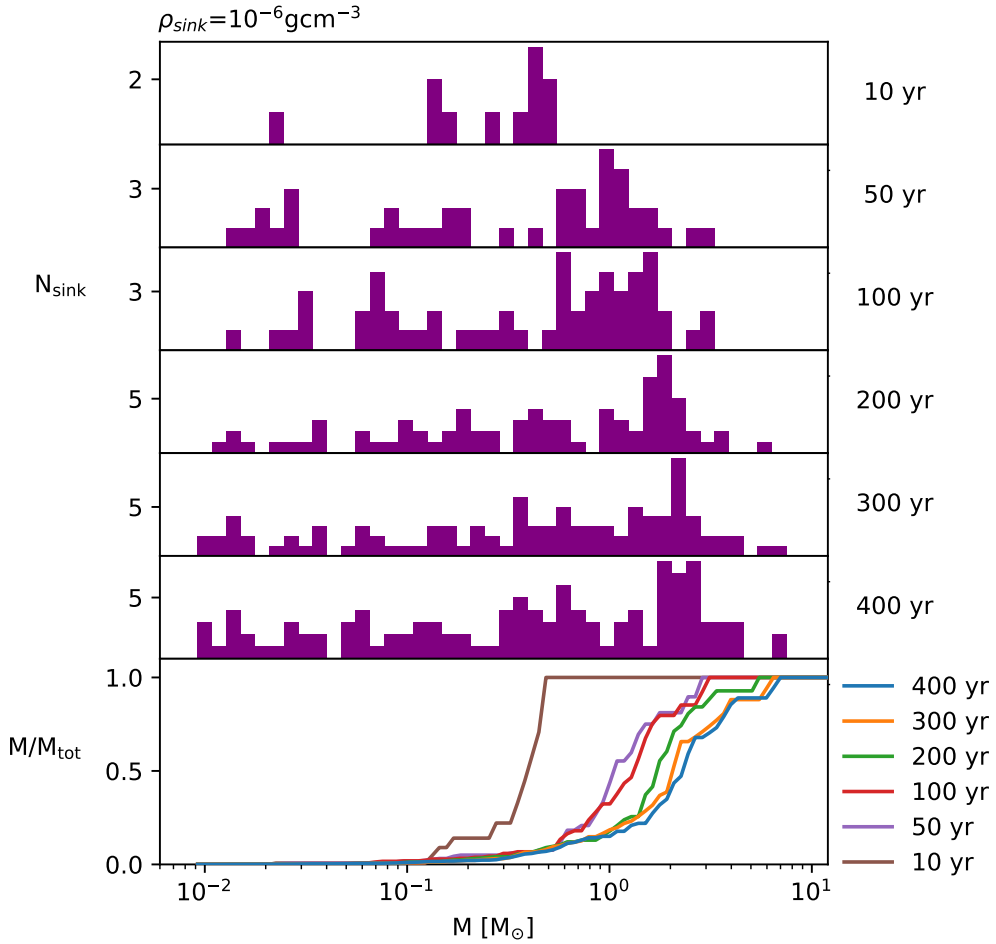

Figure 3.6. Evolution of the IMF and cumulative mass function at times 10, 50, 100, 200, 300 and 400 yr after the formation of the fist sink, for $\rho_{\rm sink} = 10^{-6}\,{\rm g\,cm^{-3}}$. The IMFs combine the sinks from the $\alpha = 0.25$ and $\alpha = 0.05$ runs.

where R is the distance of the sink from the center of mass of the complete set of sinks, which acts as a proxy for the center of the halo[†]. M is the total mass of gas and sinks within a sphere of radius R surrounding this centre of mass. The sink particle is counted as ejected if its velocity exceeds the escape velocity and R exceeds 600 AU. The ejection fraction is given by

$$f_{\rm eject} = \frac{\Sigma N_{\rm eject}(M)}{\Sigma N(M)}, \tag{3.3}$$

[†]We choose to use the centre of mass of the sinks rather than that of the gas cells for numerical convenience – there are far fewer sinks than gas cells. However, as the most massive sinks typically remain close to the centre of the halo, our results should be insensitive to this choice. We also note that the effects of dark matter are negligible at these scales.

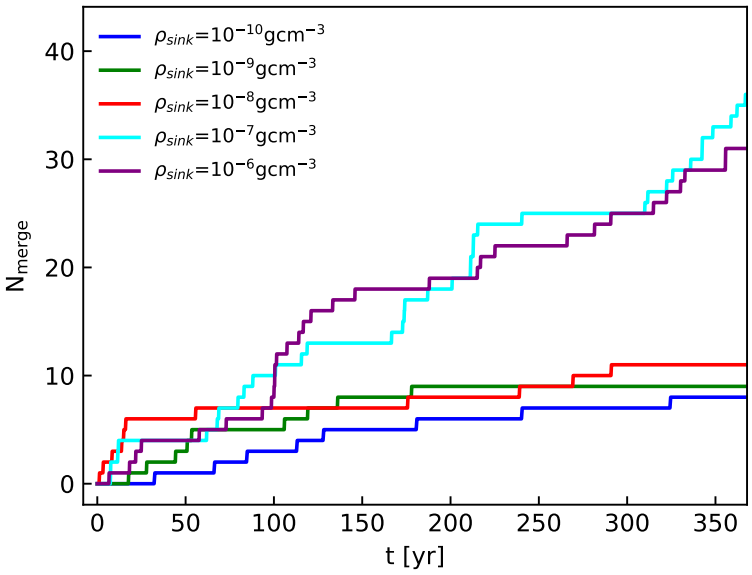

Figure 3.7. Cumulative number of sink particle mergers plotted against time across all velocity seeds.

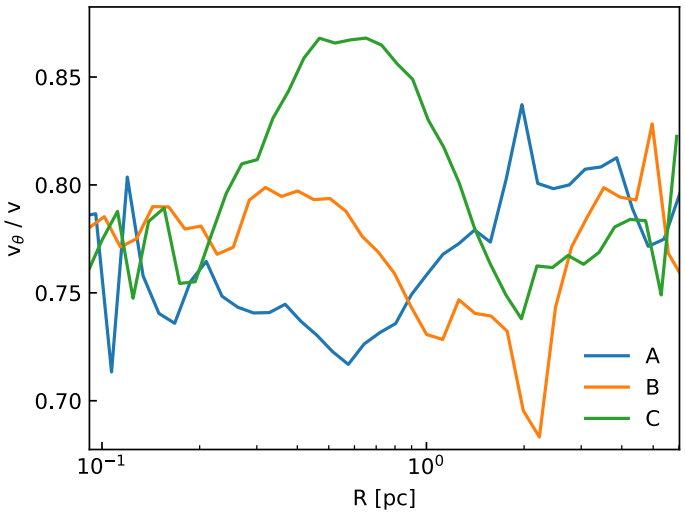

Figure 3.8. Radial profiles of the ratio of angular to total velocity in the initial velocity field, around the region where sink particles later form.

where $N_{\text{eject}}(M)$ and $N(M)$ are the number of ejections and total sinks at mass M, and the summations cover a range of stellar masses. Zero metallicity stars with initial masses in the range 0.075–0.8 M$_\odot$ have lifetimes longer than the age of the Universe (Marigo et al., 2001). These stars should therefore be alive today, while stars with masses above 0.8 M$_\odot$ will have depleted their fuel. The ejection histories of the highest resolution runs are shown in the bottom panel

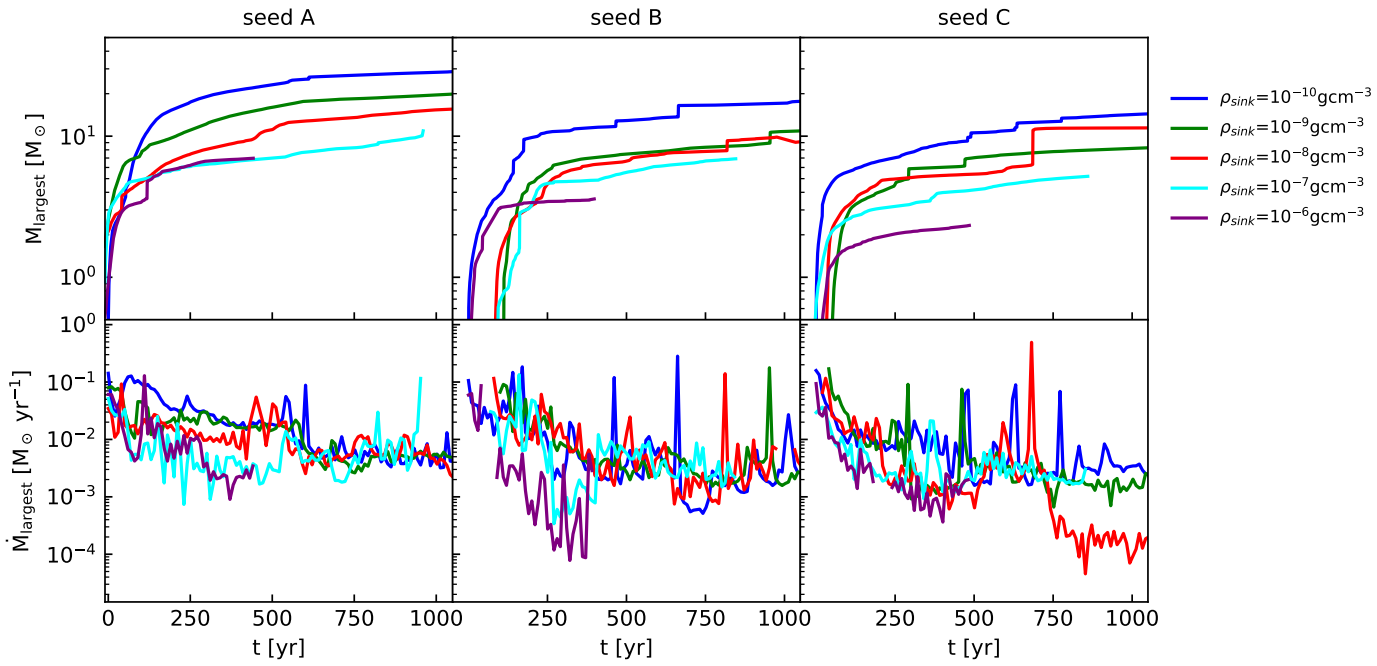

Figure 3.9. Time evolution of the mass and accretion rate onto the most massive central sink.

of Figure 3.4. The ejection fractions for the highest resolution runs across the 3 seed fields and 2 velocity strengths at $t = 400$ yr after the formation of the first sink are given in Table 3.2. We combine all of the sink particles across these 6 highest resolution runs to calculate the mean ejection fractions. We find that sinks of mass below 0.075 $M_\odot$ have a mean ejection fraction of 0.42. These ejected sinks are expected to remain as brown dwarfs for the duration of their lifetimes. The mean ejection fraction for masses between 0.075–0.8 $M_\odot$ was 0.21. These stars are expected to be alive today. Finally, the mean ejection fraction for sinks larger than 0.8 $M_\odot$ was 0.06, which represents stars which have already died by the present day. Table 3.2 also demonstrates that there is significant run-to-run scatter around these mean values. Ejected sinks are shown by the shaded regions of the IMFs in Figure 3.5.

The typical halo size is larger than we have simulated in this study (e.g. Bromm et al. 2002). However, we argue that since $v \gg v_{\rm esc}$ for most of the ejected sinks, accretion will only be significant close to the centre of the halo. The Bondi-Hoyle accretion rate is given by

$$\dot{M} = 4\pi(GM)^2\rho/(c_s^2 + v^2)^{3/2}, \tag{3.4}$$

where M is the sink mass, ρ is the gas density, $c_{\rm s}$ is the sound speed and v is the velocity of the sink relative to the gas. If $v \gg v_{\rm esc}$, then it follows that $v \gg c_{\rm s}$ and that the velocity of the sink

Table 3.2. Ejection fractions for brown dwarfs, stars with masses $<0.8M_\odot$ and stars with masses $>0.8M_\odot$, for the 10^{-6}g cm^{-3} runs, at 400 yr after the formation of the first sink.

Seed	α	$f_{\rm eject}^{\rm BD}$	$f_{\rm eject}^{<0.8M_\odot}$	$f_{\rm eject}^{>0.8M_\odot}$
A	0.05	0.67	0.41	0
A	0.25	0.75	0	0.33
B	0.05	0.29	0.09	0.09
B	0.25	0.22	0.40	0
C	0.05	0.67	0.22	0
C	0.25	0	0.25	0
All	-	0.42	0.21	0.06

will not significantly change as it makes its way out of the halo. Therefore, it follows that

$$\dot{M} \propto \rho. \tag{3.5}$$

Previous work has shown that $\rho \propto r^{-2.2}$ (e.g. Yoshida et al. 2006), so for a constant velocity,

$$\dot{M} \propto t^{-2.2}. \tag{3.6}$$

The mass accretion rate therefore drops rapidly with time and the total mass accreted is dominated by accretion close to t = 0. Therefore, the mass that the ejected protostars have accreted in the region that we simulate is the majority of the mass they are ever going to accrete. Hence even if we were to account for the gas on scales larger than a few pc in the minihalo, this would not significantly affect our conclusion regarding the masses of the ejected protostars.

3.4.2 Accretion luminosity radiation

Figure 3.9 shows that the accretion rate onto the largest sink is initially $\sim 10^{-1} M_\odot {\rm yr}^{-1}$ for all resolutions and all three seed fields, but that it drops rapidly to $\sim 10^{-2} M_\odot {\rm yr}^{-1}$ or below within a few hundred years. Given the high accretion rates, it is also interesting to ask whether the contribution made to the ionising flux by accretion onto the protostars is ever significant. To investigate this, we estimate the number of ionising photons emitted per second due to accretion using the following prescription. We first calculate the accretion luminosity of each protostar:

$$L_{\rm acc} = \frac{GM\dot{M}}{R_\star}, \tag{3.7}$$

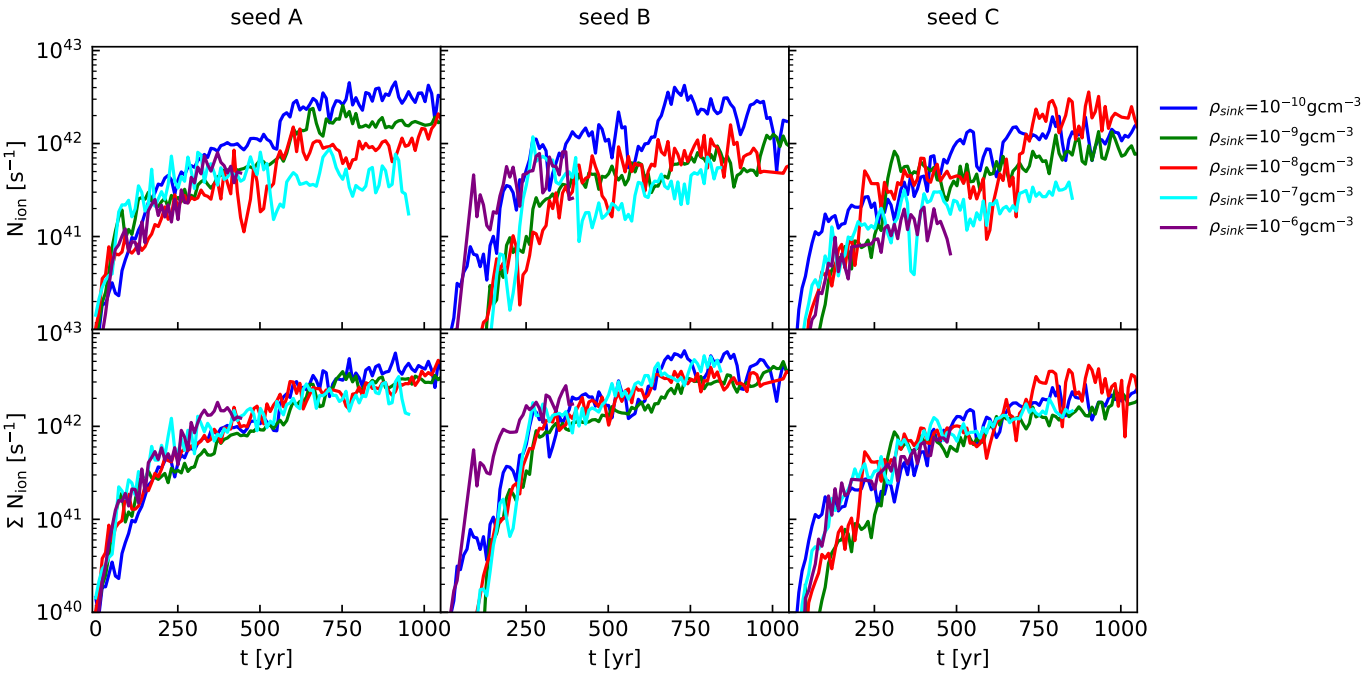

Figure 3.10. Ionising photons per second generated by accretion onto the most massive sink in the system (top) and for all sinks combined (bottom).

where M and $\dot{M}$ are the mass of, and accretion rate onto the protostar, respectively. We take $R_\star$ from the mass-radius relationship given in Hosokawa & Omukai (2009) as

$$R = 26 R_\odot \left(\frac{M}{M_\odot}\right)^{0.27} \left(\frac{\dot{M}}{10^{-3} M_\odot \mathrm{yr}^{-1}}\right)^{0.41}. \tag{3.8}$$

The effective temperature $T_{\rm eff}$ of the protostar can be estimated by equating the accretion luminosity to the total power radiated from a black body via the Stefan–Boltzmann's law:

$$\frac{L_{\rm acc}}{4\pi R_\star^2} = \sigma T_{\rm eff}^4, \tag{3.9}$$

where σ is the Stefan–Boltzmann constant. Using $T_{\rm eff}$, the total ionising energy per second can be estimated by integrating the Plank function for frequencies higher than the Lyman limit (3.28×10^{15} Hz). The number of ionising photons emitted per second then follows as:

$$\dot{N}_{\rm ion} = 4\pi \int_{\rm UV} \frac{B_v(T) 4\pi R_\star^2}{hv} dv, \tag{3.10}$$

where $B_v(T)$ is the Plank function, h is Plank's constant and v is the frequency of the the photons. The number of ionising photons per second are shown in Figure 3.10. The top panel shows that

the lower mass stars formed in higher resolution runs produce less ionising accretion radiation as a result of the fragmentation-induced starvation. The bottom panel shows that the total accretion ionising radiation from all stars in the system is unaffected by the resolution used. This can be explained by substituting equations 3.7 and 3.8 into 3.9 to obtain

$$T \propto \frac{M^{0.0475}}{\dot{M}^{0.575}}, \tag{3.11}$$

which shows that for a given mass, higher temperatures are obtained from lower accretion rates due to a smaller radius. This allows the low mass stars in the higher resolution runs to boost their ionising radiation output compared to sinks of the same mass in mass in lower resolution runs. This combined with the greater number of sinks produced in higher resolution runs explains how the total ionising radiation is independent of the resolution used and subsequent fragmentation-induced starvation.

3.5 Discussion

To the best of our knowledge, the set of simulations presented here is the first systematic study of the impact of varying the sink creation density (and hence the maximum resolution) on the formation of Pop III stars. It is also unusual in that it resolves the collapse up to a very high maximum density ($\rho \sim 10^{-6}\,\mathrm{g\,cm^{-3}}$ in our highest resolution run) while also following the evolution of the system for hundreds of years after the onset of star formation. Although many previous studies have run for comparable or longer times, they have typically done so with much lower resolution and a far smaller sink creation density (see e.g. the overview of previous simulations in Susa, 2019). Conversely, previous studies that have achieved comparable or higher resolution have typically either halted once the first protostar forms (e.g. Yoshida et al., 2008) or have been able to run for only a few years after the onset of star formation (e.g. Greif et al. 2012). The one previous study that we are aware of that combines a similar resolution with a duration of ~ 100 yr is the nested grid simulation of Machida & Nakamura (2015), although this has the disadvantage of only reaching the highest resolution in a small (~ 10 AU) central region in the calculation.

Our resolution study clearly demonstrates that the number of fragments forming within a given time systematically increases as the simulations achieve higher maximum resolution. Following the collapse to higher densities allows us to capture gravitational instability and fragmentation on ever smaller scales, owing to the decrease in λ_{J} with increasing density over the whole range of densities examined here. We have shown that the degree of fragmentation at the highest resolutions is not caused by our choice of α, as we recover qualitatively similar results regardless of whether $\alpha = 0.05$ or $\alpha = 0.25$.

Despite increased fragmentation, the total mass in stars is independent of resolution, consistent with the idea that this is determined primarily by the inflow of gas to the star-forming region, rather than the dynamics within this region. The increase in fragmentation we see at higher resolution therefore shifts the system from containing a few high mass stars at low resolutions to having many stars with lower masses in high resolution runs. The number of sinks formed did not converge, despite the fact that at the highest densities, the gas is optically thick and unable to cool radiatively. H_2 collisional dissociation enables the gas to dissipate thermal energy and remain approximately isothermal, allowing it to continue to fragment. This suggests that the degree of fragmentation will continue to increase with resolution until H_2 is fully dissociated at densities $\rho \sim 10^{-4}$ g cm^{-3}. Since most Pop III studies have used sink particle creation densities lower than the maximum tested here (e.g. Greif et al. 2011b; Smith et al. 2011; Clark et al. 2011a; Susa et al. 2014; Stacy et al. 2016; Wollenberg et al. 2019; Sharda et al. 2020), we expect that the IMFs produced by these studies have underestimated the number of stars formed and overestimated the mass of the stars.

The uncertainty in the IMF also affects the amount of ionising radiation produced by the system. An IMF dominated by high mass stars will output significantly more ionising photons than an IMF dominated by low mass stars. Once Pop III stars start emitting UV radiation, it can drastically affect the star-forming environment. Photons with energies above the Lyman limit ionise the neutral hydrogen around the star to form an H II region known as a Strömgren sphere (Strömgren 1939; McCullough 2000). Lower energy UV photons in the Lyman-Werner (LW) band escape the H II region and are able to excite and subsequently dissociate H_2, the main coolant in primordial star formation. Although it is currently unclear when and how effectively both forms of radiation escape from the immediate vicinity of the massive Pop III stars (Jaura et al., 2021), a number of simulations have outlined the effects that it can have on the gas within Pop III star-forming minihalos. For example, simulations by Stacy et al. (2012) show that ionisation of neutral hydrogen and photo-dissociation of H_2 by LW radiation causes the accretion rate onto surrounding protostars to reduce by an order of magnitude by the time the central star reaches 20 $M_\odot$. The ionising output of the first stars can also effect the next generation of stars. For instance, Hirano et al. (2015) showed that stars forming in the radiation field of the first generation of stars have stunted accretion rates and masses, which in turn lowers their output of ionising radiation (see also e.g. Haiman et al. 1997; Omukai & Palla 2003; Reed et al. 2005).

Complicating the picture here is the influence of the change in the accretion rates that occurs as we change the resolution. At higher resolution, we form more fragments and hence fragmentation-induced starvation of the most massive protostars becomes increasingly pronounced, as illustrated in Figure 3.9. Protostars with accretion rates $\sim 10^{-2}\ \mathrm{M_\odot\ yr^{-1}}$ or higher will be highly inflated, with large radii and low photospheric temperatures (see e.g. Omukai & Palla, 2003; Hirano et al.,

2014), and will only approach the standard zero-age main sequence once their accretion rates drop below this value. Protostars formed in simulations with low $\rho_{\rm sink}$ will therefore reach the main sequence more slowly than they should, delaying the time at which they become efficient emitters of ionising photons.[‡] In practice, Figure 3.9 suggests that this effect is less important than the substantial change in the IMF that we see with increasing resolution, and that the overall impact of increased resolution is to delay the time at which photoionisation feedback becomes important.

Figure 3.7 shows the cumulative number of mergers as a function of time for all $\rho_{\rm sink}$. Generally the number of mergers increases with the maximum resolution, which is to be expected as more sink particles form. However, despite the increase in $N_{\rm sink}$ from 10^{-7} to 10^{-6}g cm^{-3}, the number of mergers appears to converge. This coincides with the resolution where sink particle ejections are first seen in our simulations. We speculate that the merging behaviour converges as a consequence of the loss of sinks from the system via ejections.

Finally, our simulations demonstrate that many low mass stars will be ejected from a Pop III star-forming minihalo as it evolves, with a substantial fraction having masses that allow them to still be alive today. While accretion of metals from interstellar objects (ISOs) may disguise low mass ejectors as Pop II stars (Tanikawa et al., 2018), most studies indicate that a stellar wind and radiation can blow away interstellar particles before reaching the stellar surface (Tanaka et al. 2017; Johnson & Khochfar 2011). This would leave these low mass Pop III ejectors as pristine, metal free stars. As low-mass stars below $\sim 0.8\,{\rm M}_{\odot}$ will have survived until the present days (Kippenhahn et al., 2012), these objects should be directly detectable in current and future stellar archeological surveys (see e.g. Beers & Christlieb, 2005; Frebel & Norris, 2015; Starkenburg et al., 2017). Even non-detections allow us to constrain the low-mass end of the Pop III IMF. For example, Hartwig et al. (2015c) and Magg et al. (2019) computed the expected numbers of low-mass Pop III stars in the Galactic halo based on semi-analytic models of the assembly history of the Milky Way, and estimated the minimum sample size needed to exclude the existence of genuine low-mass Pop III stars in our Galaxy. For a similar discussion, see also Salvadori et al. (2007, 2010) and Tumlinson (2006, 2010). This approach can be extended to include the satellite galaxies to the Milky Way (e.g. Magg et al., 2018).

Although protostellar ejections have been found to occur in many previous simulations of Pop III star formation, Greif et al. (2012) raised the concern that this may be a numerical artifact, a consequence of not allowing sink particles to merge. We have introduced sink mergers into AREPO to remedy this situation and have proved that ejections indeed continue to occur when merging is enabled, suggesting that this is a real physical effect and not an artifact.

[‡]In Appendix 3.4.2, we estimate the total ionising luminosity generated by accretion onto the protostars and show that this is negligible compared to the ionising luminosity of even a single massive main sequence star.

3.6 Caveats

Our initial conditions represent idealised Bonnor-Ebert sphere density profiles in randomised turbulent velocity fields, in the absence of a live dark matter gravitational potential. Although we expect the influence of the dark matter halo to be small on the scales we simulate, it is nevertheless the case that a more realistic approach would be to isolate a single dark matter halo and perform star formation simulations within it. However, this is not necessary to assess the effects of resolution on the fragmentation behaviour of primordial gas, as is the focus here.

A more important limitation of our current study (albeit one shared by most previous work on Pop III star formation) is the fact that we have examined only non-magnetised collapses. Weak magnetic seed fields are believed to have existed in the early Universe, which were amplified by the small-scale turbulent dynamo, resulting in a magnetic field with a $k^{3/2}$ power spectrum (Sur et al., 2010; Schleicher et al., 2010; Schober et al., 2015). Present day star formation simulations show that uniform magnetic fields support discs against fragmentation (e.g. Hennebelle & Fromang 2008; Seifried et al. 2011; Bürzle et al. 2011b) and evidence is starting to accumulate that the small-scale primordial fields can also reduce fragmentation (Sharda et al., 2020). Magnetic flux freezing allows the field to become stronger as the maximum density of the gas is increased, which may counteract the increase in gravitational instability as the maximum resolution is increased. The ability of magnetic fields to achieve numerical convergence in N_{sink} and prevent increasing fragmentation-induced starvation will be assessed Chapter 5.

Another caveat is the fact that in our treatment of sink particle mergers, we have assumed that the merging cross-section is fixed, and set by the accretion radius of the sink particle, which in turn is set by the Jeans length at the sink formation density. In reality, the merging scale will depend on the physical size of the protostar and likely increases as the protostar gains mass.

Finally, these simulations only included accretion luminosity feedback and not the radiative feedback produced by the stars once they reach the main sequence. Although stellar luminosity has been shown to prevent accretion onto the host star and to suppress star formation in the surrounding cloud (Stacy et al., 2016), its absence from our simulations is unimportant, since the protostars formed in our simulations are still in the early, adiabatic phase of their evolution and will not emit significant radiation.

3.7 Conclusions

In a Population III setting, the effect of varying the sink particle creation density was investigated. A turbulent cloud collapse resulting in periodic bursts of star formation was repeated for sink

creation densities ρ_{sink} spanning the range 10^{-10}-10^{-6}g cm^{-3}. As ρ_{sink} increased, larger numbers of sinks were formed without converging within the range tested. The total mass in sinks was independent of the sink parameters used, resulting in an IMF that shifts towards lower mass stars with higher sink creation density. We also find that a significant number of low mass protostars get ejected from the halo center by stellar dynamical processes. Combining the 6 iterations of the highest resolution case resulted in an ejection fraction of 0.21 for low mass stars capable of surviving to this day (0.075 - 0.8 $M_{\odot}$), and 0.42 for brown dwarf stars. Our results suggest that the number of sinks will continue to grow with increasing ρ_{sink}, until H_2 is fully dissociated and the collapse becomes almost adiabatic at 10^{-4}g cm^{-3}. More sinks owing to higher ρ_{sink} also caused increased fragmentation-induced starvation of the most massive sink in the system, which will lower the final stellar mass and subsequent ionising radiation output of the star. Since Population III studies are yet to reach densities of 10^{-4}g cm^{-3}, these results show that the primordial IMF has thus far overestimated the mass of stars and underestimated the number of stars forming per halo. We predict a significant number of free-floating genuine low-mass Pop III stars in the Milky Way and its satellites, which could be the target of current and future archaeological surveys.

Chapter 4

Testing MHD methods with Arepo

In chapter 3 we have shown that for a primordial chemistry set-up, increased resolution allows fragmentation on smaller Jeans scales all the way up to the formation of the protostar. In chapter 5 we go on to assess whether primordial magnetic fields can provide support against this fragmentation. In this chapter, we test different approaches to simulating magnetic fluids to find the most stable method. We begin by comparing two commonly used techniques of cleaning divergence errors in the field, then assess the use of a variable time step to clean the divergence errors, before exploring how resolution changes the dynamo amplification process on an unstructured Voronoi tessellation mesh.

4.0.1 Divergence error cleaning

It is common for $\nabla \cdot \vec{B}$ errors to arise in numerical simulations. This results in non-physical results, such as plasma transport orthogonal to the magnetic field lines. Constrained transport methods have been developed to restrict $\nabla \cdot \vec{B}$ to 0, but these are restricted to codes with structured grids, unlike the voronoi mesh of Arepo.

One of the most popular methods of dealing with $\nabla \cdot \vec{B}$ errors is the Powell et al. (1999) approach, which adds additional source terms into the momentum equation, induction equation and energy equation, to advect $\nabla \cdot \vec{B}$. A more sophisticated method is the Dedner et al. (2002) approach, which adds a scalar-field and a set of source terms to advect local divergence errors away but also dampen them. As both techniques are currently implemented into AREPO, we compare Powell and Dedner cleaning schemes by performing a Pop III collapse simulation with the same initial conditions and chemistry as Section 3.3, with an additional uniform magnetic field of strength 10^{-9} G and resolution criteria of 128 cells per Jeans length. The properties of the field as a function of density for both cleaning methods are shown in Figure 4.1.

The Powell scheme gives increased dynamo amplification compared to Dedner cleaning, however the divergence error is of the order of 10% of the field strength, compared to the 1% error produced with Dedner cleaning. For this reason, the Dedner scheme was used for the remainder of the simulations. We note that this gives a conservative estimate of the field amplification.

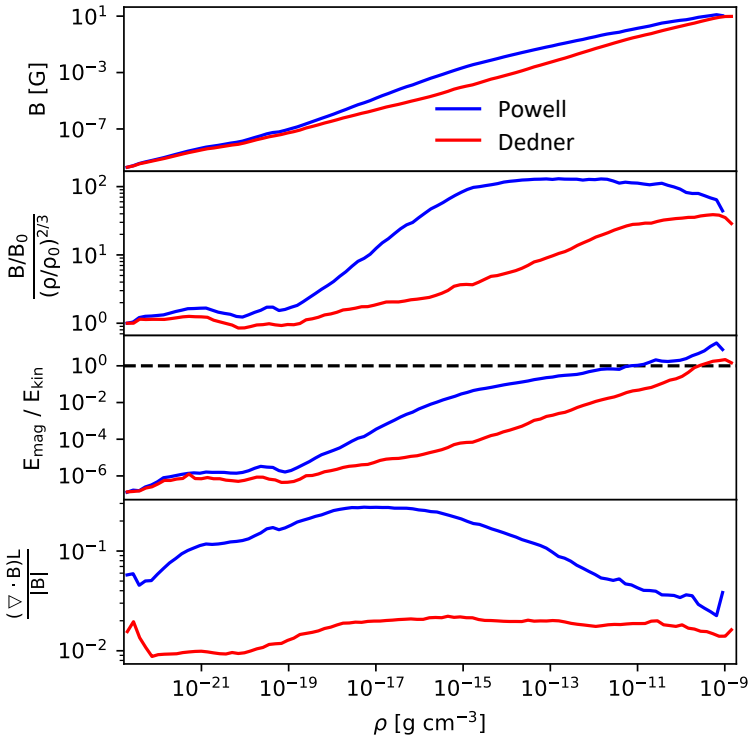

Figure 4.1. Comparison of the dynamo action when using Powell terms versus Dedner terms for cleaning $\nabla \cdot \vec{B}$ errors. From top to bottom, the panels show magnetic field strength, field strength normalised by $\rho^{2/3}$ to show dynamo action, the ratio of magnetic to kinetic energy and the ratio of divergent field to the total field i.e. the $\nabla \cdot \vec{B}$ error.

4.0.2 Variable Dedner cleaning speed

Magnetic fields drastically increase the computational resources required for simulations. For this reason, we consider using a variable cleaning speed for the $\nabla \cdot \vec{B}$ cleaning (e.g. Tricco et al. 2016). We test the variable cleaning speed by reproducing a present day star formation simulation as performed by Hennebelle & Fromang (2008) and Bürzle et al. (2011b). A spherical cloud of radius 0.016 pc with uniform density 5×10^{18} g cm^{-3} and solid body rotation defined by its ratio of rotational to gravitational energy β=0.045 was placed in an ISM 100 times less dense. The simulation box scale was 0.064 pc with periodic boundary conditions. A linear magnetic

field was threaded through the cloud, parallel to the axis of rotation. The field strength was defined by the systems mass-to-flux over critical mass-to-flux ratio $\mu = 5$, corresponding to 10.67 G. This produces a highly magnetised supercritical cloud. A baratropic equation of state $C_s^2 = (C_s^0)^2(1 + (\frac{\rho}{\rho_c})^{4/3})^{1/2}$, where $\rho_c = 10^{-13}$ g cm^{-3} and $C_s^0 = 0.2$ km s^{-1}, was used to mimic opaque, nearly adiabatic gas at high densities. We ran the simulation twice, using a global cleaning speed followed by a variable cleaning speed. The outcome seen in Figure 4.2. An initial outflow was produced in both simulations, similarly to Bürzle et al. (2011b). However, when using the variable cleaning speed the outflow evolved into a non-symmetric, non-physical explosion in the central region.

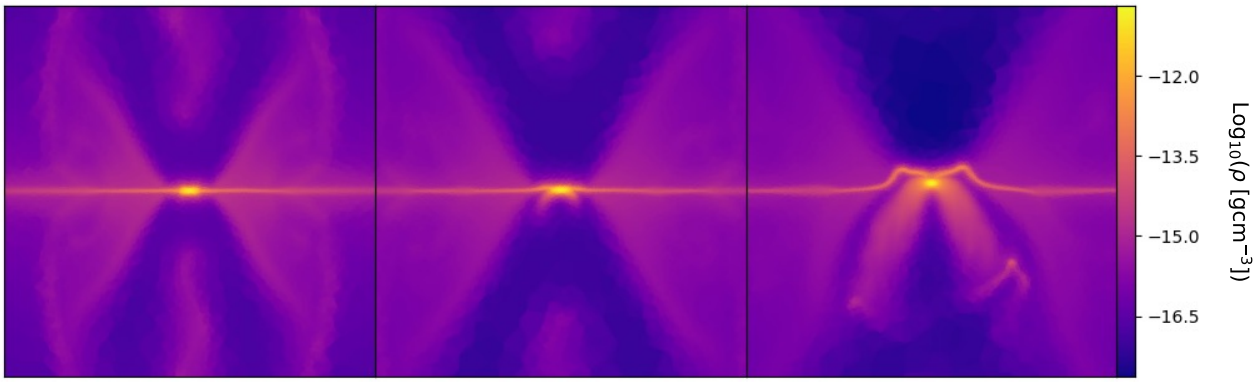

Figure 4.2. Column-weighted density projections of a magnetised cloud collapse resulting in the launch of a jet. The simulations ran with a variable cleaning speed. Panels correspond to 1.074, 1.089 and 1.103 free-fall times.

To investigate this result, we set up a simulation inspired by Tricco & Price (2012). We placed a small 'blob' containing a divergent magnetic field within a box of non-divergent field. For our first test, the blob was placed in a medium of constant density with uniform velocity. Figure 4.3 shows that both a global and varied cleaning speed converge to the same maximum and average error in the medium of constant density, but that varying the cleaning speed achieves the final value faster. A second test was performed where the blob was placed in a static medium with a density step to a region where the density was enhanced by a factor of 2. Figure 4.4 shows that in the presence of a density enhancement, cleaning is not able to bring the error down to values below its initial value, but it does prevent it from growing indefinitely if a global cleaning speed is used. In contrast to the uniform density and velocity test, the variable cleaning speed leads to a run-away growth of the divergence error. In light of these results, the global cleaning speed was used for the remainder of the project.

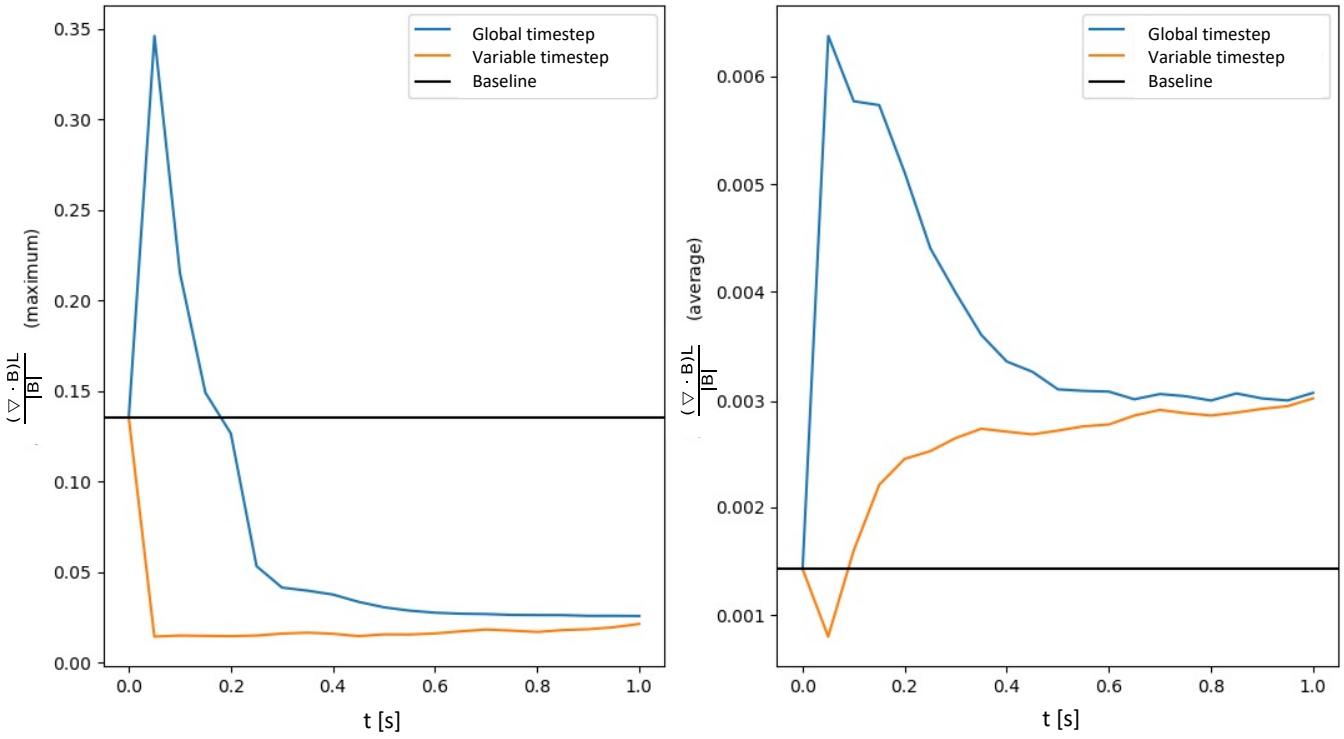

Figure 4.3. Performances of the Dedner et al. (2002) divergence cleaning with global and varied cleaning speeds, for a ball of divergent magnetic field in a medium of constant density, with uniform velocity. The black line shows the initial values of the divergent field.

4.0.3 Dynamo amplification on an unstructured mesh

While the effects of refinement criteria on the amplification of magnetic fields were explored in Federrath et al. (2011a) on a uniform grid, there is currently no equivalent literature for the unstructured voronoi tessellation that forms the mesh of AREPO simulations. We have run a series of idealised Bonner Ebert sphere collapses with the same initial conditions as Section 3.3, with an additional uniform magnetic field at strength 10^{-9} G. We repeat the collapse, increasing the Jeans refinement criteria from 16 to 128 cells per Jeans length. The results are shown in Figure 4.5.

The second panel shows the field strength normalised by $\rho^{2/3}$ i.e. the amplification expected from flux freezing. The resulting values show the pure dynamo amplification of the field. Clearly higher refinement criteria gives greater amplification of the field even for an unstructured mesh.

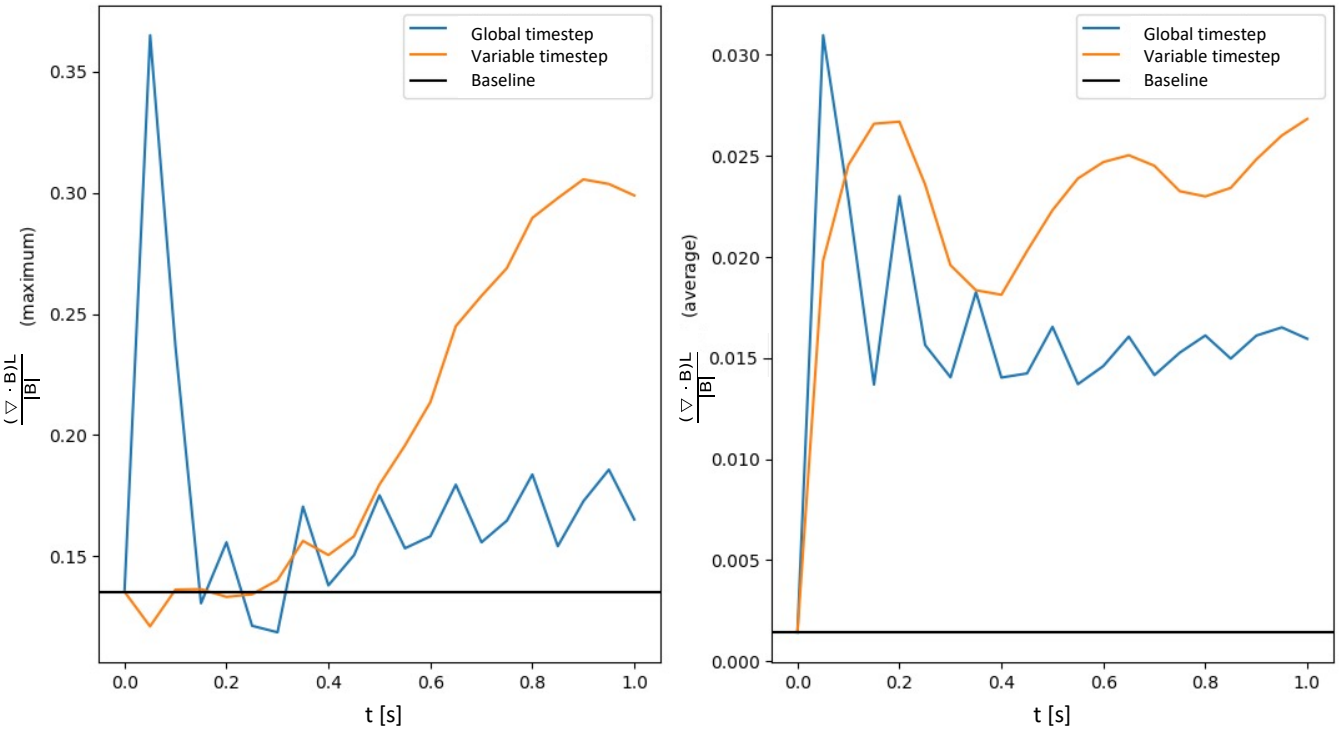

Figure 4.4. Performances of the Dedner et al. (2002) divergence cleaning with global and varied cleaning speeds, for a ball of divergent magnetic field in an initially static medium in the presence of a X2 density jump. The black line shows the initial values of the divergent field.

4.1 Conclusion

The results of these MHD tests will govern the methods used in the magnetised resolution study in Section 5. We have shown that using Dedner cleaning terms yield lower $\nabla \cdot \vec{B}$ divergence errors than the Powell scheme. Using a variable cleaning speed to clean the divergence errors leads to non-physical results such as exploding stars, which we have attributed to a build up of divergent field. Finally we have shown that increasing the refinement criteria does lead to increased amplification of the magnetic field during a turbulent collapse on an unstructured mesh. Unlike previous studies on uniform grid codes, we find that dynamo amplification occurs for refinement criteria as low as 16 cells per Jeans length. As simulations can not achieve infinite resolution, the safest way to handle the amplification of magnetic fields is to bypass the amplification phase and introduce a fully saturated field later in the collapse (see Chapter 5).

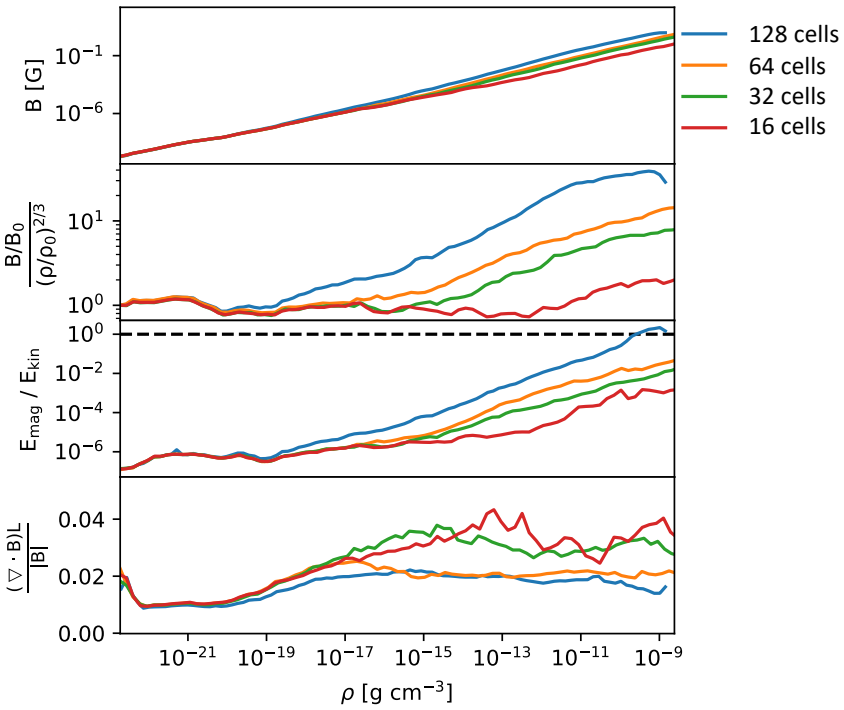

Figure 4.5. Comparison of magnetic field properties when varying the Jeans refinement criteria from 16-128 cells per Jeans length. From top to bottom, the panels show magnetic field strength, field strength normalised by $\rho^{2/3}$ to show dynamo amplification, ratio of magnetic to kinetic energy and the ratio of divergent field to total field strength i.e. the $\nabla \cdot \vec{B}$ error.

Chapter 5

Magnetised resolution study

While magnetic fields have been shown to suppress fragmentation in present day star formation, it is unclear if they will have the same impact on Pop III star formation due to differences in the field structure. This investigation attempts to bypass the resolution-dependent amplification process described in Section 4.0.3 by introducing a saturated field after an initial non-magnetized phase of collapse. We zoom-in on the most central region for the magnetised phase and set the magnetic field strength to the theoretical maximum by choosing the dynamo saturation energy to be at equipartition with the velocity field i.e. $E_{mag}/E_{kinetic}$ =1. In (Prole et al., 2022a) (hereafter LP22), we concluded that in the purely hydrodynamic case, the degree of disc fragmentation would not converge until the gas becomes adiabatic at 10^{-4}gcm^{-3}, shifting the IMF to smaller mass stars as the maximum density increases. This chapter covers work originally presented in Prole et al. (2022b), which tests if realistic primordial magnetic fields can provide the necessary support against fragmentation to converge the IMF before the formation of the adiabatic core. Due to the increased computing resources required for MHD simulations, the maximum density of the resolution test was chosen to catch all of the relevant chemical processes, the last of which is the dissociation of H_2 molecules at $\sim 10^{-8}$gcm^{-3}.

5.1 Simulations

5.1.1 non-magnetised collapse

Initially, we assume that the magnetic field is too weak to affect the collapse significantly (see Section 5.4) and run a pure hydrodynamic collapse of primordial gas. The initial conditions consist of a Bonner-Ebert sphere (Ebert, 1955; Bonnor, 1956) categorised by central density

Table 5.1. For each simulation parametrised by its seed field and sink creation density, we give the rms magnetic field strength for the MHD zoom-in simulations.

Seed	$\rho_{\rm sink}$ [gcm^{-3}]	$B_{\rm rms}$ [mG]
A	10^{-10}	7.42
A	10^{-9}	7.40
A	10^{-8}	7.48
B	10^{-10}	11.74
B	10^{-9}	11.68
B	10^{-8}	11.78
C	10^{-10}	6.94
C	10^{-9}	6.90
C	10^{-8}	6.94

ρ_c=2×10^{-20} g cm^{-3} and radius R_{BE}=1.87 pc, placed in a box of side length 4R_{BE} and temperature 200K. The stable Bonner-Ebert density profile was enhanced by a factor of 2 to promote collapse, such that the new central density was 4×10^{-20} g cm^{-3}. The initial abundances of H_2, H^+, D^+ and HD are x_{H_2}=10^{-3}, x_{H^+}=10^{-7}, x_{D^+}=2.6×10^{-12} and x_{HD}=3×10^{-7}. A random velocity field was imposed on the box, generated from the Burgers turbulent power spectrum $\propto k^{-2}$ (Burgers, 1948). The rms velocity was scaled to give a ratio of kinetic to gravitational energy α=0.05. The simulations were performed with a refinement criterion that ensured that the Jeans length was always resolved by at least 32 cells, as required by the findings of Federrath et al. (2011a). The simulations were repeated for 3 different velocity fields, which we henceforth refer to as seeds A, B and C. We repeat the simulations increasing the sink particle creation densities from 10^{-10} to 10^{-8} g cm^{-3} to make sure the findings aren't resolution dependent. We use the sink particle parameters from Table 5.1.

5.1.2 Magnetised collapse

We allow an initial non-magnetised collapse to run until the central density reaches ∼10^{-13} g cm^{-3}, before cropping the central region and applying a saturated magnetic field. At this point, the smallest cells are of scale $\Delta x \sim 14.5$AU. The cropped box size is chosen by calculating the radius which corresponds to a free-fall time of 10^4 yr, ensuring that further collapse of the order of 1000 yr can be safely followed within the new box size. The new box size was calculated to be 0.032pc and has periodic boundary conditions. Although the use of periodic boundary conditions prohibits angular momentum from the dense core to be transferred outside of the simulation box, potentially affecting the ability of the disc to fragment, the timescales involved with these processes mean that this is not a problem for our set-up. Angular momentum is transferred by torsional Alfvén waves travelling at the Alfvén velocity $v_{\rm A} = B/\sqrt{4\pi\rho}$. At our initial field strength

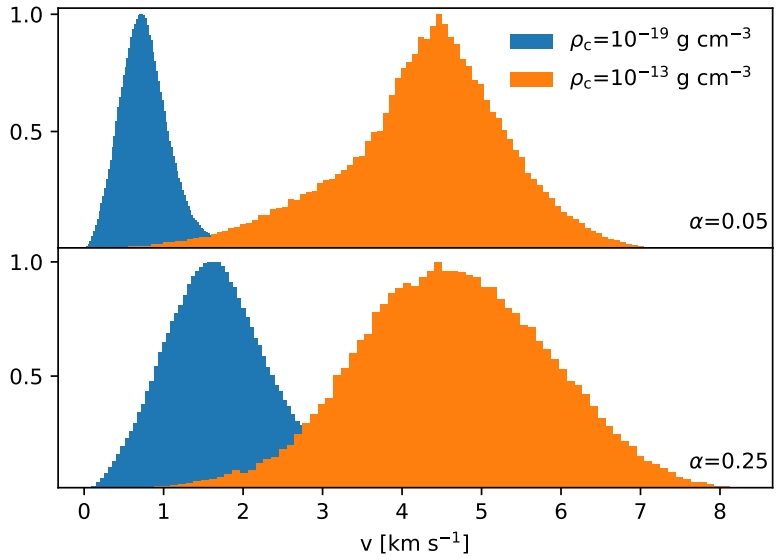

Figure 5.1. Normalised, mass weighted histograms of the initial velocity field and the field within the central 0.032pc when the central density reaches $\sim 10^{-13}$gcm^{-3}, for the α=0.25 and α=0.05 runs of Chapter 3.

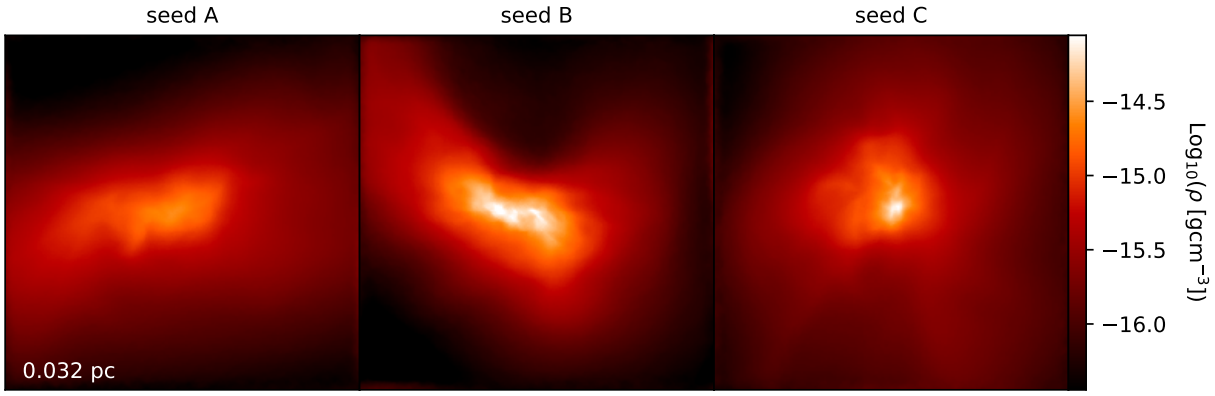

Figure 5.2. The inner 0.032 pc of the non-magnetised collapse, once the central density has reached $\sim 10^{-13}$gcm^{-3}, projected onto 500^3 cubes and flattened along the y axis. These serve as the initial conditions for the magnetised stage of the collapse.

of $\sim 10^{-2}$ G at $\sim 10^{-13}$ g cm^{-3}, it would take $\sim 2 \times 10^5$ yr to transport the angular momentum to the edge of the simulation box, roughly two orders of magnitude longer than the simulations are allowed to run. As we will see in Section 5.3, by the end of the simulation the field strength at 10^{-8} g cm^{-3} is $\sim 10^2$ G. At this Alfvén velocity, the travel time reduces to ~ 6000 yr. We

therefore do not expect significant angular momentum to reach the boundaries from the center during the simulated period. As such, the small-scale magnetic braking in discs is unaffected by our choice of boundary conditions or the size of our computational domain. The cropped boxes are shown in Figure 5.2.

To generate the saturated magnetic fields, we used the Kazantsev $P_k \propto k^{3/2}$ power spectrum with 200 modes (and 200 negative modes), resulting in a cube with spatial resolution $\Delta x \sim 17$AU, such that the field is resolved in the central region of the collapse. The imposed magnetic field is scaled to the maximum strength by assuming that the magnetic energy has saturated with the velocity field. While it might be expected that saturated magnetic field strength depends on the initial velocity field strength, Figure 5.1 shows the velocity fields from the α=0.25 and α=0.05 runs in LP22 within the central 0.032pc, when the central density reaches 10^{-13} g cm^{-3}. The strength of the central velocity field does not depend on the initial field strength, hence the saturated magnetic field strength does not depend on the initial velocity field. The method of generating a 3D field from the 1D power spectrum is described in Section 2.2. The field is then interpolated onto the AREPO cell coordinates and rescaled to give the desired rms strength. The rms strength is chosen so that the magnetic field energy reaches equipartition with the velocity field. Magnetic energy density is given by $B^2/8\pi$, so we scale the rms magnetic field strength as $B_{\rm rms} = \sqrt{8\pi\epsilon_{\rm KE}}$, where $\epsilon_{\rm KE}$ is the volumetric kinetic energy density.

We repeat the simulations with no magnetic fields as a control case. For seed A, we repeat the simulation with a uniform field threaded through the z-axis, with the same rms field strength as the k$^{3/2}$ field i.e. B=(0,0,B$_{\rm rms}$) at all points in the simulation box, to show the effects of under resolving the field in the initial conditions. We also repeat the $\rho_{\rm sink} = 10^{-13}$ g cm^{-3} version of seed A with a less restrictive refinement criterion that requires only 16 cells per Jeans length, to compare the dynamo amplification to the 32 cells per Jeans length case. This gives a total of 22 zoom-in simulations from the initial 3 full-scale simulations. The initial conditions for the magnetised collapses are summarised in Table 5.1.

5.2 FRAGMENTATION BEHAVIOUR

For the 3 seed fields, Figures 5.3, 5.4 and 5.5 show the number of sink particles and total mass in sink particles as a function of time, for increasing sink particle creation density. For all 3 seeds, the number of sink particles is not significantly lower in the magnetised case compared to the hydrodynamic cases. There is therefore no evidence of reduced fragmentation owing to magnetic support. While the pause in sink formation seen in the top left panel of seed C could be interpreted as delayed star formation due to magnetic fields, the total mass accreted onto sink particles is unaffected by the fields. This indicates that the differences are due to the stochastic

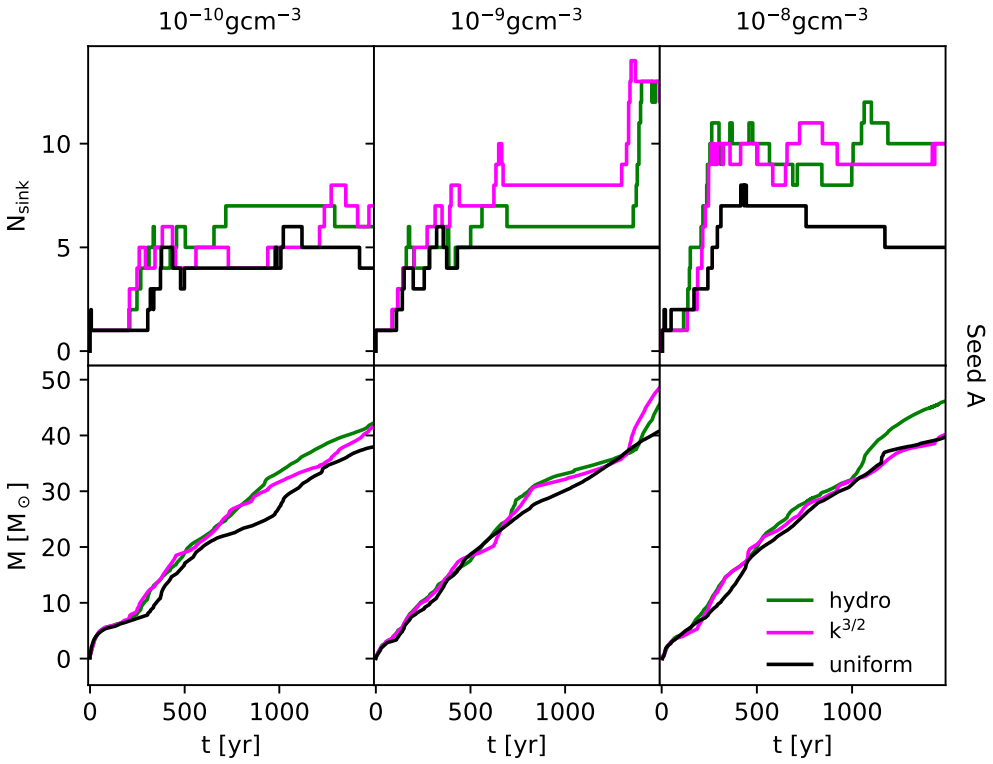

Figure 5.3. Number of sinks formed and total mass in sinks as a function of time, for initial velocity and magnetic seed field A. The sink particle creation density is indicated above the columns.

nature of the simulations. In the hydrodynamic case, increased fragmentation with increasing sink creation density occurs as described in LP22, despite the employed zoom-in method described in Section 5.1.2. The presence of magnetic fields does not change this outcome within the range of resolutions tested. The cumulative IMFs at ~ 1000 yr after sink formation are shown in Figure 5.6 and reveal no trends between the hydrodynamic and MHD runs. The systems at ~ 1000 yr are shown in Figure 5.7. While the scale and orientation of the systems are unaffected by the magnetic fields, there are some structural differences which are to be expected from stochastic N-body simulations.

When the $k^{3/2}$ field was replaced with a uniform field for velocity seed A, the system does experience decreased fragmentation as the resolution is increased. The fragmentation behaviour possibly converges with resolution in this case, although that is impossible to interpret with only 1 realisation of the fields. Decreased fragmentation in the presence of initially uniform magnetic fields has been seen in many previous present-day star formation studies (e.g. Price & Bate 2007; Machida & Doi 2013). This effect is likely due to a mixture of magnetic tension transferring angular momentum away via magnetic braking and pressure support against Jeans instabilities.

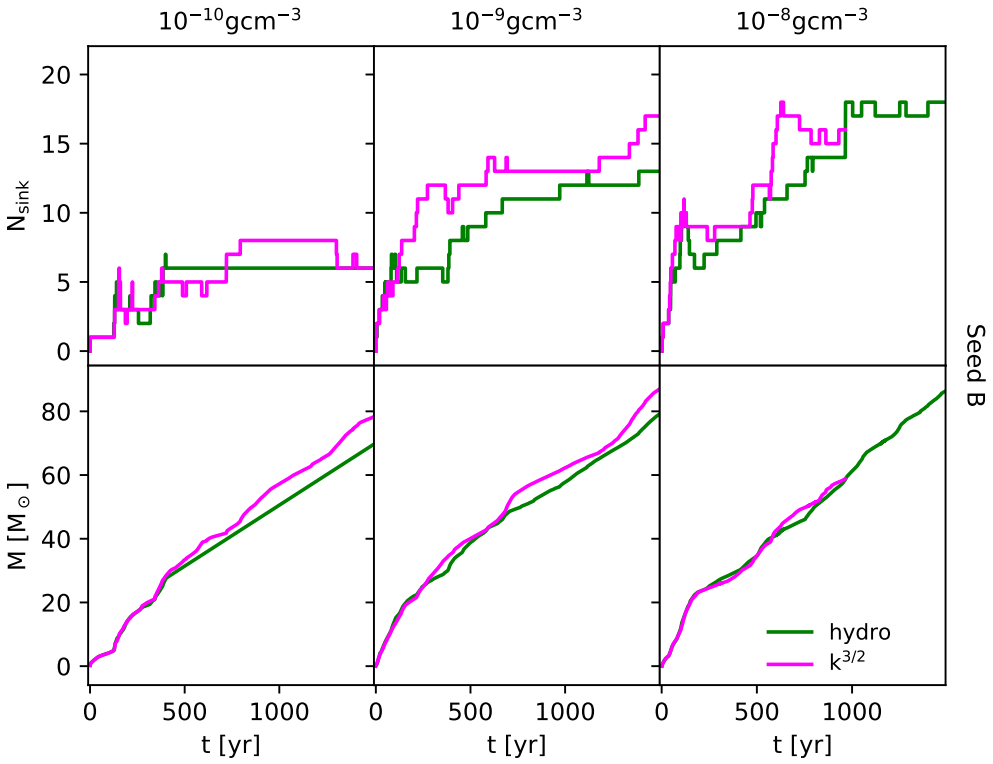

Figure 5.4. Same as Figure 5.3 but for seed field B.

The lesser effect of the field at lower resolutions is due to the gas's tendency to fragment less at lower resolutions in both the hydrodynamic and MHD scenarios.

Suppressed fragmentation by uniform fields at these scales reveals a non-obvious danger of including a tangled magnetic field in the initial conditions as has been done in previous studies (e.g. Sharda et al. 2020). For a given simulation box, only a small region collapses to form stars, so an insufficiently resolved $k^{3/2}$ magnetic field can act as a uniform field across the relevant areas in the early collapse, providing false support against fragmentation. This may not be a problem in the later collapse as the small scale turbulent dynamo should convert the field into a $k^{3/2}$ power spectrum, but the early effects of the field could significantly alter the gas flow into the star-forming region. Our high resolution $k^{3/2}$ fields were introduced across a small region of the box once relevant areas of star formation were revealed, so we are confident that the gas sees a $k^{3/2}$ field (see Section 5.4).

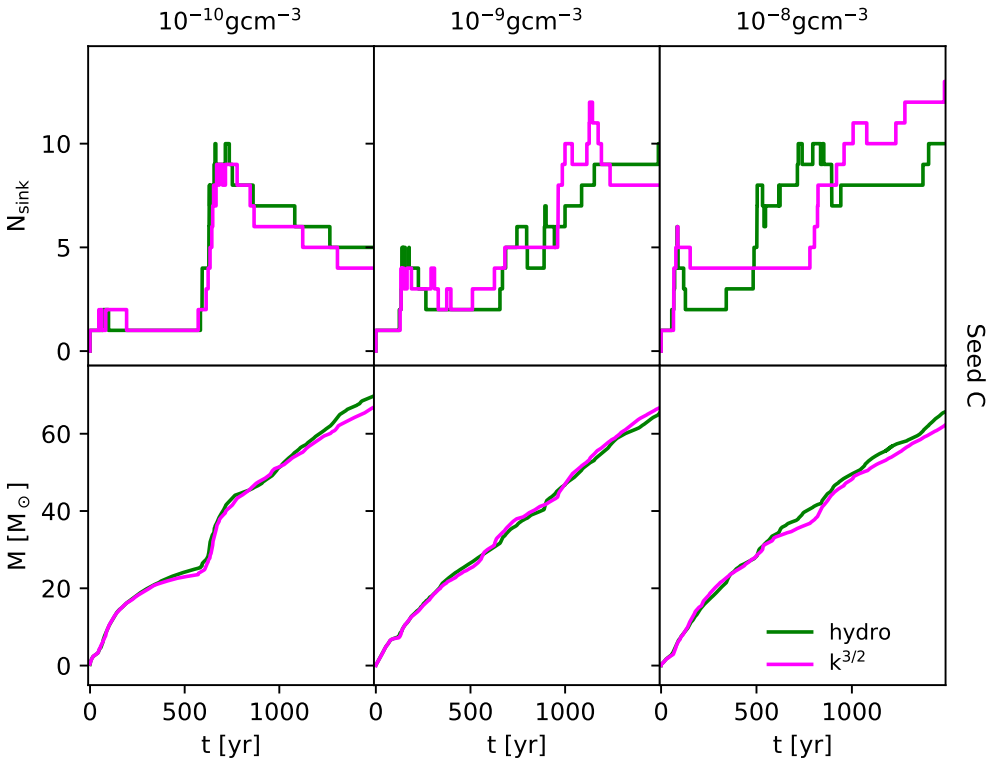

Figure 5.5. Same as Figure 5.3 but for seed field C.

5.3 Field behaviour

Figure 5.9 shows the field strength normalised by $\rho^{2/3}$, which is the amplification expected due to flux freezing alone. Any positive gradients in the resulting curve correspond to dynamo amplification. The runs with 32 cells per Jeans length do experience dynamo action while the central density increases towards the maximum density of the simulations, unlike the run with 16 cells per Jeans length. This aligns with the findings of Federrath et al. (2011a). The amplification is a factor ~ 3 in the densest regions. However, after sink particle formation the amplification rises rapidly to ~ 10 in both cases.

The field strength just before the formation of sink particles is shown for the different resolutions used in Figure 5.10. Higher resolutions allow for higher maximum densities and hence stronger maximum magnetic field strengths due to flux freezing. By normalising by $\rho^{2/3}$, it is revealed that increasing the maximum refinement level (and decreasing the gravitation softening length) only affects the dynamo amplification at the highest available densities (smallest scales), where the amplification gets progressively stronger.

Figure 5.11 shows the evolution of field quantities as a function of density, for the 10^{-8} g cm^{-3}

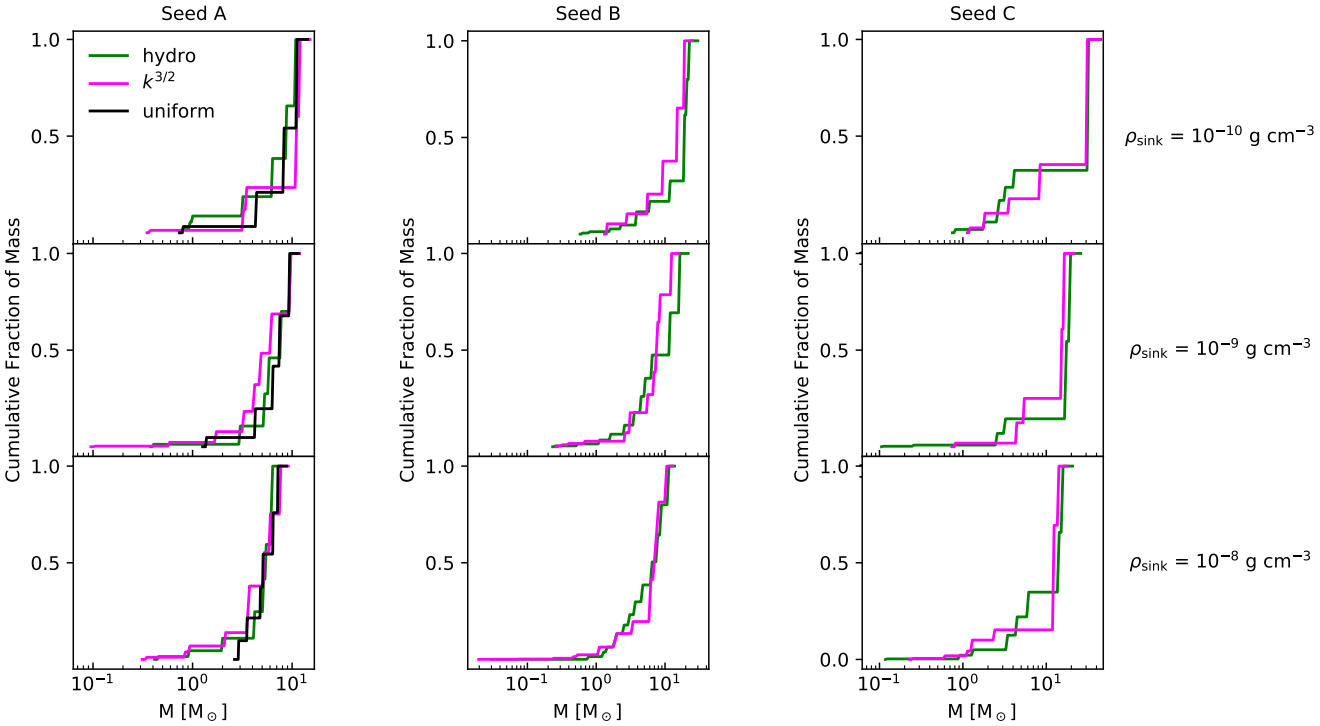

Figure 5.6. Normalised cumulative IMFs for the hydro and $k^{3/2}$ runs at $\sim$ 1000 yr after the formation of the first sink particles. The sink particle creation densities used are shown on the right side of the figure.

run. The field strength within the entire collapsing region grows until seemingly converging after 1000 yr. For our small-scale fields, we do not expect magnetic tension will play an important role. The magnetic pressure however is isotropic and in theory can support against fragmentation. The magnetic and thermal pressure are given by

$$P_{\mathrm{B}} = \frac{B^2}{8\pi}, \tag{5.1}$$

$$P_{\mathrm{gas}} = \frac{k_{\mathrm{B}}\rho T}{\mu m_p} \tag{5.2}$$

respectively, where k_{B} is Boltzmann's constant, T is the temperature, μ is the mean molecular weight and m_{p} is the mass of a proton. The magnetic pressure is significantly lower than the thermal pressure at low densities and high densities pre-sink formation, explaining why it was unable to suppress fragmentation. Amplification of the field strength leads to the magnetic and thermal pressures becoming comparable at densities of 10^{-10} g cm^{-3} and upwards by the end of

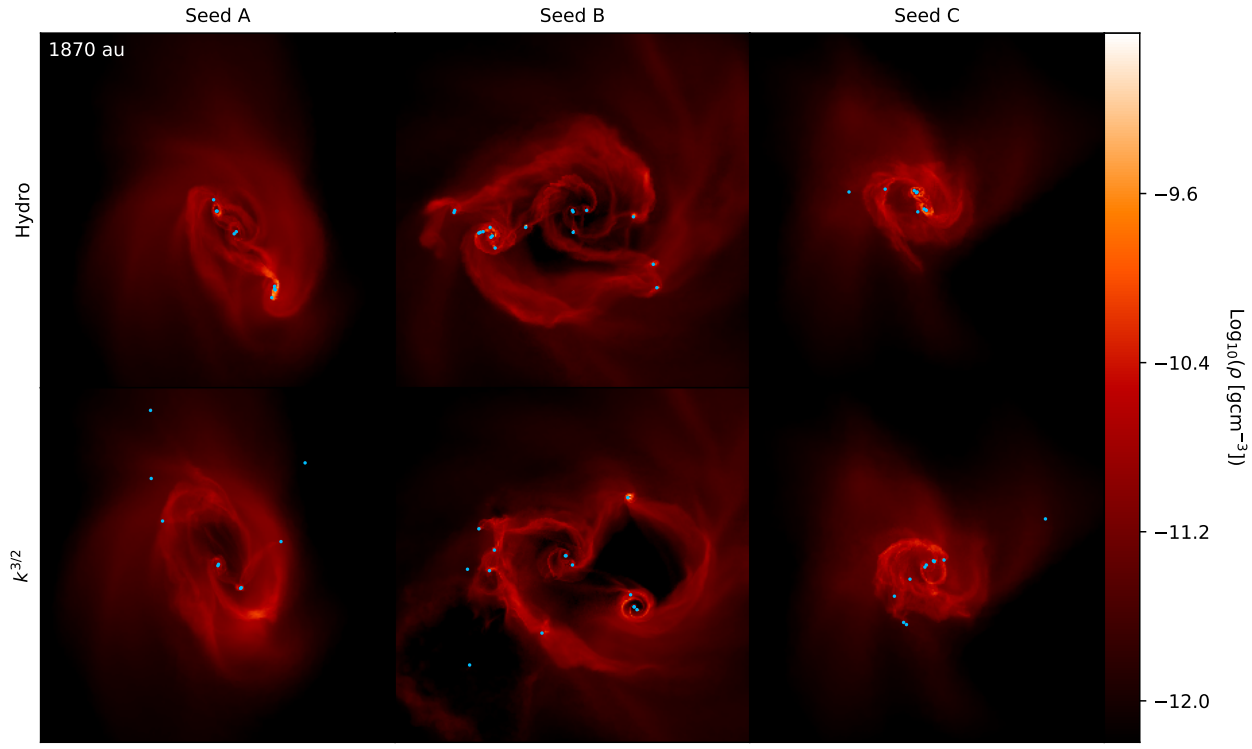

Figure 5.7. Density projections for the highest resolution ($\rho_{\mathrm{sink}} = 10^{-8}$ g cm^{-3}) runs, comparing the non-MHD (top) and $k^{3/2}$ magnetic field (bottom) scenarios. Sink particles are shown as blue dots.

the simulation. Additionally, the maximum density of the simulations was reached before magnetic pressure could grow to become the dominant term. The magnetic pressure grows at minimum as $\rho^{4/3}$ due to flux freezing, while the gas pressure has a linear dependency on density, so the gas pressure likely becomes dominated by the magnetic contribution at higher densities than this investigation has resolved. As fragmentation is expected to occur on smaller Jeans scales with increasing density, this dominant magnetic pressure may suppress fragmentation on the smallest scales between $10^{-10} - 10^{-4}$ g cm^{-3} before the adiabatic core forms. However, one-zone calculations with an added protostellar model for zero metallicity stars by Machida & Nakamura (2015) suggest a rapid increase in temperature at 10^{-6} g cm^{-3}, likely rendering the gas stable to fragmentation. This only leaves 2 orders of magnitude in density higher than our sink particle creation density where magnetic fields could suppress fragmentation.

The ratio of magnetic to kinetic energy settles at a value of ~ 0.3 in the highest density regions while the ratio of magnetic to thermal energies reaches ~ 10. This saturation value fits

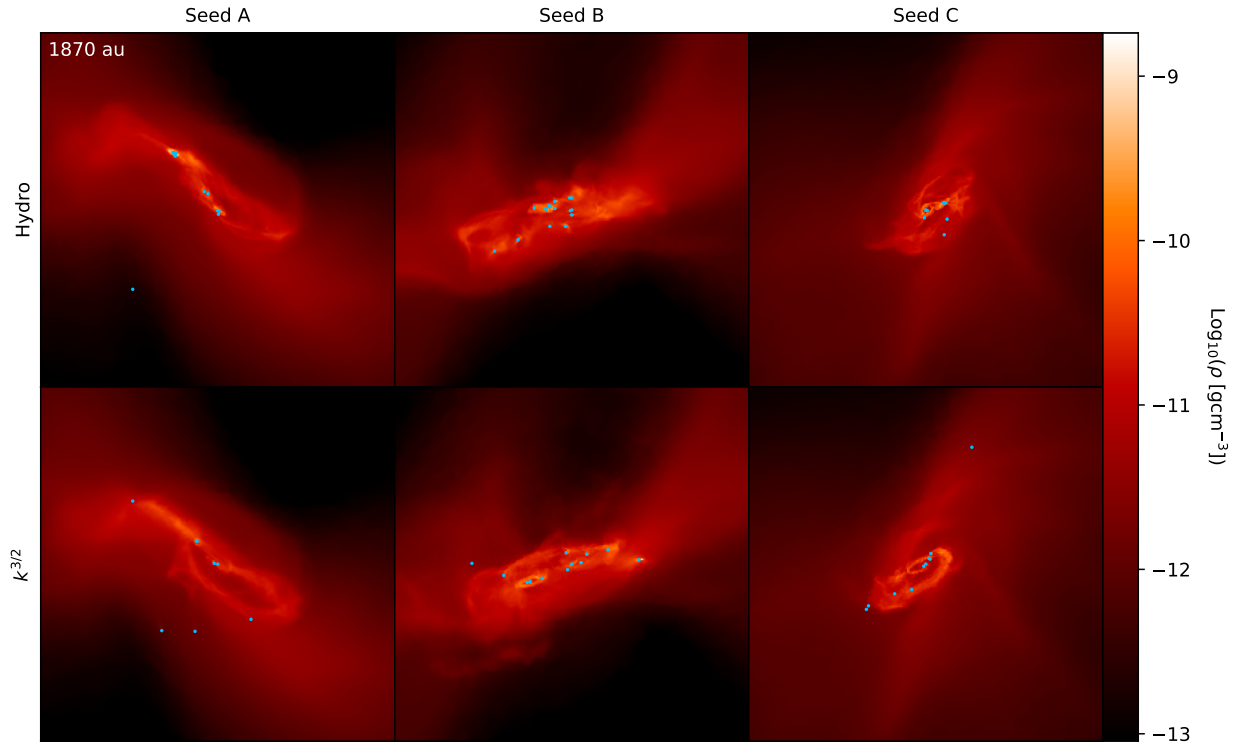

Figure 5.8. Same as Figure 5.7 but showing an edge on view to the discs.

in line with previous turbulent box studies of the small-scale turbulent dynamo (e.g. Haugen et al. 2004, Federrath et al. 2011b, Schober et al. 2015).

The evolution of the magnetic power spectrum within the central 600 AU around the most massive sink is shown in Figure 5.12. These were created by projecting the AREPO cells onto a 50^3 uniform grid, resolving scales of 12 au. The peak of the spectrum moves to smaller spatial scales after the formation of sink particles, following a $k^{3/2}$ power law down to scales of ~ 120 AU at 1000 yr after the formation of the first sink particle. The energy continues to grow on smaller scales down to the Nyquist frequency of the projection, corresponding to ~ 25 au.

Our results suggest that the inclusion of magnetic fields is unimportant in numerical simulations of Pop III star formation up to densities of 10^{-8} g cm^{-3}. For most previous Pop III studies, the resolution is too poor to capture the small-scale fragmentation that could be suppressed by magnetic fields at densities higher than explored in the simulations presented here (e.g. Greif et al. 2011b; Smith et al. 2011; Clark et al. 2011a; Susa et al. 2014; Stacy et al. 2016; Wollenberg et al. 2019; Sharda et al. 2020). This result renders the task of finding the primordial IMF through

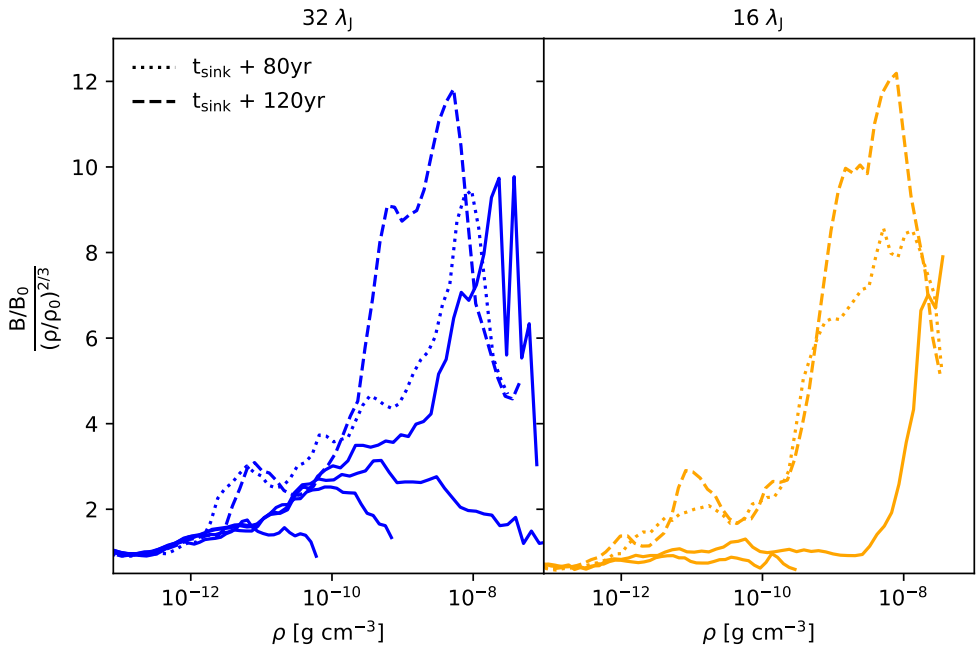

Figure 5.9. Comparison of the dynamo amplification between the 32 and 16 cells per Jeans length runs for seed field A, for the highest sink particle creation density. The field strength is normalised by $\rho^{2/3}$ i.e. the growth due to flux freezing. Any residual positive gradient is due to dynamo amplification. The solid lines show the field at different central densities leading up to and including sink particle formation, while the dotted and dashed lines show the field at 80 and 120 yr after sink formation, respectively.

numerical simulations less computationally expensive and time consuming.

5.4 Comparison with previous studies

Machida et al. (2008) produced jets in set-ups where the initial magnetic field was dominant over rotation ($\gamma_0 > \beta_0$) above a threshold magnetic field strength of 10^{-9} G at 10^{-21} g cm^{-3}. They did not report the evolution of magnetic field strengths at different central densities, so we can not compare the field strength at our starting density of 10^{-13} g cm^{-3}. Initial solid-body rotation was also not included in our initial conditions, but from our turbulent velocity field we calculate that the ratio of total magnetic energy to rotational kinetic energy is ~ 2 when we introduce the field to the cropped box, making our model magnetically dominated. Despite this, there is no evidence for jet launching in our simulations. This is due to our use of a realistic $P(k) \propto k^{3/2}$ magnetic field power spectrum, which results in misaligned field vectors and hence the misaligned directional force of magnetic tensions. Also, our inclusion of a turbulent velocity field promotes fragmentation of the disc, differentiating the set-up from the idealised rotating

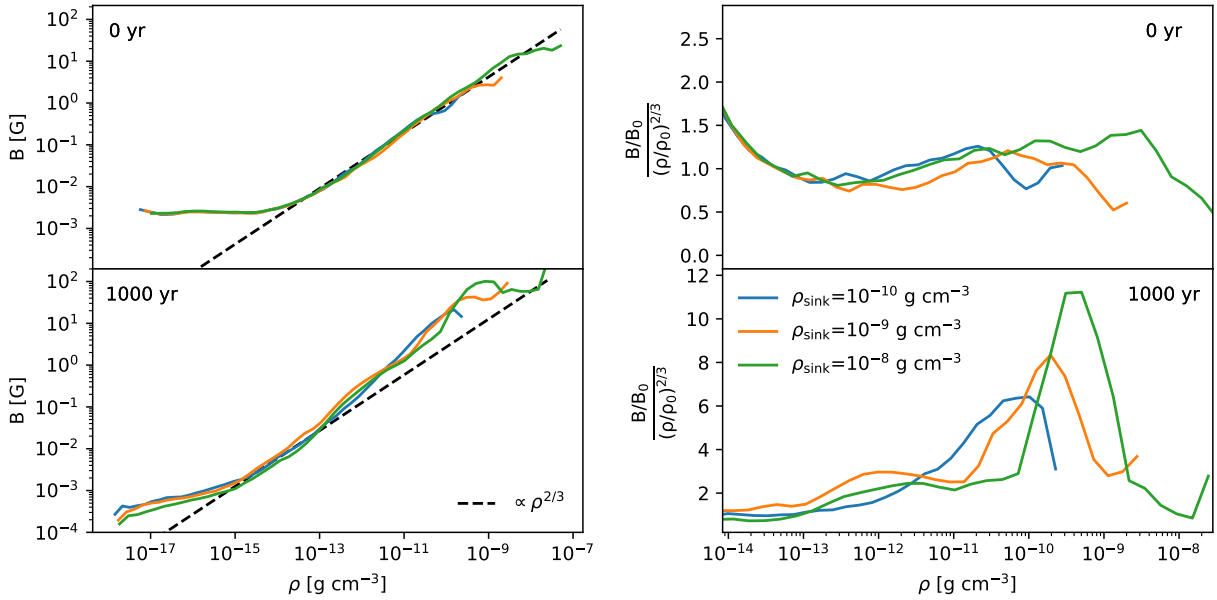

Figure 5.10. Left: volume-weighted magnetic field strength as a function of density for the three maximum resolutions considered from seed field C, shown at a time just before the formation of the first sink particle (top) and 1000 yr later (bottom). The dashed line shows the field growth expected from flux freezing. Right: Field strengths divided by the flux freezing line, such that growth above values of 1 indicate dynamo amplification.

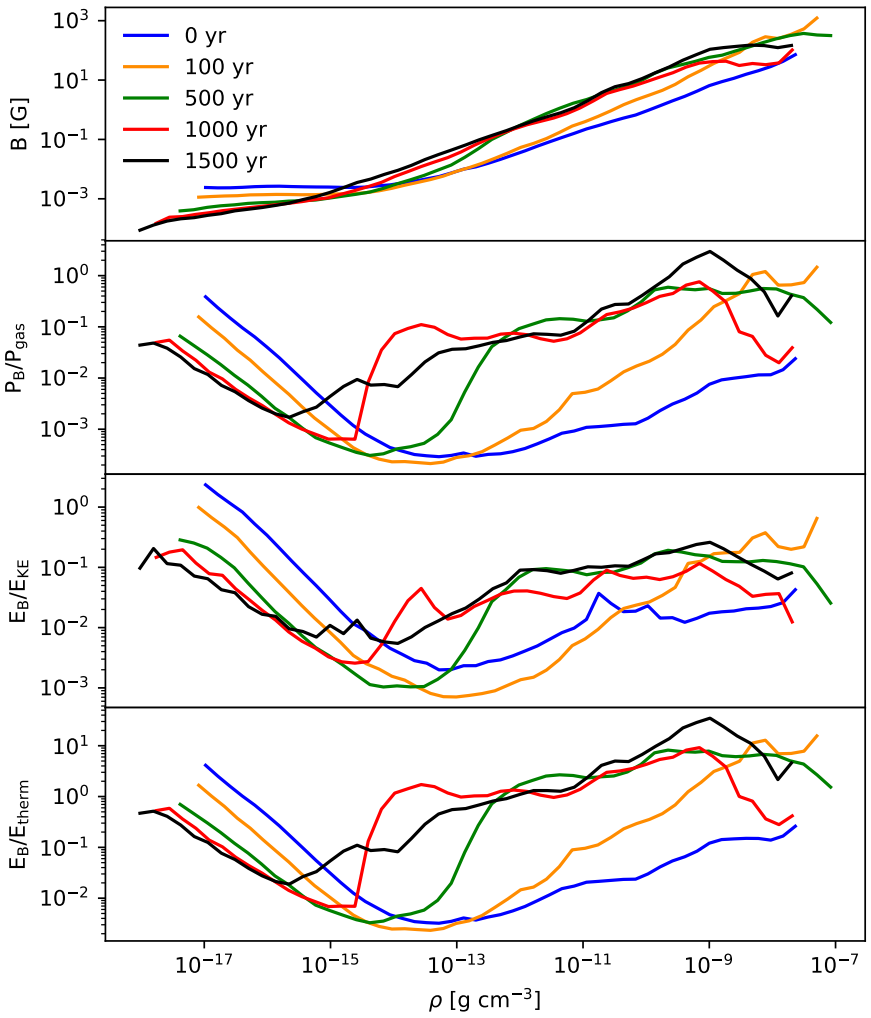

Figure 5.11. Volume-weighted density profiles for seed field C of the magnetic field strength, ratio of magnetic to thermal pressure, ratio of magnetic to kinetic energy and ratio of magnetic to thermal energy.

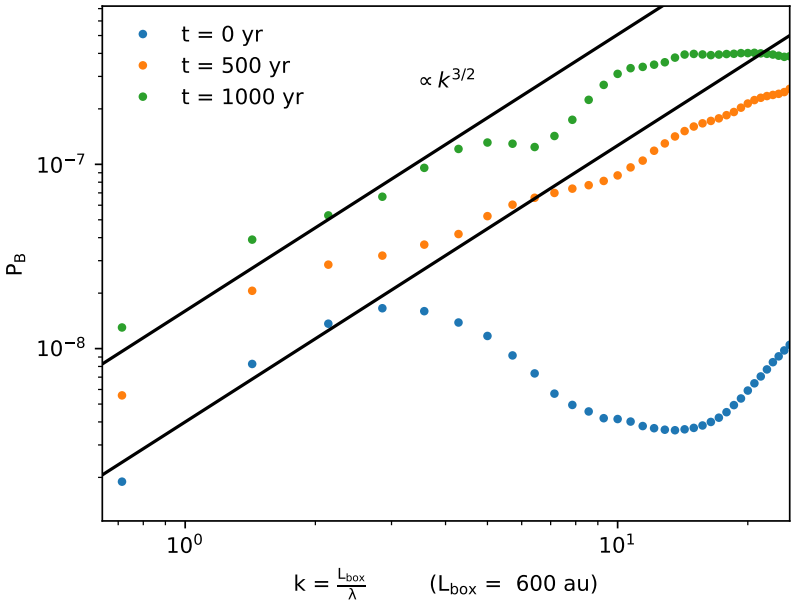

Figure 5.12. The magnetic power spectra within the central 600 AU at times 0, 500 and 1000 yr after the formation of the first sink, for seed field C. The highest modes shown on the plot correspond to scales of 25 au. The black lines show a $k^{3/2}$ power law.

cloud used in Machida et al. (2008) and Machida & Doi (2013).

Sharda et al. (2020) used a $P(k) \propto k^{3/2}$ power spectrum, finding suppressed fragmentation and a reduction in the number of first stars with masses low enough that they might be expected to survive to the present-day. The magnetic field strengths at their maximum density of 10^{-11} g cm^{-3} are similar to ours at the same density (1-10 G). However, they introduce their fields at a much lower density and hence poorer mesh resolution, and only populate the magnetic field with 20 modes throughout the 2.4 pc box. This raises concerns that the $k^{3/2}$ spectrum could be under-sampled, possibly allowing the magnetic field to be artificially uniform within the collapsing region. To demonstrate this, we repeat the initial non-magnetised stage of the collapse described in Section 5.1.1 with an initial $P(k) \propto k^{3/2}$ magnetic field consisting of 20 modes, scaled to $E_{\rm B}/E_{\rm KE} = 0.1$ to replicate the strong field case in Sharda et al. (2020), giving an rms field strength of 1.01 μG. We repeat the simulation with a ratio of 1 to compare with the method from this paper, giving a field strength of 3.18 μG. We allow the gas to collapse to the point where our non-magnetised box was cropped and our magnetic field was interpolated onto the AREPO cells. Figure 5.13 compares the gas structure and power spectra of the fields at that point within the central 0.032pc cropped box. Our freshly introduced field is roughly $P(k) \propto k^{3/2}$ while the evolved fields have almost flat power spectra, indicating equal energies on all scales,

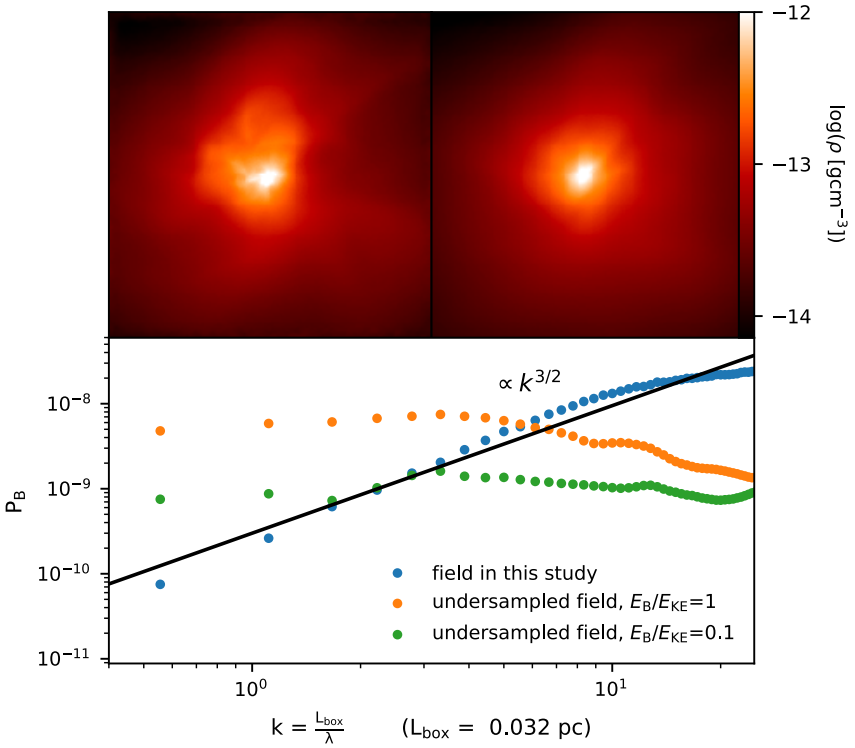

Figure 5.13. Comparison of introducing a magnetic field late in the collapse versus introducing a low resolution field at the beginning of the collapse. Top - density projections of the non-magnetised (left) and $E_{\rm B}/E_{\rm KE}$=1 magnetised (right) clouds at the point when our tangled field is introduced as described in Section 5.1.2. Bottom - Magnetic power spectrum of the field we interpolate onto the cells (blue) compared to the evolved spectra of the fields introduced at the beginning of the simulation at $E_{\rm B}/E_{\rm KE}$=1 (orange) and 0.1 (green). The black line shows a $k^{3/2}$ power law.

which is not predicted by Kazantsev theory. The top panels of Figure 5.13 compare the gas structure of our magnetised initial conditions with the $E_{\rm B}/E_{\rm KE}$=1 simulation described above. The lack of significant difference in the structure supports our assumption that the field does not affect the collapse of the gas significantly before the point where we introduce our magnetic field. We attribute the lack of magnetic support in our study compared to Sharda et al. (2020) to our improved method of sampling the tangled $P(k) \propto k^{3/2}$ spectrum, along with our increased maximum densities and spatial resolution allowing fragmentation on smaller Jeans scales.

5.5 Caveats

The weak magnetic seed fields undergo amplification via the small-scale magnetic dynamo, during the early stages of collapse. In our initial non-magnetised simulations, we have assumed

that the magnetic fields are too weak to affect the collapse, and only account for magnetic effects once the field is expected to have saturated. The magnetic fields generated from the $k^{3/2}$ spectrum are random, whilst the fields resulting from a fully magnetised treatment would be structured by the collapsing density distribution and velocity field. Furthermore, while the initial conditions were set up to a field energy at equipartition with the velocity field (i.e. their theoretical maximum strength and hence maximum support against fragmentation), Figure 5.11 clearly shows that the equipartition did not survive the early stages of collapse. We suspect that this is due to averaging the energies over the whole simulation box and spreading the field energy equally over entire volume, most of which did experience collapse. However, previous studies have found saturation ratios of the dynamo in the range of $\sim 0.01 - 0.6$, which is in line with the fields in this study.

Our method of calculating the rms field strength was dependant on the mean kinetic energy in the cropped simulation box, which is sensitive to the size of the cropped box. Zooming into a smaller region around the center of collapse gives a higher average kinetic energy and hence a higher rms magnetic field strength. Our cropped box size was chosen to provide a large enough cloud to allow collapse for sufficient time without causing issues with the periodic boundary conditions.

Although we remove compressive modes from the magnetic fields generated from the $k^{3/2}$ power spectrum, $\nabla \cdot \vec{B}$ errors are produced when the field is interpolated onto the AREPO non-uniform mesh. During the early stages of collapse, these errors are cleaned as described in Section 2.1.1. Our simulations also suffer from numerical diffusion. The combination of these effects results in a loss of magnetic energy in the early stage of collapse. While these issues would be reduced by implementing a magnetic field with fewer modes i.e. neglecting the smallest spatial scales, this is the equivalent of scaling up the magnetic energy on larger scales. It is more important to scale the magnetic field to distribute the magnetic energy according to the $k^{3/2}$ power spectrum, even if the highest energies on the smallest scales are lost due to numerical effects. We note that after the loss of energy, the field strength agrees with that of Federrath et al. (2011a) at the corresponding density.

This study does not incorporate the effects of non-ideal MHD. Ohmic, Ambipolar and Hall diffusion are not considered, but contribute to the breakdown of flux freezing. Ohmic dissipation can redistribute magnetic flux from dense regions and enable the formation of rotationally supported discs around protostars (e.g. Tomida et al. 2012). Ambipolar diffusion causes magnetic decoupling (Desch & Mouschovias, 2001) and creates a magnetic diffusion barrier in the vicinity of the core, limiting the field amplification and hindering magnetic braking (Masson et al., 2016). The Hall effect occurs at intermediate densities when neutral collisions preferentially decouple ions from the magnetic field, leaving only the electrons to drift with the magnetic field (e.g. Pandey & Wardle 2008). However, inclusion of these effects leads to decreased magnetic field strength (e.g.

Masson et al. 2016; Wurster et al. 2021), so the inclusion would not aid in the suppression of fragmentation.

5.6 Conclusions

We have investigated the ability of saturated primordial magnetic fields to suppress the fragmentation of gas during Pop III star formation. We present two-stage MHD zoom-in simulations, whereby random $k^{3/2}$ magnetic fields were superimposed onto the system when the central density achieved 10^{-13} g cm^{-3}. We have tracked the fragmentation behaviour of the systems for ~ 1000 yr after the formation of the first sink particle. The simulations were repeated for sink particle creation densities in the range 10^{-10}-10^{-8} g cm^{-3}. Within this range the magnetic pressure remained sub-dominant or comparable with the thermal pressure, providing inadequate support to prevent Jeans instabilities from fragmenting the system. The total number of sink particles formed did not reduce in the magnetised case compared to the purely hydrodynamic scenario. The total mass accreted onto sink particles and the resulting IMFs were also unaffected by the field. As we have not resolved up to stellar core densities, it is possible that the magnetic pressure will become the dominant pressure term in the density range of 10^{-8}-10^{-4} g cm^{-3} before the adiabatic core forms, which could suppress fragmentation on the smallest scales not explored in this work. Our results suggest that the inclusion of magnetic fields in numerical simulations of Pop III star formation is unimportant, especially in studies where the maximum resolution is too poor to resolve the scales at which the magnetic pressure could become the dominant support term. Additionally, placing a uniform field over the central collapsing region did result in reduced fragmentation, demonstrating the danger of under-resolving the initial $k^{3/2}$ field in future studies.

Chapter 6

High resolution follow-up of cosmological Lyman-Werner simulations

Chapter 3 argues that when properly resolved, primordial gas fragments to produce low mass stars capable of surviving until the present day, while Chapter 5 argues that evoking primordial magnetic fields does not provide support to prevent this fragmentation. As accretion of metals onto the surface of these stars during their lifetime is unlikely (e.g. Johnson & Khochfar 2011; Tanaka et al. 2017), the question is raised about why these stars have not be found within archeological surveys (see e.g. Beers & Christlieb, 2005; Frebel & Norris, 2015; Starkenburg et al., 2017).

To briefly summarise Section 1.3.3, the first stars were able to form because pristine baryonic gas collapsed within the gravitational potential well of dark matter (DM) halos (Couchman & Rees, 1986; Haiman et al., 1996b; Tegmark et al., 1997), heating it to ~ 5000 K and facilitating the formation of H_2 (Bromm et al., 2002) via the channel shown in Equation 1.39. Radiative cooling from the molecular hydrogen rendered the gas gravitationally unstable, which allowed it to decouple from the DM and collapse to form the first stars. The necessity of H_2 renders any process of H_2 destruction as a mechanism to delay or prevent Pop III star formation, such as LW photons produced by Pop III.1 stars as reviewed in Section 1.3.7. This chapter covers work originally presented in Prole et al. (2023), which investigates whether radiation feedback from Pop III.1 stars can increase the mass of Pop III.2 stars and if the number of stars with masses low enough to survive until today can be reduced by the mechanism. We perform high resolution follow-up simulations around selected halos from the cosmological simulations of Schauer et al. (2021) (hereafter AS21).

6.1 Sink particle parameter study

Before discussing the simulations, it is worth noting that the simulation boxes are orders of magnitude larger in this chapter than in the previous investigations. As such, an investigation was carried out into the simulation parameters in an attempt to reduce the computational cost of the simulations without losing accuracy and quality.

The cells that span across a sink particle are typically the smallest and hence densest cells in simulations. Though the total number of cells near the minimum cell volume may be small compared to the total number of cells in the simulation, their contribution to the computational resource usage can be sizable due to the high densities and accelerations involved. There are 2 parameters that need to be optimised for a cheaper sink particle treatment: the minimum cell volume $\mathrm{V_{min}}$ and minimum gravitational softening length $\mathrm{L_{soft}}$ with respect to the sink particle radius. The Truelove condition requires at least 4 cells per Jeans length, this corresponds to a minimum cell size of 2 cells across the sink particle radius R_{sink} as our lowest resolution test case. We also test 4 and 8 cells per R_{sink}. For each of these cases, we test a range of minimum gravitational softening lengths from $2R_{\mathsf{sink}}$ down to $(\mathrm{V_{min}})^{1/3}$. We chose a simple set up of a rotating cloud seeded with angular density enhancements to promote the creation of a binary, as described in Section 2.1.4. We use a barotropic equation of state with ρ_{sink}=10^{-13} g cm^{-3} and R_{sink}=28 au. Figure 6.1 shows the total mass accreted onto sinks as a function of time for the 3 minimum cell volumes. The results converge when $\mathrm{L_{soft}}$ is half the sink radius or smaller when $\mathrm{V_{min}}$ allows 4 or 8 cells per R_{sink} (this would be smaller than $(\mathrm{V_{min}})^{1/3}$ for the 2 cell case). Furthermore, Figure 6.2 compares the cases where $\mathrm{L_{soft}}$ is half the sink radius for each $\mathrm{V_{min}}$, which also agrees that the accretion behaviour is almost identical for all values of $\mathrm{V_{min}}$ as long as $\mathrm{L_{soft}}$=$R_{\mathsf{sink}}/2$. It is generally accepted that while the Truelove condition requires 4 cells across a Jeans length, more resolution is required to prevent artificial fragmentation, so we opt to adopt 4 cells per R_{sink} (8 cells per Jeans length) with $\mathrm{L_{soft}}$=$R_{\mathsf{sink}}/2$ as the sink particle parameters moving forward.

6.2 Cosmological simulations

The cosmological simulations performed by AS21 assumed a ΛCDM cosmology with parameters $h = 0.6774$, $\Omega_0 = 0.3089$, $\Omega_\mathrm{b} = 0.04864$, $\Omega_\Lambda = 0.6911$, $n = 0.96$ and $\sigma_8 = 0.8159$ as derived by the Planck Collaboration et al. (2020). The simulations were initialised at $z = 200$ with an initial DM distribution created by MUSIC (Hahn & Abel, 2011) using the transfer functions of Eisenstein & Hu (1998) and the gas distribution initially followed the DM. The DM was represented by

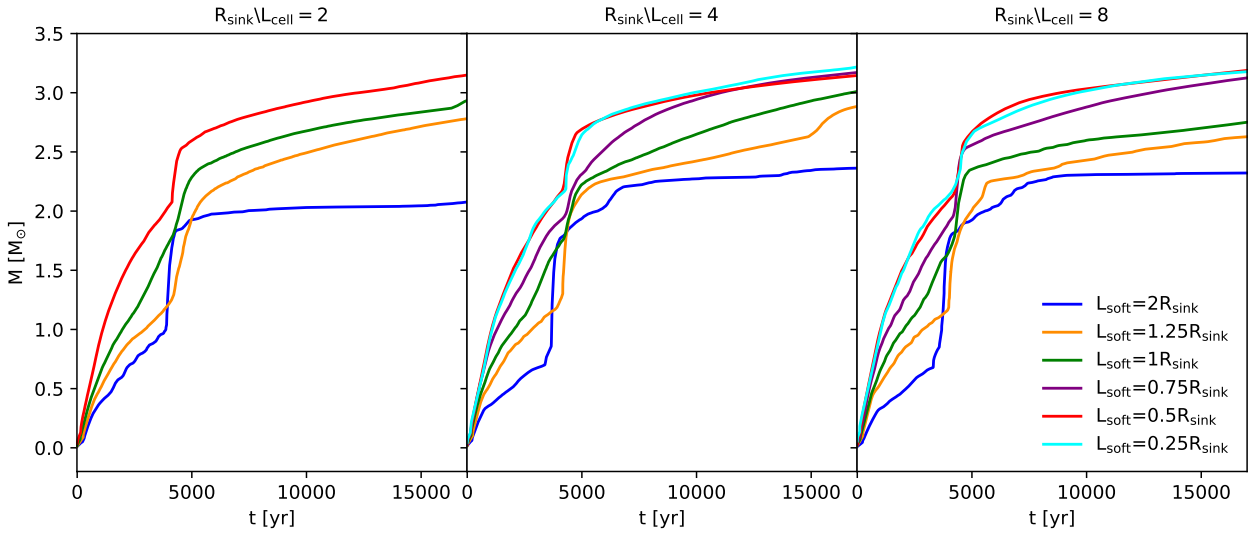

Figure 6.1. Total mass accreted onto sinks as a function of time for different gravitational softening lengths L_{soft} and different minimum size scales L_{cell}=$V_{min}^{1/3}$.

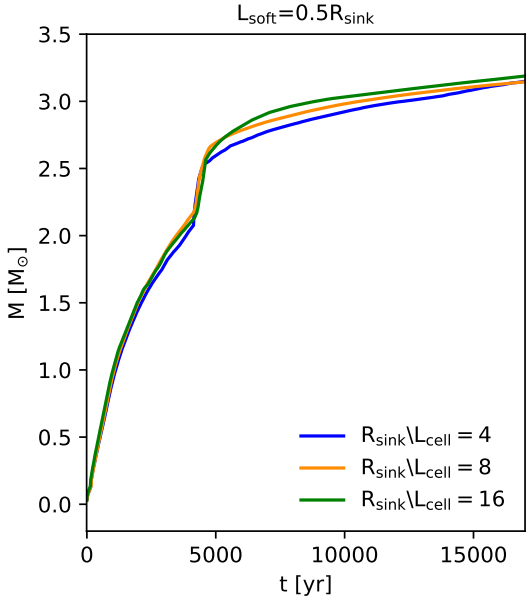

Figure 6.2. Comparison of the total mass accreted onto sinks as a function of time for different minimum size scales L_{cell} when the minimum gravitational softening length is fixed at half of the sink particle radius.

1024^3 particles and the gas was initially modelled with 1024^3 grid cells, all contained within a box with side length $1h^{-1}\mathrm{Mpc}$ in comoving units. During the simulation, an additional Jeans refinement criterion was applied: cells were refined whenever necessary so as to ensure that the Jeans length was always resolved with at least 16 cells. This refinement was carried out until the gas reached a threshold density of $\sim 10^{-19}$ g cm^{-3}. Above this threshold density, gravitationally bound and collapsing gas was converted into collisionless sink particles, as explained at greater length in AS21. The simulations were carried out with four different values of the baryonic streaming velocity ($v_{\mathrm{str}} = 0, 1, 2$ and 3, in units of σ_{rms}, the large-scale root mean squared value) and three different values for the LW field strength ($J_{21} = 0$, 0.01 and 0.1). In this study, we make use of the three simulations with $v_{\mathrm{str}} = 1\sigma_{\mathrm{rms}}$ because this is the most representative value available, as the volume fraction of streaming velocities peaks at $0.8\sigma_{\mathrm{rms}}$ (AS21).

6.3 Halo selection

Given snapshots at $z = 15$ from the three simulations with $v_{\mathrm{str}} = 1$ presented in AS21, we have selected 5 halos for each value of J_{21}. Halo positions and masses were provided by the friends-of-friends (FoF) algorithm as described in that study. The selection criteria for the halos was as follows:

- The halos identified by the FoF algorithm were sorted by their mass difference with $\mathrm{M_{av}}$, the average minihalo mass above which minihalos become capable of cooling and forming stars. This average mass was defined in AS21, following Schauer et al. (2019), to be the minihalo mass above which more than 50% of minihalos can cool and form stars.* AS21 report $\mathrm{M_{av}}$ at a range of redshifts between $z = 22$ and $z = 14$; here, we adopt their values at $z = 15$. By sorting the halos in this way, we ensure that the halos that we eventually select will have masses close to $\mathrm{M_{av}}$, i.e. that they are representative of the common case at that redshift.
- We considered a halo if it contained a cell denser than $\rho_{\mathrm{th}} = 10^{-22}$ g cm^{-3} within a search radius $\mathrm{R_{search}} = 1$ kpc in physical units from the halo's central coordinate. Note that checking the H_2 abundance is not necessary, as collapse to this density is not possible without a high H_2 abundance outside of the atomically cooling halo scenario.
- We check that the halo is sufficiently resolved i.e. that the 16 cells per Jeans length criteria has not decreased as the cell sizes approach the maximum resolution of the cosmological simulations. This process begins when the density reaches $\sim 10^{-20}$ g cm^{-3}, so we reject

*Note that $\mathrm{M_{av}}$ is typically around a factor of three larger than M_{min}, the mass of the least massive minihalo with cool gas.

Table 6.1. Total mass (DM and gas) as detected by the FoF algorithm within the selected halos from Schauer et al. (2021).

	J_{21}=0	J_{21}=0.01	J_{21}=0.1
halo	M_{tot} [10^6 $M_\odot$]		
1	3.50	4.76	8.70
2	3.65	4.84	8.30
3	2.81	4.30	6.70
4	2.76	4.02	4.15
5	2.96	3.91	3.90

halos including a cell above this density. Note that this also ensures that a sink particle has not yet been formed within R_{search}.

- Lastly, we removed the halo from consideration if there were other dense objects in the vicinity by checking there were no cells above ρ_{th} within the radius $R_{search}/2 < r < R_{search}$.

We performed this search throughout the simulation cube until 5 suitable halos were selected for each J_{21} value. After converting the units from co-moving to physical, we cropped a 2 kpc box around each of the halos for our zoom-in simulations. The selected halo masses from each simulation are shown in Table 6.1. Mass-weighted mean temperatures and H_2 abundances are plotted as a function of density for each halo in Figure 6.3 and radial distributions of enclosed gas and DM along with velocity information are shown in Figure 6.4. Projections of the initial density, temperature and H_2 abundance distributions are visualised in Figures 6.5, 6.6 and 6.7. Note that all of these figures show the state of the halos at the point at which we extract them from the AS21 simulations, i.e. prior to our zoom-in calculation. Our choice of selection criteria means that the same halos are not chosen for direct comparison between each simulation. Rather, they are chosen to be most representative of the Universe at the given background LW field strength. Direct comparison also has the drawback that individual halos will collapse at different redshifts depending on the LW field strength, whereas we exclusively select halos that become able to form stars at $z = 15$.

6.4 Sink particles

The zero metallicity protostellar model of Machida & Nakamura (2015) suggests that stellar feedback kicks in to halt collapse at $\sim 10^{-6}$ g cm^{-3} (10^{18} cm^{-3}), so we choose this as our sink particle creation density. The initial accretion radius of a sink particle R_{sink} is chosen to be the Jeans length λ_J corresponding to the sink particle creation density and corresponding temperature. At 10^{-6} g cm^{-3}, we take the temperature value from LP22 of 4460 K to give a Jeans length of

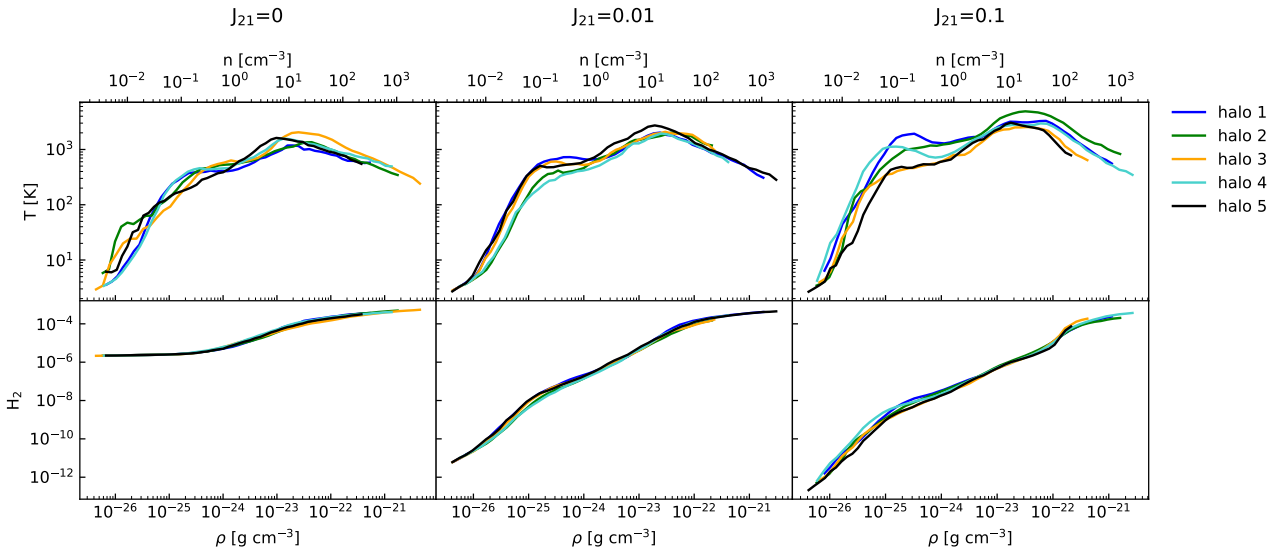

Figure 6.3. Summaries of the initial conditions for our simulations. Mass-weighted density profiles of temperature and H_2 abundances.

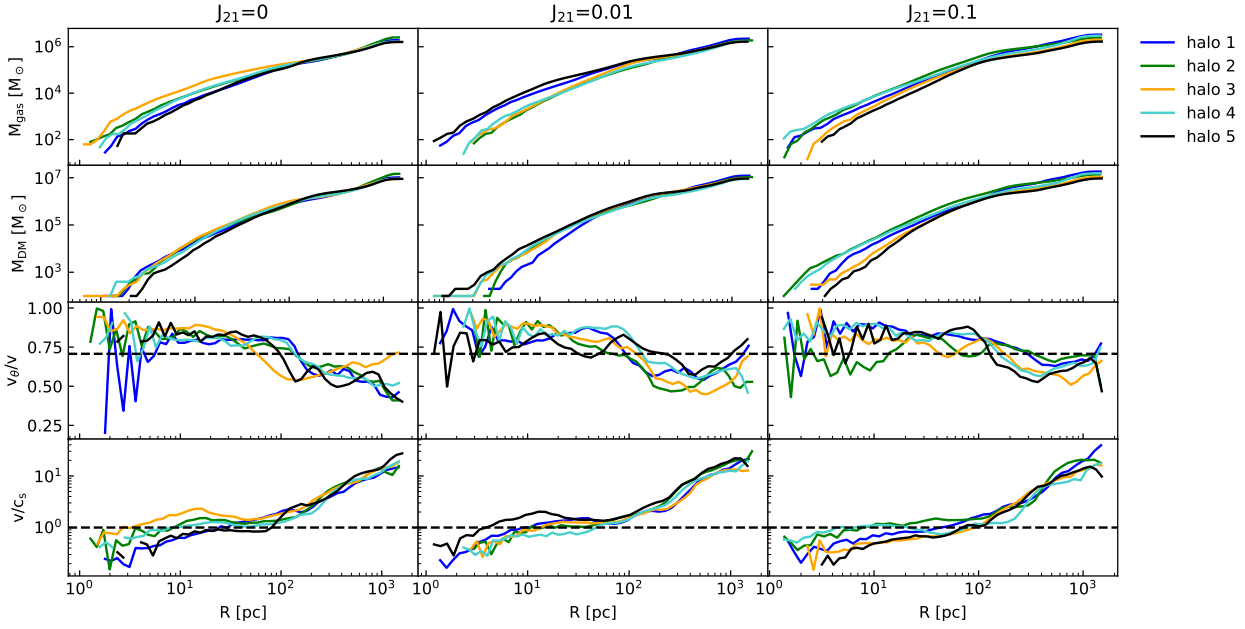

Figure 6.4. Summaries of the initial conditions for our simulations. Cumulative radial profiles of gas and DM mass and mass-weighted radial profiles of the ratio of rotational to total velocity (note the dotted line represents the value above which rotational component dominates the velocity) and ratio of velocity to sound speed i.e. Mach number.

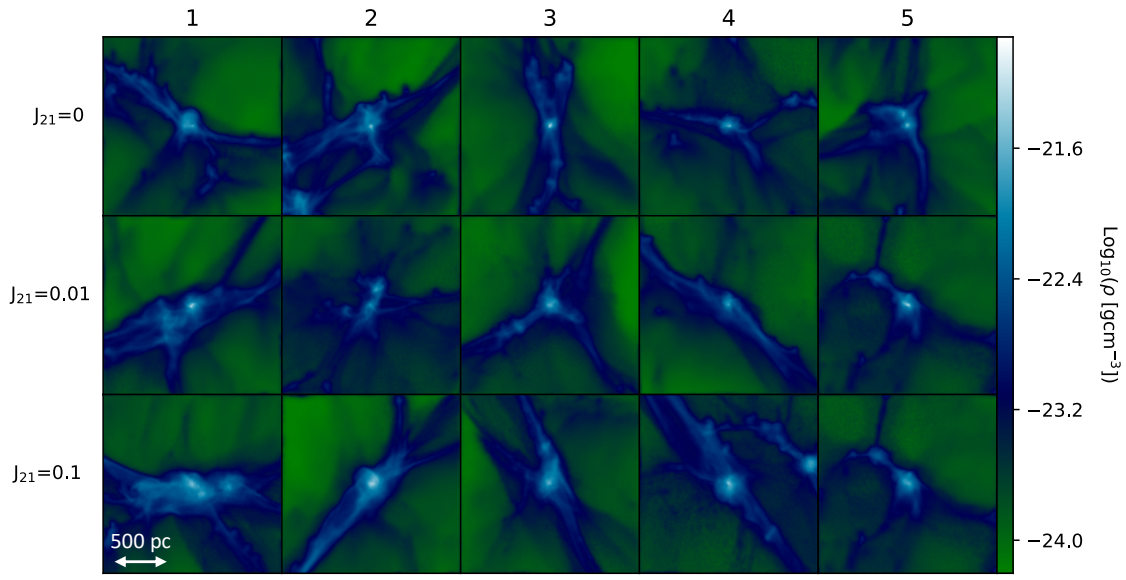

Figure 6.5. Column-weighted density projections of the 2 kpc region around the 5 cosmological halos for each J_{21} value, taken from Schauer et al. (2021), which serve as the initial conditions of the high resolution follow-up simulations presented in this work. The halo numbers to compare with upcoming plots are indicated at the top of the figure.

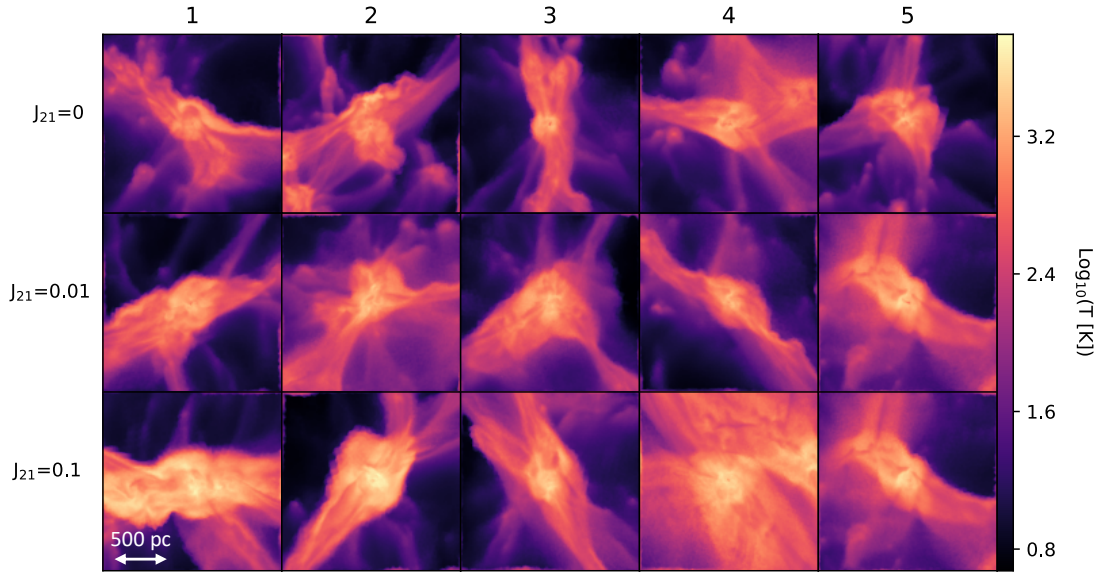

Figure 6.6. Column-weighted temperature projections of the 2 kpc region around the 5 cosmological halos for each J_{21} value, taken from Schauer et al. (2021), which serve as the initial conditions of the high resolution follow-up simulations presented in this work.

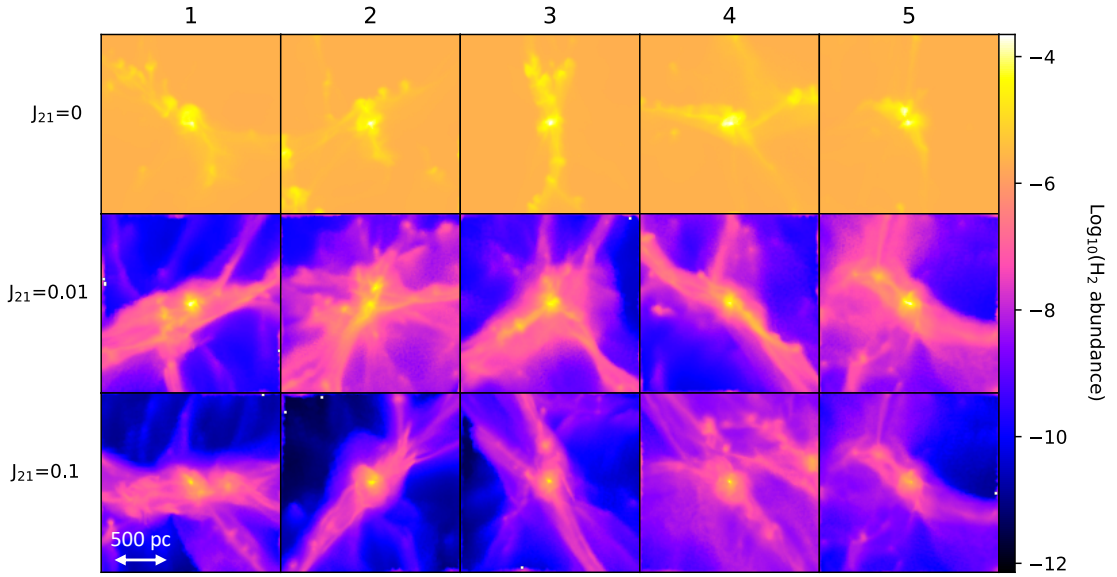

Figure 6.7. Column-weighted H_2 abundance projections of the 2 kpc region around the 5 cosmological halos for each J_{21} value, taken from Schauer et al. (2021), which serve as the initial conditions of the high resolution follow-up simulations presented in this work.

1.67×10^{12} cm. We set the minimum cell length to fit 8 cells across the sink particle in compliance with the Truelove condition, by setting a minimum cell volume $V_{\text{min}} = (R_{\text{sink}}/4)^3$. The minimum gravitational softening length for cells and sink particles L_{soft} is set to $R_{\text{sink}}/4$.

The increasing radius of a Pop III protostar is dependent on both its mass and accretion rate (e.g. Omukai & Palla 2003; Hosokawa & Omukai 2009; Hosokawa et al. 2012; Hirano et al. 2014). We allow the sink particle accretion radius R_{sink} to vary throughout its accretion history, using on-the-fly calculations of the stellar radius using an approximate analytic formulae originally derrived by Stahler et al. (1986):

$$R_{\text{sink}} = 26 R_{\odot} \left(\frac{M}{M_{\odot}} \right)^{0.27} \left(\frac{\dot{M}}{10^{-3} M_{\odot} \text{yr}^{-1}} \right)^{0.41}, \tag{6.1}$$

where we smooth $\dot{M}$ by taking the average over the time taken to accrete $0.1 M_{\odot}$.

6.5 Initial halo characteristics

Figures 6.3 and 6.4 show some of the characteristics of the halos at the time when they were selected for zoom-in follow-up simulations. The top panel of Figure 6.3 shows that the gas has

already been shock heated as it fell into the gravitational potential well of the DM halo, allowing it to produce the necessary H_2 to cool and collapse to higher densities. The bottom panel shows the destructive impact of the LW radiation field on the H_2 abundance in the outer regions of the halo. The H_2 abundance in the central regions reaches the same peak value of 4×10^{-4} due to self-shielding from the radiation field, however this happens at increasingly higher densities for larger J_{21} values. Figure 6.4 shows that within ~ 100 pc, the gas velocity is dominated by the component perpendicular to the radius vector, v_θ. The gas surrounding the halos is highly supersonic due to large-scale streaming, which cascades down to become subsonic at scales smaller than ~ 10 pc, although we show in Section 6.6 that the velocities do not remain subsonic once the gas collapses further. From the density projections of Figure 6.5, halo sizes range from $\sim 100 - 200$ pc, their shapes range from roughly spherical to structurally complex, and each is embedded within a network of filamentary structures. Figure 6.6 shows that these webs of filaments are a few hundred Kelvin hotter than the ~ 10 K gas that surrounds them, with the central halo reaching $\sim 1000 - 2000$ K. Figure 6.7 shows how the background H_2 abundance is reduced drastically by the LW background, with significant levels of H_2 only appearing in the central regions of the halo.

6.6 Further collapse

We continue the collapse down to densities of 10^{-6} g cm^{-3} before inserting sink particles. Figure 6.8 shows temperature and chemical abundance profiles as a function of density, just before the formation of the first sink particle. At densities above 10^{-15} g cm^{-3}, three-body H_2 formation raises its abundance to over 0.1 within the *molecular core*. The abundance of free electrons falls off with density as the gas recombines. Figure 6.9 shows radial profiles of density and velocity. The rotational component of the gas velocity remains dominated by rotation only down to scales of ~ 1 pc, below which infall begins to dominate. The velocities remain supersonic down to scales of 10^{-6} pc (0.2 au). Halos experiencing a LW field are capable of achieving higher velocities, likely due to the higher halo mass.

The left hand side of Figure 6.10 compares the temperature, density, accretion timescale and H_2 abundance radial profiles for the different J_{21} values just before the formation of the first sink particle. Stronger LW fields require higher mass halos for star formation, as their stronger gravitational potential is capable of shock-heating the gas to higher temperatures, which increases the H_2 formation rate enough to build up a high column density of H_2 in order to self-shield the collapsing regions. Despite larger halo masses and shock-heating to higher initial temperatures, the density profile of the gas remains unaffected. Following Abel et al. (2002) and O'Shea &

Norman (2008), we have also estimated the accretion timescale ($t_{\rm acc} = {\rm M}/\dot{\rm M}$) where

$$\dot{\rm M} = 4\pi R^2 \rho(R) v_{\rm rad}(R) \tag{6.2}$$

is our estimate of the mass inflow rate at radius R and $\rho(R)$ and $v_{\rm rad}(R)$ are the mass-weighted density and radial velocity within shells at radius R. For $t_{\rm acc} < 10^4\,{\rm yr}$, there is very little difference between the runs, suggesting that the accretion rate at early times is not influenced by the LW field. For larger $t_{\rm acc}$, we do see a difference between different runs, but this manifests as an increased scatter in $t_{\rm acc}$ at a given R rather than any systematic dependence on the LW field strength.

The right hand side of Figure 6.10 shows the gas as it transitions into a fully molecular state within the inner $\sim 10^{-2}$ pc core corresponding to the density regime above 10^{-15} g cm^{-3}. Halos illuminated by a LW background have higher gas kinetic energies owing to their larger masses, which promotes a larger molecular core. However, the increasing photodissociation rate with increasing J_{21} acts against this mechanism, reducing the H_2 formation rate and shrinking the molecular core. This results in the $J_{21} = 0.01$ halos having molecular cores that extend to larger radii than the $J_{21} = 0.1$ halos, despite both having larger molecular cores than the $J_{21} = 0$ halos. As we only have access to these 3 values of J_{21}, the value where the core size is maximised could lie anywhere between $0 < J_{21} < 0.1$.

The importance of the molecular core is shown in Figure 6.11, which shows the total mass in sink particles at the end of the simulations as functions of the halo mass, virial temperature and mass within different regimes of the collapse, just before the maximum density was reached. The mass in sink particles grows almost linearly with the mass within the inner molecular core with H_2 abundances above 10^{-1} as

$$\log_{10}({\rm M_{sinks}}) = (0.85 \pm 0.11)\log_{10}({\rm M_{H_2 > 10^{-1}}}) + (0.14 \pm 0.24). \tag{6.3}$$

Due to competing effects between halo mass and H_2 photodissociation rate, the mass in sink particles is not correlated with the total halo mass or the subsequent mass that initially falls into its potential well with H_2 abundances $> 10^{-4}$. However, we have only followed the accretion for 300 yr, which corresponds to a free-fall time for gas at density 10^{-14} g cm^{-3}. Gas below this density will not have been accreted within the simulation time, while gas above this density resides within the molecular core (see Figure 6.8). It is therefore unclear if the relationship between accretion and mass of the molecular core would remain if the simulations ran for a longer time. If the relationship does hold, we speculate that increasing the size of the streaming velocities between gas and DM may have a greater effect on the IMF, since this also increases halo masses without the counteracting effects of H_2 dissociation (Tseliakhovich & Hirata 2010; Greif et al.

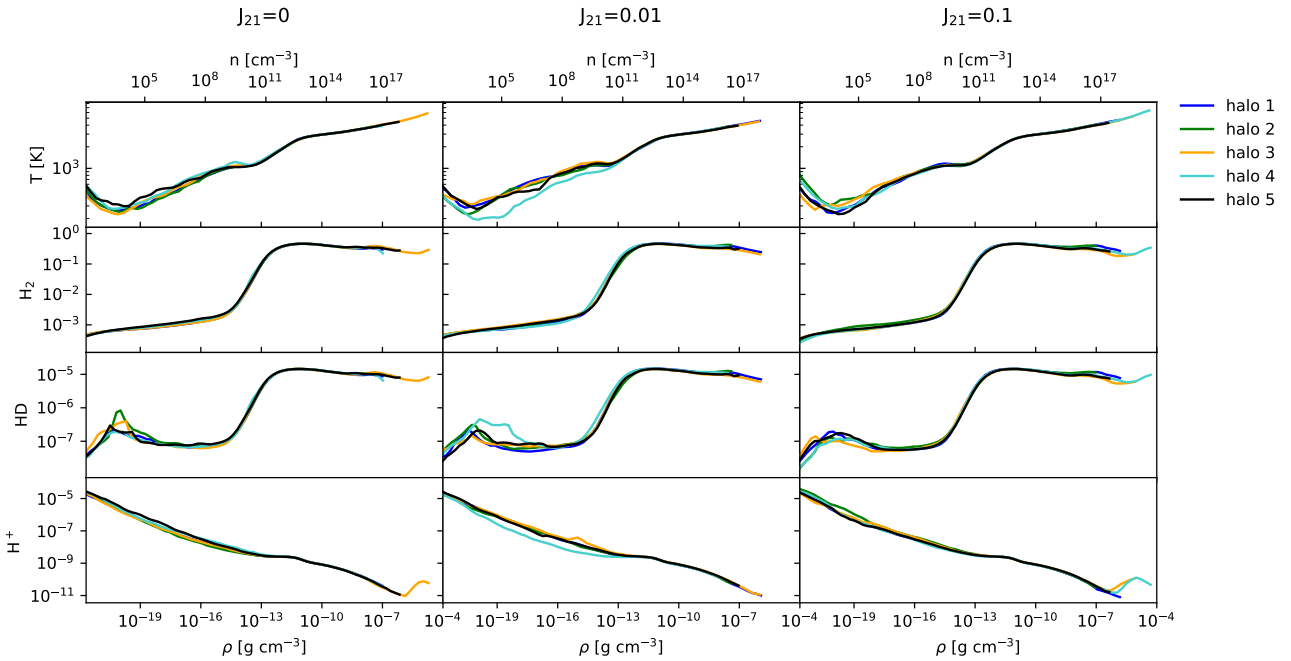

Figure 6.8. Mass-weighted temperature, H_2, HD and H^+ abundances versus density at a time shortly after the formation of the first sink particle. (Note that the HD abundance is only tracked self-consistently up to $\rho = 10^{-16}\,\mathrm{g\,cm^{-3}}$; above this, we simply fix the HD/H_2 ratio at 2.6×10^{-5}, as explained in Section 3.2).

2011a; Hirano et al. 2017; Schauer et al. 2019, AS21).

6.7 Fragmentation and the IMF

The IMF of Pop III stars is determined by the fragmentation behaviour of the disc around the initial central object and the subsequent accretion onto fragments. Density projections of the inner 650 AU of the halos are shown in Figure 6.12, while Figure 6.13 shows the evolution of the total number of sink particles formed, the total mass in sink particles and highest mass sink particle in each halo as a function of time. While the halos from the simulation without a LW background typically yield less fragmentation, the overall fragmentation behaviour is stochastic, as expected. The total mass accreted onto sinks is typically higher in the halos illuminated by a LW field due to their higher halo mass.

Figure 6.14 shows the IMF at a time 300 yr after the formation of the first sink particle. The peak of the IMF positioned at ∼0.2-0.5 $M_\odot$ shows little dependence on the LW strength, likely because the positive influence of larger halo masses on the molecular core is regulated by the increasing photodissociation rate. We also show the evolution of the cumulative IMFs in time, which converge by the end of the simulations for the J_{21}=0.01 and 0.1 suites. The left side of

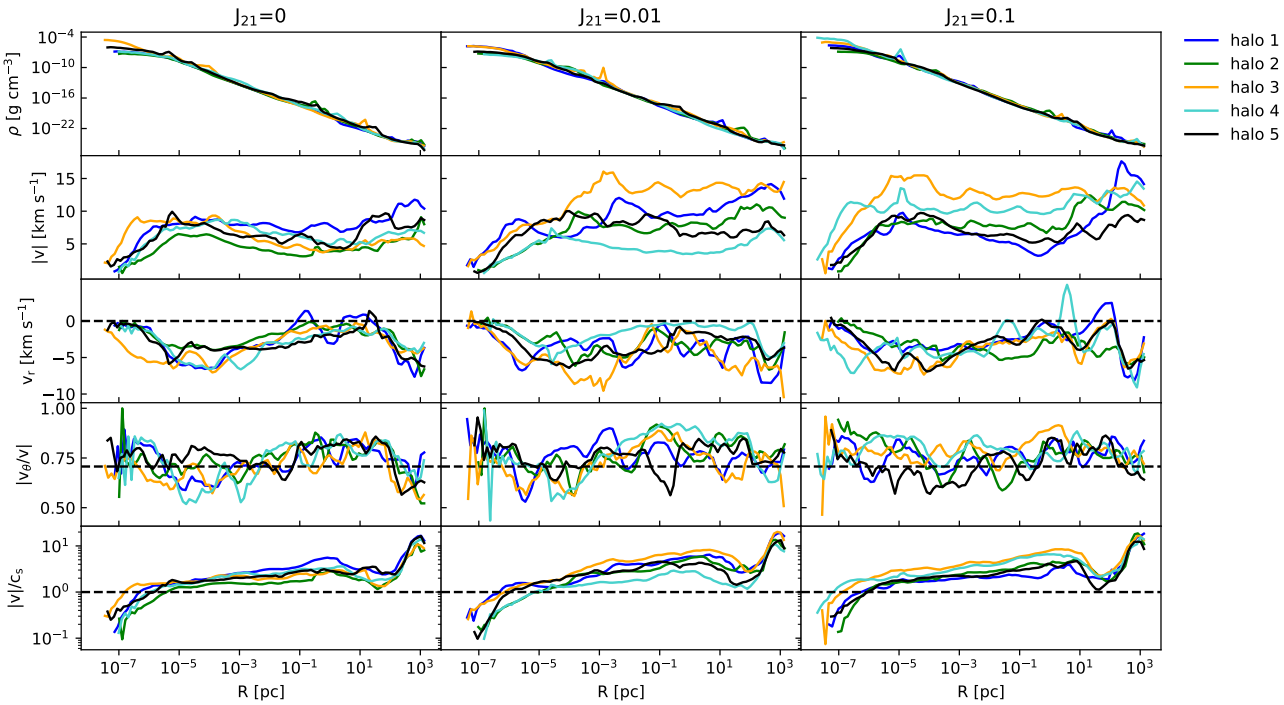

Figure 6.9. Radial distribution of cumulative gas mass and mass-weighted radial profiles of radial velocity, ratio of rotational to total velocity (note the dotted line represents the value above which rotational component dominates the velocity) and ratio of velocity to sound speed, taken at a time shortly after the formation of the first sink particle.

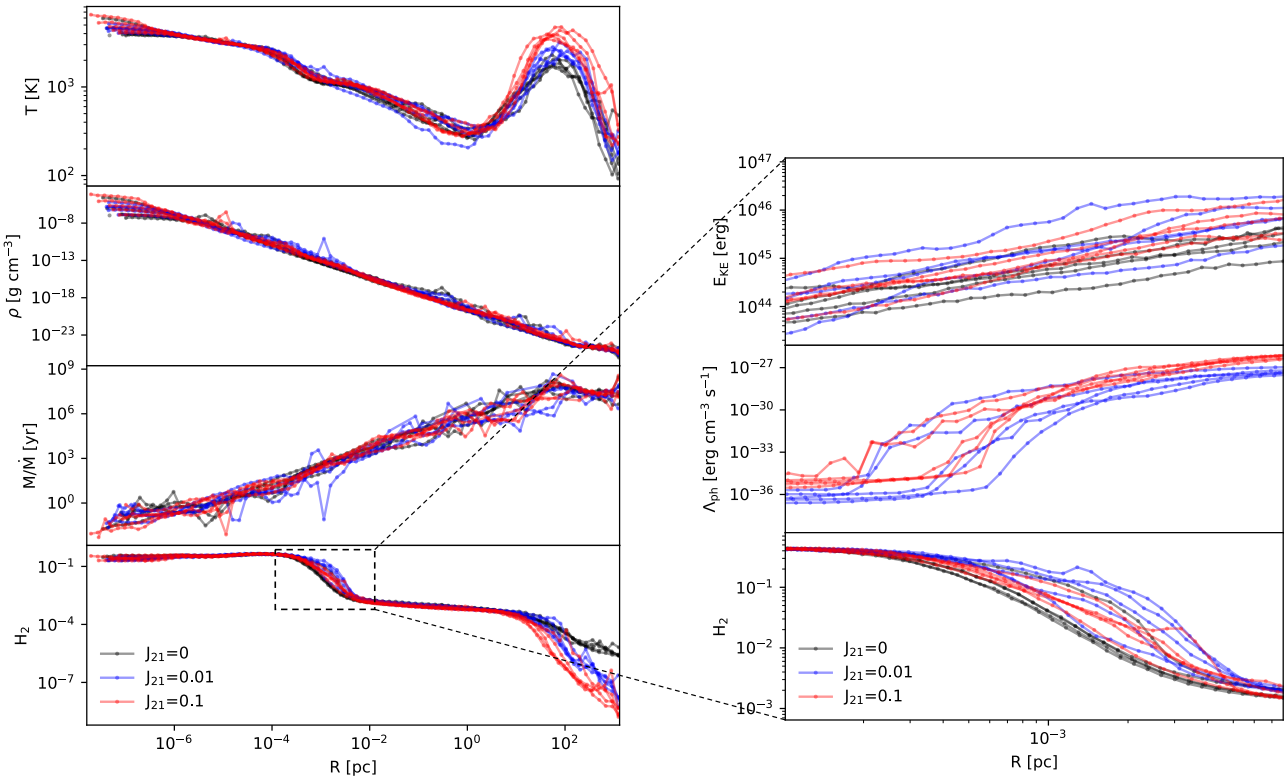

Figure 6.10. Left: Comparison of the mass-weighted temperature, density and and H_2 abundance profiles between the J_{21} values. Right: Zoom-in of the transition to fully molecular core, showing the total kinetic energy within radial shells, mass weighted H_2 photodissociation heating rate and H_2 abundance.

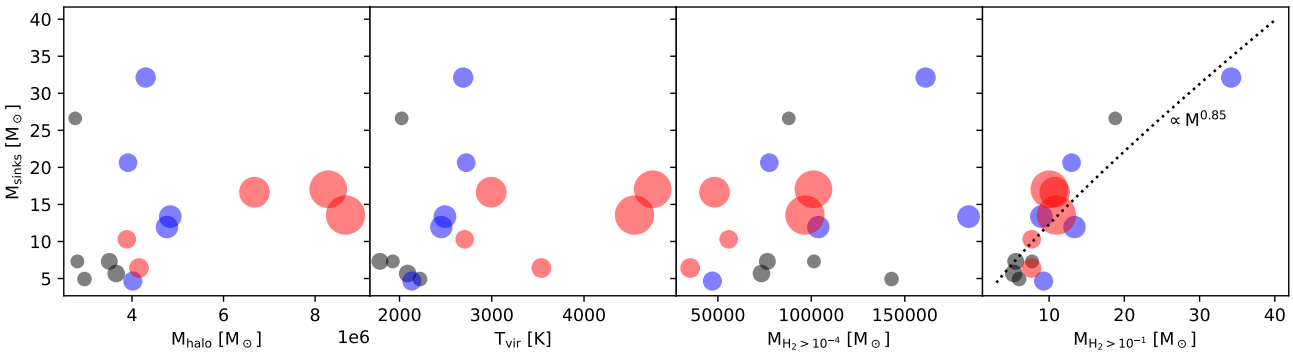

Figure 6.11. Total mass in sinks at the end of the simulations versus halo mass, virial temperature, mass within the halo with H_2 abundance $> 10^{-4}$ and mass within the molecular core with H_2 abundance $> 10^{-1}$. The size of the markers is scaled with the halo mass.

Figure 6.15 compares the combined cumulative IMFs for different J_{21} values. While the high mass end of the IMFs are nearly identical between the different J_{21} values, the low mass end of the IMFs show variance due to the random and stochastic nature of ejection events for low mass objects. Assuming these low mass objects ($< 0.075\mathrm{M}_{\odot}$) do not go on to accrete significant mass, they will remain as brown dwarfs and never sustain nuclear fusion. The right side of the plot shows the cumulative IMFs if the brown dwarfs are ignored. Here, the IMFs fit well within each other's regions of uncertainty, which are the standard deviations from the cumulative IMFs of the 5 halos individually. The overlap between the regions of uncertainty indicates that the LW strength does not significantly affect the primordial IMF. As the range of background LW field strengths tested here covers the most likely values from literature, we infer that the IMF for Pop III.2 stars is not significantly different from the initial population of Pop III.1 stars.

We also show the IMF from LP22 as a dotted line, which was produced from idealised halos as opposed to the cosmological initial conditions. The cosmological halos produced a bi-modal distribution with a significant population of brown dwarfs that the idealised halos are missing. Even when ignoring the brown dwarfs, the cosmological initial conditions have yielded distributions tending to lower mass protostars.

To compare the fragmentation behaviour of our simulations with the results of previous studies, we have recreated Figure 10 of Susa (2019) in Figure 6.16, which collected data from various studies. They found a power-law growth of the number of fragments with time. As the studies implemented different maximum densities, the time at the end of the simulations was scaled as $\tau/\sqrt{4\pi G\rho_{\mathrm{ad}}}$, where $\rho_{\mathrm{ad}} = 1.67 \times 10^{-5}$ is the maximum density of Greif et al. (2012) (see Susa 2019 for further details). The fragmentation behaviour in our simulations agrees well with the findings of Susa (2019). Our results appear advanced in time compared to the other studies despite only following 300 yr of fragmentation because of the high maximum density implemented in this study.

6.8 Caveats

Aside from the obvious uncertainties in the ΛCDM model on which this work and the work of AS21 are based on, there are a number of caveats to note.

The LW fields we have used in this study assume a population of massive Pop III stars already exists. While previous studies do suggest that Pop III stars were massive, more recent work suggests that they may only grow to a few $\mathrm{M}_{\odot}$ (e.g. Stacy & Bromm 2013; Wollenberg et al. 2020; Prole et al. 2022a; Jaura et al. 2022). In this scenario, significantly less LW radiation would be produced, however radiation from solar mass stars can inhibit H_2 formation through the destruction of H^-.

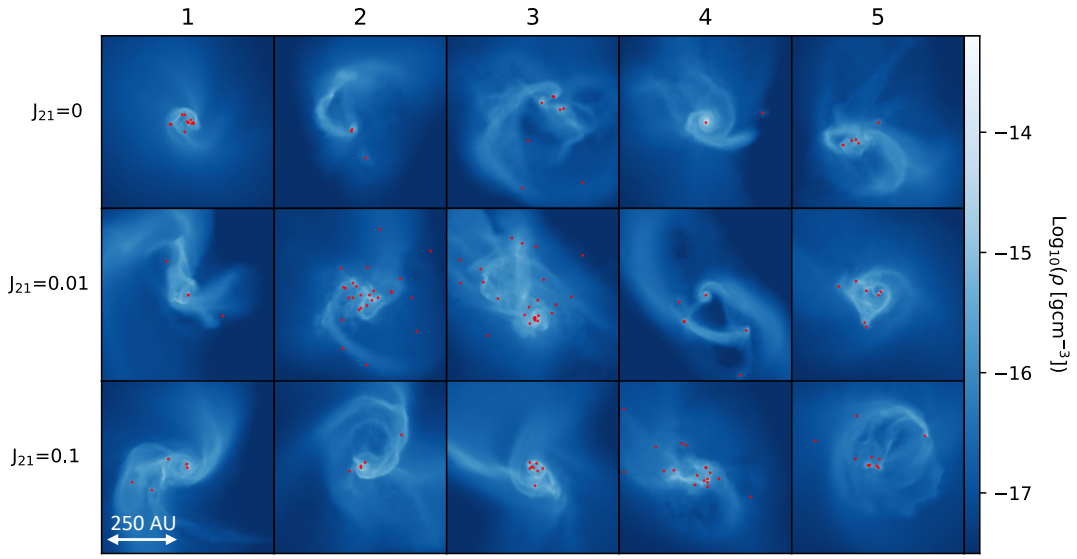

Figure 6.12. Column-weighted density projections of the inner 650 AU of the halos at a time 300 yr after the formation of the first sink particle. Sink particles are represented as red dots.

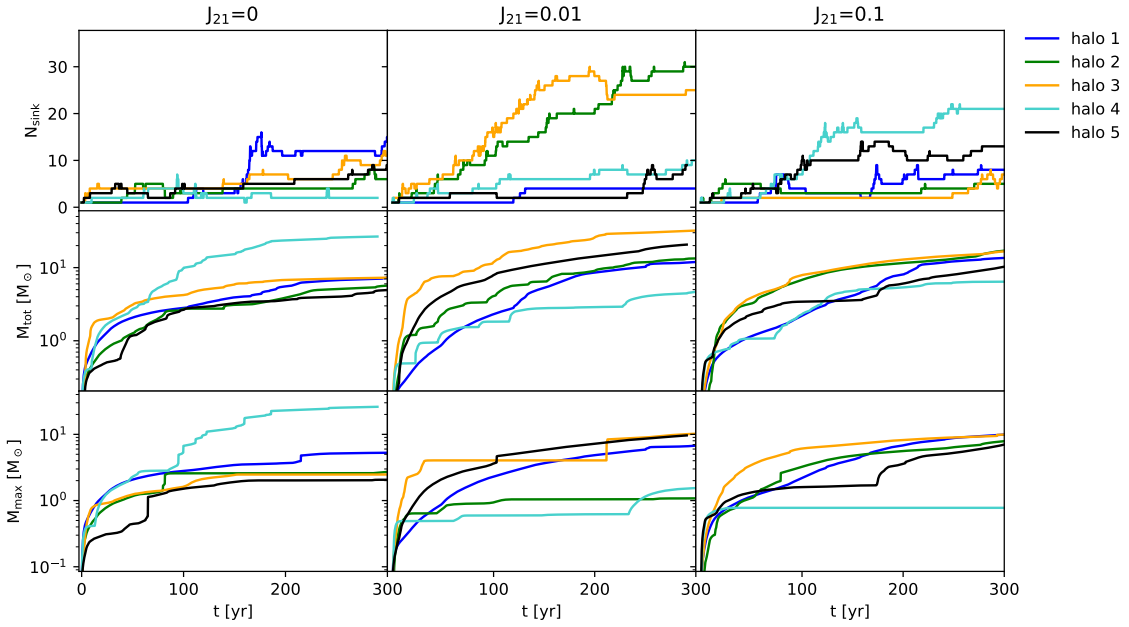

Figure 6.13. Number of sink particles formed, total mass in sinks and largest mass sink particle as a function of time.

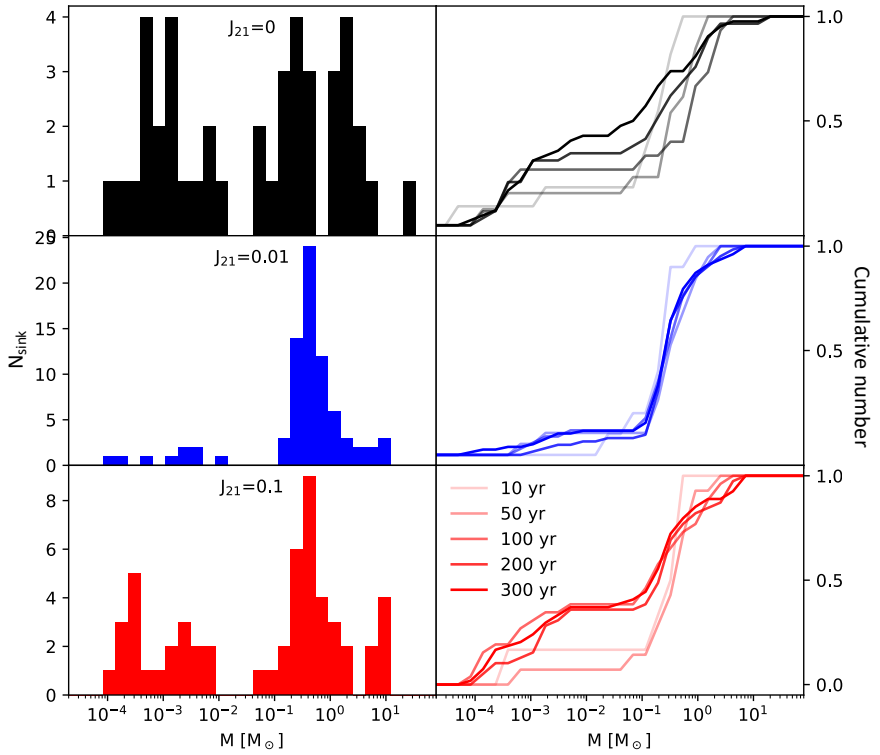

Figure 6.14. Left: combined IMFs of sink particles for the different the J_{21} values, Right: Cumulative IMFs of the combined sink particles for the different the J_{21} values.

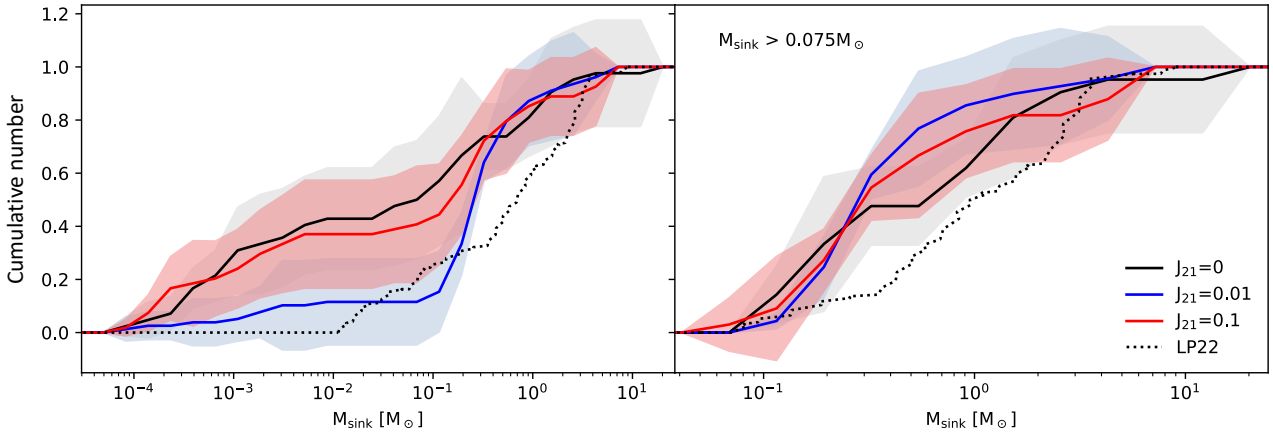

Figure 6.15. Left: Comparison of the cumulative IMFs at 300 yr after the formation of the first sink particle. Right: Cumulative IMFs ignoring brown dwarfs ($< 0.075\mathrm{M}_{\odot}$).

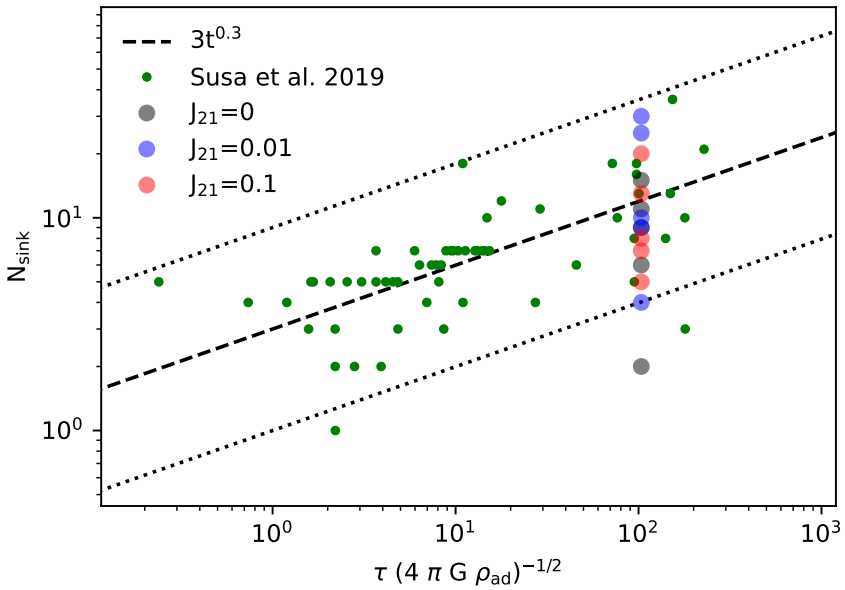

Figure 6.16. Comparison of the results of our study with the data of various studies collected in Figure 10 of Susa (2019). The number of sink particles formed is plotted verses time scaled as $\tau/\sqrt{4\pi G\rho_{\rm ad}}$. The thick dashed line shows the fit $\propto t^{0.3}$ and the dotted lines denote x3 and x1/3 of the thick dashed line.

The fields used in this study therefore represent the maximum effect Pop III stars can have on the the Pop III.2 stars that follow. Since the effects of the LW fields appear to be insignificant, it is likely that this result also represents the outcome for weaker fields.

The average halo mass from the $J_{21} = 0$ simulations of AS21 are a few times larger than that of Hirano et al. (2015). We assume this is due to the difference in self-shielding treatment, as Hirano et al. (2015) uses the Wolcott-Green et al. (2011) method. For example, an overestimation of self-shielding would result in an underestimation of photodissociation and hence a lower average mass of star forming halos. However, here we have shown that the IMF above the brown dwarf limit is invariant to halo mass.

We have assumed that the protostellar radius grows as Equation 6.1. This process begins immediately after sink particle formation. While this is predicted by stellar theory, it is unclear at what point the protostar would begin to expand, which may affect the accretion behaviour.

We have neglected the presence of primordial magnetic fields in this study. While the findings of Prole et al. (2022b) suggest that primordial magnetic fields make little difference to the primordial IMF due to their small-scale structure, the field is still active, with other recent studies finding that magnetic fields indeed lead to higher mass Pop III stars (e.g. Saad et al. 2022; Hirano &

Machida 2022; Stacy et al. 2022).

6.9 Conclusions

The results of cosmological simulations by AS21 show that increasing the background LW field strength increases the average halo mass required for star formation. These simulations ran up to a maximum density of 10^{-19} g cm^{-3}, hence the knock-on effects on the Pop III IMF were unclear. In this investigation, we have performed follow-up simulations of 5 halos for each of the $J_{21} = 0$, 0.01 and 0.1 LW field strengths, resolving the protostellar density of 10^{-6} g cm^{-3} before inserting sink particles and following the fragmentation behaviour for hundreds of years further. We have found that the mass accreted onto sinks by the end of the simulations is proportional to the mass within the $\sim 10^{-2}$ pc molecular core, which is not correlated to the initial mass of the halo. As such, the IMF shows little dependence on the LW field strength. We also find no clear relationship between the estimated accretion time of gas lying further out within the halo and the LW field strength, suggesting that the LW field is unlikely to influence the development of the IMF at later times. As the range of background LW field strengths tested here covers the most likely values from literature, we conclude that the IMF for so-called Pop III.2 stars is not significantly different from that of the initial population of Pop III.1 stars, although we cannot rule out greater effects in the small subset of halos that are illuminated by LW fields much stronger than the average value (see e.g Latif et al., 2014). In a future paper, we will explore the effects of increasing the streaming velocities between the gas and dark matter on the Pop III IMF, as this has been shown to increase halo masses through a different mechanism.

Chapter 7

Conclusion

The first stars formed within the gravitational potential well of dark matter halos at $z \sim 15$. They ionised the gas in their environments and chemically enriched the ISM with metals when they died as SN. Since observing Pop III stars is currently impossible, numerical simulations can increase our understanding of star formation and stellar properties in the early Universe. To that end, this thesis has presented a number of numerical experiments simulating the formation of Pop III stars, which will be summarised here.

7.1 Resolution criteria for Pop III simulations

The gravitational potential of DM halos facilitated the formation of the coolant H_2 within baryonic gas, allowing it to cool and collapse. The evolution of the collapse is dominated by the chemistry involved. The dominant chemical processes that complicate the collapse are three-body H_2 formation heating, collision-induced emission cooling and H_2 collisional dissociation. The collapse becomes adiabatic at the formation of the protostar at 10^{-4} g cm^{-3}, although this may happen at 10^{-6} g cm^{-3} if stellar feedback is considered (Machida & Nakamura, 2015). Due to the lack of dust and metals in the early Universe, the Jeans length continues to decrease as the gas collapses, all the way down to the formation of the protostar. This corresponds to an increase in density of 10 orders of magnitude from the first stellar core in present-day star formation when the gas becomes stable to fragmentation.

The Pop III IMF is disputed among authors but most recent studies agree that the gas fragments to form a group of stars within the halo. In Chapter 3 we performed a resolution study to show that these discrepancies are largely due to the difference in resolution adopted by these studies. We have shown that failure to resolve the Jeans length at the protostellar density (0.01-0.1 au)

results in underestimated fragmentation behaviour in the gas. The lower core masses that we produce when we increase our resolution effects how these stars interact with their environments through increased main sequence lifetimes, reduced contribution to reionisation, and ending their lives as Type II SN instead of pair-instability explosions. We also noted that a number of cores are ejected from the system with masses low enough that they should have survived until the present day, and may be observable. This raises questions into the pollution of Pop III stars with metals throughout their lifetimes as an explanation for the lack of Pop III observations.

7.2 Inclusion of magnetic fields in Pop III simulations

Magnetic fields have been shown to prevent fragmentation in present-day star formation simulations, increasing stellar masses. It is natural to expect that this may be the case in primordial star formation also. If this is the case, it would soften the resolution criteria discovered in Chapter 3. The main differences between magnetic fields in primordial times and the present day is their structure. The galactic magnetic field present today is uniform over the scales concerned with star formation. These highly ordered fields can provide a coherent magnetic tension force over large scales. Primordial magnetic fields go through the small-scale turbulent dynamo and are therefore expected to have small-scale structure described by a $k^{3/2}$ power spectrum, where the magnetic energy increases towards smaller spatial scales. Despite this, the magnetic pressure is isotropic and could therefore provide extra support against the fragmentation caused by gravitational collapse at Jeans scales at the highest densities.

7.2.1 Numerical tests

In order to assess the ability of small-scale primordial magnetic fields to reduce fragmentation in Pop III discs, we first performed a number of numerical tests throughout Chapter 4 to see what the most appropriate treatment of magnetic fields would be.

We first compared two methods of cleaning the $\nabla \cdot \vec{B}$ errors that arise in simulations. Namely the use of the Powell et al. (1999) scheme versus the more sophisticated Dedner et al. (2002) scheme. We used the same set-up as the simulations from Chapter 3 and let the gas collapse, amplifying the magnetic field through flux freezing and the small-scale turbulent dynamo. We found that Dedner terms yielded a $\sim 1\%$ divergence error while Powell terms gave a $\sim 10\%$ error accompanied by an increased amplification effect. We opted to use the Dedner terms moving forward as they gave a lower $\nabla \cdot \vec{B}$ error and a conservative estimate of field amplification.

As the addition of magnetic fields increases the computational cost significantly, we considered using a variable cleaning speed to reduce the computational cost. Inheriting the initial conditions of a magnetised cloud from Bürzle et al. (2011b), we performed a simple outflow/jet launching simulation. The variable cleaning speed resulted in an non-symmetric and non-physical breakdown of the outflow. We investigated this further by performing a test simulation inspired by Tricco & Price (2012) to find that the variable cleaning speed lead to a build up of artificial magnetic divergence when compared to a global cleaning speed. For this reason we opted to use the global cleaning speed moving forward despite the increase in computational cost.

Field amplification has been shown to be dependant on the adopted refinement criteria in AMR codes (Federrath et al., 2011a), which is very different to the unstructured mesh of AREPO. We therefore ran a series of simulations with the same initial conditions as Chapter 3, varying the refinement criteria from 16 to 128 cells per Jeans length. We found that indeed the amplification effect increased with the refinement criteria despite the difference in mesh technique. While the AMR study found that dynamo amplification could only occur for 32 cells per Jeans length, we found that field amplification above the flux freezing limit ($\rho^{2/3}$) occurred even in the 16 cell criteria run.

7.2.2 Pop III simulations

In Chapter 5 we investigated whether primordial magnetic fields could reduce Pop III disc fragmentation. Since amplification via the small-scale turbulent dynamo is dependent on resolution (which is inherently finite in simulations), we opted to bypass the amplification process and introduce a fully saturated (maximum strength) magnetic field late into a non-magnetised collapse. The field was introduced at a time before the disc formed to assess the ability of a tangled magnetic field to reduce disc fragmentation. We created the field by generating a random vector field from the $k^{3/2}$ power spectrum predicted by dynamo theory. Although these simulations were lower resolution than those presented in Chapter 3 we have shown that the small-scale fields do not reduce disc fragmentation or prevent the degree of fragmentation from increasing when the maximum density of the simulations is increased. As the inclusion of magnetic fields into these simulations greatly increased the computational cost without changing the results, we concluded that magnetic fields are not necessary in Pop III star formation simulations.

7.3 Effects of LW radiation on star formation

The radiation that Pop III stars emit interacts with their environments in different ways. Photons with energies above the hydrogen ionisation limit go towards forming a H_{II} region around the star, while photons below this limit are free to escape the halo and penetrate nearby halos. LW band photons photodissociate H_2 in nearby halos, preventing star formation until the halo gains sufficient mass through mergers so that the outer layers can self-shield the inner H_2 and form stars. While cosmological simulations have confirmed that the mass of halos required to form stars increases as the strength of the LW field is increased, these simulations lack sufficient resolution to resolve star formation within the halo. How the increasing halo masses affects the Pop III IMF is therefore unclear from cosmological simulations.

In Chapter 6 we performed zoom-in simulations around halos from the cosmological simulations of AS21, resolving the formation of the protostar and following the fragmentation of the gas for hundreds of years after. While the mass accreted onto sink particles by the end of the simulations was not correlated with initial mass of the halo or the mass of gas that managed to initially form enough H_2 to collapse, the accreted mass was correlated with the mass of the inner molecular core. Crucially, the mass of the molecular core was not correlated with the initial mass of the halo. The IMFs were almost identical across the LW field strengths, suggesting that the Pop III IMF may be invariant with halo mass and is therefore the same wherever we look in the early Universe, until the formation of Pop II stars.

7.4 Key Results

Throughout this work, a number of key findings have been presented. Here they will be stated concisely:

1) The lack of dust in primordial gas means that there is no first core in Pop III star formation. The collapse must therefore be simulated to much higher densities than present day star formation and hence requires higher spatial resolution. We have performed a resolution study for primordial chemistry and found that the degree of fragmentation increases as the maximum density of the simulation is increased, up to the protostellar density.

2) Higher degrees of fragmentation lead to lower Pop III core masses, accretion rates and output of ionising radiation, limiting their contribution to the re-ionisation of the Universe.

3) During the resolution test, a number of sub-solar mass Pop III cores were ejected from the system. These cores have the capacity to survive until the present day if they were cut off from

their accretion source.

4) Handling the cleaning of magnetic divergence errors with Dedner terms results in lower divergence errors than using Powell terms. This also results in lower field amplification via the turbulent dynamo.

5) Cleaning of magnetic divergence errors with a variable cleaning speed can produce non-physical results due to a build up of divergent field.

6) Previous findings that dynamo field amplification increases with increasing refinement criteria in grid codes holds true on the unstructured mesh of AREPO.

7) Under the assumption that primordial magnetic fields retain a $k^{3/2}$ power spectrum until shortly before the formation of Pop III discs, our simulations imply that they do not suppress fragmentation in primordial star formation or lead to more massive stars.

8) Photodissociation of H_2 by Lyman-Werner radiation produced by Pop III stars delays star formation in other halos until they can gain enough mass to self-shield the inner H_2, increasing the average star forming halo mass. Despite this, our high-resolution follow-up simulations of cosmological halos suggests that this does not effect the Pop III IMF.

7.5 FUTURE WORK

The results of Chapter 6 suggest that the Pop III IMF is independent of halo mass and is therefore universal until the formation of Pop II stars. This result is worth investigating further. Halo masses can also be increased in regions of higher streaming velocities between the gas and DM (see Section 1.3.9). The cosmological simulations of AS21 cover a parameter space of streaming velocities as well as LW radiation field strengths, showing that increased streaming velocities increases the average mass of star forming halos. Here the mass increases because the gravitational potential well of the DM halo needs to be greater to capture gas which now moves at relatively super-sonic speeds with respect to the DM. If the Pop III IMF is invariant to changes in halo mass due to this mechanism, it will provide supporting evidence that the Pop III IMF is universal.

An exception to the universal Pop III IMF may be found within atomically cooled halos (see Section 1.3.7). Here a strong LW field causes the gas to collapse isothermally at $\sim 10^4$ K via atomic cooling. The gas is thought to remain stable to fragmentation and collapse onto a single, central object capable of forming a DCBH. These DCBHs are theorised to explain high redshift quasar observations. However, previous studies have failed to implement high enough resolution to resolve whether this scenario results in fragmentation, running up to a maximum density of

10^{-14} g cm^{-3} (Johnson & Khochfar, 2011; Latif et al., 2013b; Regan et al., 2014; Schauer et al., 2017; Latif et al., 2020). In Chapter 3 we showed that fragmentation occurs up to the formation of the protostellar density at 10^{-6} g cm^{-3}, warranting high resolution simulations to confirm or deny whether DCBH formation is a feasible explanation for high redshifit quasar observations.

Bibliography

Abbott C D., 1982, The Astrophysical Journal, 259, 282

Abel T., Anninos P., Zhang Y., Norman M. L., 1997, New Astronomy, 2, 181

Abel T., Bryan G. L., Norman M. L., 2002, Science (New York, N.Y.), 295, 93

Abel T., Wise J. H., Bryan G. L., 2007, The Astrophysical Journal, 659, L87

Afrasiabi M., Klippel H., Roethlin M., Wegener K., 2021, Applied Mathematical Modelling, 100

Agarwal B., Khochfar S., 2015, Monthly Notices of the Royal Astronomical Society, 446, 160

Agarwal B., Khochfar S., Johnson J. L., Neistein E., Dalla Vecchia C., Livio M., 2012, Monthly Notices of the Royal Astronomical Society, 425, 2854

Agarwal B., Dalla Vecchia C., Johnson J. L., Khochfar S., Paardekooper J.-P., 2014, Monthly Notices of the Royal Astronomical Society, 443, 648

Agarwal B., Smith B., Glover S., Natarajan P., Khochfar S., 2016, Monthly Notices of the Royal Astronomical Society, 459, 4209

Agertz O., et al., 2007, Monthly Notices of the Royal Astronomical Society, 380, 963

Ahn K., Shapiro P. R., Iliev I. T., Mellema G., Pen U.-L., 2009, The Astrophysical Journal, 695, 1430

Alfvén H., 1942, Ark. f. Mat. Astro. o. Fysik 27A, N. 2. [§14.2, §14.5]

Allen A., Li Z.-Y., Shu F. H., 2003, The Astrophysical Journal, 599, 363

Alvarez M. A., Bromm V., Shapiro P. R., 2006, The Astrophysical Journal, 639, 621

Amati L., et al., 2018, Advances in Space Research, 62, 191

Bate M. R., Bonnell I. A., Price N. M., 1995, Monthly Notices of the Royal Astronomical Society, 277, 362

Beers T. C., Christlieb N., 2005,] 10.1146/annurev.astro.42.053102.134057, 43, 531

Berger M. J., Colella P., 1989, Journal of Computational Physics, 82, 64

Bertin G., Lodato G., 1999, A class of self-gravitating accretion disks, doi:10.48550/arXiv.astro-ph/9908095, http://arxiv.org/abs/astro-ph/9908095

Biermann L., 1950, Zeitschrift Naturforschung Teil A, 5, 65

Blandford R. D., Payne D. G., 1982, Monthly Notices of the Royal Astronomical Society, 199, 883

Bonnor W. B., 1956, Monthly Notices of the Royal Astronomical Society, 116, 351

Boss A., Bodenheimer P., 1979, The Astrophysical Journal, 234, 289

Bromm V., Loeb A., 2003, The Astrophysical Journal, 596, 34

Bromm V., Coppi P. S., Larson R. B., 1999, The Astrophysical Journal, 527, L5

Bromm V., Kudritzki R. P., Loeb A., 2001, The Astrophysical Journal, 552, 464

Bromm V., Coppi P. S., Larson R. B., 2002, The Astrophysical Journal, 564, 23

Bromm V., Yoshida N., Hernquist L., 2003, The Astrophysical Journal, 596, L135

Burgers J. M., 1948, in Von Mises R., Von Kármán T., eds, , Vol. 1, Advances in Applied Mechanics. Elsevier, pp 171–199, doi:10.1016/S0065-2156(08)70100-5, https://www.sciencedirect.com/science/article/pii/S0065215608701005

Burkert A., Bodenheimer P., 1993, Monthly Notices of the Royal Astronomical Society, 264, 798

Bürzle F., Clark P. C., Stasyszyn F., Greif T., Dolag K., Klessen R. S., Nielaba P., 2011a, Monthly Notices of the Royal Astronomical Society, 412, 171

Bürzle F., Clark P. C., Stasyszyn F., Dolag K., Klessen R. S., 2011b, Monthly Notices of the Royal Astronomical Society: Letters, 417, L61

Chon S., Omukai K., Schneider R., 2021, Monthly Notices of the Royal Astronomical Society, 508, 4175

Choudhuri A. R., 1998, The Physics of Fluids and Plasmas: An Introduction for Astrophysicists. Cambridge University Press, Cambridge, doi:10.1017/CBO9781139171069, https://www.cambridge.org/core/books/physics-of-fluids-and-plasmas/8A235D6F1D9DA51F05237D42BDFEFD06

Chuzhoy L., Kuhlen M., Shapiro P. R., 2007, The Astrophysical Journal, 665, L85

Clark P. C., Glover S. C. O., Smith R. J., Greif T. H., Klessen R. S., Bromm V., 2011a, Science, 331, 1040

Clark P. C., Glover S. C. O., Smith R. J., Greif T. H., Klessen R. S., Bromm V., 2011b, Science (New York, N.Y.), 331, 1040

Clark P. C., Glover S. C. O., Klessen R. S., 2012, Monthly Notices of the Royal Astronomical Society, 420, 745

Clarke C., Carswell B., 2007, Principles of Astrophysical Fluid Dynamics. Cambridge University Press

Collaboration T. E., et al., 2014, The Astrophysical Journal Supplement Series, 211, 19

Collaboration P., et al., 2020, Astronomy and Astrophysics, 641, A6

Collaboration T. C., et al., 2022, The Astrophysical Journal Supplement Series, 261, 29

Couchman H. M. P., Rees M. J., 1986, Monthly Notices of the Royal Astronomical Society, 221, 53

Courant R., Isaacson E., Rees M., 1952, Communications on Pure and Applied Mathematics, 5, 243

Cucchiara A., et al., 2011, The Astrophysical Journal, 736, 7

Dedner A., Kemm F., Kröner D., Munz C.-D., Schnitzer T. J., Wesenberg M., 2002. , doi:10.1006/jcph.2001.6961

Desch S. J., Mouschovias T. C., 2001, The Astrophysical Journal, 550, 314

Dijkstra M., Haiman Z., Mesinger A., Wyithe J. S. B., 2008, Monthly Notices of the Royal Astronomical Society, 391, 1961

Dove J. B., Shull J. M., Ferrara A., 2000, The Astrophysical Journal, 531, 846

Draine B. T., 2003, Annual Review of Astronomy and Astrophysics, 41, 241

Draine B. T., Bertoldi F., 1996, The Astrophysical Journal, 468, 269

Ebert R., 1955, ZAp, p. 217

Efstathiou G., Gratton S., 2020, Monthly Notices of the Royal Astronomical Society: Letters, 496, L91

Eisenstein D. J., Hu W., 1998, The Astrophysical Journal, 496, 605

Elmegreen B. G., 2000, The Astrophysical Journal, 539, 342

Federrath C., Banerjee R., Clark P. C., Klessen R. S., 2010, The Astrophysical Journal, 713, 269

Federrath C., Chabrier G., Schober J., Banerjee R., Klessen R. S., Schleicher D. R. G., 2011a, Physical Review Letters, 107, 114504

Federrath C., Chabrier G., Schober J., Banerjee R., Klessen R. S., Schleicher D. R. G., 2011b, Physical Review Letters, 107, 114504

Ferraro V. C. A., 1937, Monthly Notices of the Royal Astronomical Society, 97, 458

Field G. B., 1958, Proceedings of the IRE, 46, 240

Field G. B., Somerville W. B., Dressler K., 1966, Annual Review of Astronomy and Astrophysics, 4, 207

Franco J., Kurtz S., GarcÍa-Segura G., Hofner P., 2000, Astrophysics and Space Science, 272, 169

Frebel A., Norris J. E., 2015, Annual Review of Astronomy and Astrophysics, 53, 631

Fryer C. L., Woosley S. E., Heger A., 2001,] 10.1086/319719, 550, 372

Galli D., Palla F., 1998, Memorie della Societa Astronomica Italiana, 69, 337

Gammie C. F., 2001, The Astrophysical Journal, 553, 174

Ghirlanda G., et al., 2015, Monthly Notices of the Royal Astronomical Society, 448, 2514

Glover S. C. O., 2015, Monthly Notices of the Royal Astronomical Society, 451, 2082

Glover S. C. O., Abel T., 2008, Monthly Notices of the Royal Astronomical Society, 388, 1627

Glover S. C. O., Clark P. C., 2012, Monthly Notices of the Royal Astronomical Society, 421, 9

Glover S. C., Savin D. W., Jappsen A.-K., 2006, The Astrophysical Journal, 640, 553

Gould J. R., Gold T., Salpeter E E., 1963, he Astrophysical Journal, 138, 408

Greif T. H., Johnson J. L., Bromm V., Klessen R. S., 2007, The Astrophysical Journal, 670, 1

Greif T. H., Johnson J. L., Klessen R. S., Bromm V., 2008, Monthly Notices of the Royal Astronomical Society, 387, 1021

Greif T. H., White S. D. M., Klessen R. S., Springel V., 2011a, The Astrophysical Journal, 736, 147

Greif T. H., Springel V., White S. D. M., Glover S. C. O., Clark P. C., Smith R. J., Klessen R. S., Bromm V., 2011b, The Astrophysical Journal, 737, 75

Greif T. H., Bromm V., Clark P. C., Glover S. C. O., Smith R. J., Klessen R. S., Yoshida N., Springel V., 2012, Monthly Notices of the Royal Astronomical Society, 424, 399

Hahn O., Abel T., 2011, Monthly Notices of the Royal Astronomical Society, 415, 2101

Haiman Z., Thoul A. A., Loeb A., 1996a, The Astrophysical Journal, 464, 523

Haiman Z., Thoul A. A., Loeb A., 1996b, The Astrophysical Journal, 464, 523

Haiman Z., Rees M. J., Loeb A., 1997, The Astrophysical Journal, 476, 458

Haiman Z., Abel T., Rees M. J., 2000, The Astrophysical Journal, 534, 11

Hartwig T., Glover S. C. O., Klessen R. S., Latif M. A., Volonteri M., 2015a, Monthly Notices of the Royal Astronomical Society, 452, 1233

Hartwig T., Clark P. C., Glover S. C. O., Klessen R. S., Sasaki M., 2015b, The Astrophysical Journal, 799, 114

Hartwig T., Clark P. C., Glover S. C. O., Klessen R. S., Sasaki M., 2015c, The Astrophysical Journal, 799, 114

Haugen N. E. L., Brandenburg A., Dobler W., 2004, Physical Review E, 70, 016308

Heger A., Woosley S. E., 2002, The Astrophysical Journal, 567, 532

Heger A., Fryer C. L., Woosley S. E., Langer N., Hartmann D. H., 2003, The Astrophysical Journal, 591, 288

Heitmann K., et al., 2008, Computational Science and Discovery, 1, 015003

Hennebelle P., Ciardi A., 2009, Astronomy & Astrophysics, 506, L29

Hennebelle P., Fromang S., 2008, Astronomy & Astrophysics, 477, 9

Hennebelle P., Commerçon B., Joos M., Klessen R. S., Krumholz M., Tan J. C., Teyssier R., 2011, Astronomy & Astrophysics, 528, A72

Hirano S., Bromm V., 2017, Monthly Notices of the Royal Astronomical Society, 470, 898

Hirano S., Machida M. N., 2022, The Astrophysical Journal, 935, L16

Hirano S., Hosokawa T., Yoshida N., Umeda H., Omukai K., Chiaki G., Yorke H. W., 2014, The Astrophysical Journal, 781, 60

Hirano S., Hosokawa T., Yoshida N., Omukai K., Yorke H. W., 2015, Monthly Notices of the Royal Astronomical Society, 448, 568

Hirano S., Hosokawa T., Yoshida N., Kuiper R., 2017, Science, 357, 1375

Hosokawa T., Omukai K., 2009, The Astrophysical Journal, 691, 823

Hosokawa T., Omukai K., Yoshida N., Yorke H. W., 2011, Science, 334, 1250

Hosokawa T., Omukai K., Yorke H. W., 2012, The Astrophysical Journal, 756, 93

Hubble E., 1929, Proceedings of the National Academy of Sciences, 15, 168

Ichiki K., Takahashi K., Ohno H., Hanayama H., Sugiyama N., 2006, Science (New York, N.Y.), 311, 827

Jaura O., Magg M., Glover S. C. O., Klessen R. S., 2020, Monthly Notices of the Royal Astronomical Society, 499, 3594

Jaura O., Glover S. C. O., Wollenberg K. M. J., Klessen R. S., Finkelstein S., Haemmerlé L., 2021, Monthly Notices of the Royal Astronomical Society, submitted

Jaura O., Glover S. C. O., Wollenberg K. M. J., Klessen R. S., Geen S., Haemmerlé L., 2022, Monthly Notices of the Royal Astronomical Society, 512, 116

Joggerst C. C., Almgren A., Bell J., Heger A., Whalen D., Woosley S. E., 2009, The Astrophysical Journal, 709, 11

Johnson J. L., Khochfar S., 2011, Monthly Notices of the Royal Astronomical Society, 413, 1184

Kazantsev A. P., 1968, Soviet Journal of Experimental and Theoretical Physics, 26, 1031

Kimball D. F. J., Budker D., 2023, Introduction to Dark Matter, doi:10.1007/978-3-030-95852-7_1. , https://ui.adsabs.harvard.edu/abs/2023subd.book....1K

King A. R., Pringle J. E., Livio M., 2007, Monthly Notices of the Royal Astronomical Society, 376, 1740

Kippenhahn R., Weigert A., Weiss A., 2012, in , Stellar structure and evolution: , astronomy and astrophysics library. ISBN 978-3-642-30255-8. Springer-verlag berlin heidelberg, 2012, doi:10.1007/978-3-642-30304-3. , http://dx.doi.org/10.1007/978-3-642-30304-3

Kitayama T., Yoshida N., 2005, The Astrophysical Journal, 630, 675

Kitayama T., Yoshida N., Susa H., Umemura M., 2004, The Astrophysical Journal, 613, 631

Kogut A., Lineweaver C., Smoot G. F., Bennett C. L., Banday A., 1993, The Astrophysical Journal, 419, 1

Kolmogorov A. N., 1941, Equations of turbulent motion in an incompressible fluid

Kroupa P., 2001, Monthly Notices of the Royal Astronomical Society, 322, 231

Kroupa P., Jerabkova T., 2019, Nature Astronomy, 3, 482

Kulsrud R. M., 1990, Symposium - International Astronomical Union, 140, 527

Kulsrud R. M., Cen R., Ostriker J. P., Ryu D., 1997, The Astrophysical Journal, 480, 481

Larson R. B., 1969, Monthly Notices of the Royal Astronomical Society, 145, 271

Larson R. B., 1981, Monthly Notices of the Royal Astronomical Society, 194, 809

Latif M. A., Schleicher D. R. G., Schmidt W., Niemeyer J. C., 2013a, Monthly Notices of the Royal Astronomical Society, 436, 2989

Latif M. A., Schleicher D. R. G., Schmidt W., Niemeyer J., 2013b, The Astrophysical Journal, 772, L3

Latif M. A., Schleicher D. R. G., Bovino S., Grassi T., Spaans M., 2014, The Astrophysical Journal, 792, 78

Latif M. A., Khochfar S., Whalen D., 2020, The Astrophysical Journal, 892, L4

Laugier A., Garai J., 2007, Journal of Chemical Education, 84, 1832

Lepp S., Shull M J., 1984, The Astrophysical Journal, 280, 465

Li D., Zhu H.-M., Pen U.-L., 2019, Physical Review D, 100, 023517

Liu H., Outmezguine N. J., Redigolo D., Volansky T., 2019, Physical Review D, 100, 123011

Lodato G., 2007, La Rivista del Nuovo Cimento, pp 293–99999

Low C., Lynden-Bell D., 1976, Monthly Notices of the Royal Astronomical Society, 176, 367

Lynden-Bel D., 1967, Monthly Notices of the Royal Astronomical Society, 136, 101

Lynden-Bell D., 1996, Monthly Notices of the Royal Astronomical Society, 279, 389

Ma C.-P., Bertschinger E., 1995, The Astrophysical Journal, 455, 7

Machacek M. E., Bryan G. L., Abel T., 2001, The Astrophysical Journal, 548, 509

Machida M. N., 2014, The Astrophysical Journal, 796, L17

Machida M. N., Doi K., 2013, Monthly Notices of the Royal Astronomical Society, 435, 3283

Machida M. N., Nakamura T., 2015, Monthly Notices of the Royal Astronomical Society, 448, 1405

Machida M. N., Matsumoto T., Hanawa T., Tomisaka K., 2005, Monthly Notices of the Royal Astronomical Society, 362, 382

Machida M. N., Matsumoto T., Inutsuka S.-i., 2008, The Astrophysical Journal, 685, 690

Magg M., Hartwig T., Agarwal B., Frebel A., Glover S. C. O., Griffen B. F., Klessen R. S., 2018,] 10.1093/mnras/stx2729, 473, 5308

Magg M., Klessen R. S., Glover S. C. O., Li H., 2019, Monthly Notices of the Royal Astronomical Society, 487, 486

Marigo P., Girardi L., Chiosi C., Wood P. R., 2001, Astronomy & Astrophysics, 371, 152

Masson J., Chabrier G., Hennebelle P., Vaytet N., Commerçon B., 2016, Astronomy & Astrophysics, 587, A32

Matsuoka Y., et al., 2019, The Astrophysical Journal, 872, L2

Mazzali P. A., Röpke F. K., Benetti S., Hillebrandt W., 2007, Science, 315, 825

McCray R., Kafatos M., 1987, Mathematics, Physics, and Computer Science Faculty Articles and Research

McCullough P. R., 2000, Publications of the Astronomical Society of the Pacific, 112, 1542

Mellon R. R., Li Z.-Y., 2008, The Astrophysical Journal, 681, 1356

Merlin E., et al., 2022, The Astrophysical Journal Letters, 938, L14

Mestel L., 1963, Monthly Notices of the Royal Astronomical Society, 126, 553

Miniati F., Bell A. R., 2011, The Astrophysical Journal, 729, 73

Monaghan J. J., 1992, Annual Review of Astronomy and Astrophysics, 30, 543

Moore B., Quilis V., Bower R., 2000, 197, 363

Mortlock D. J., et al., 2011, Nature, 474, 616

Nakamura F., Umemura M., 2002, The Astrophysical Journal, 569, 549

Netterfield C. B., et al., 2002, The Astrophysical Journal, 571, 604

Nusser A., 2005, Monthly Notices of the Royal Astronomical Society, 359, 183

O'Shea B. W., Norman M. L., 2008, The Astrophysical Journal, 673, 14

Oh S. P., Haiman Z., 2002, The Astrophysical Journal, 569, 558

Omukai K., 2001, The Astrophysical Journal, 546, 635

Omukai K., Palla F., 2003, The Astrophysical Journal, 589, 677

Omukai K., Tsuribe T., Schneider R., Ferrara A., 2005, The Astrophysical Journal, 626, 627

Pakmor R., Bauer A., Springel V., 2011, Monthly Notices of the Royal Astronomical Society, 418, 1392

Pandey B. P., Wardle M., 2008, Monthly Notices of the Royal Astronomical Society, 385, 2269

Park J., Gillet N., Mesinger A., Greig B., 2020, Monthly Notices of the Royal Astronomical Society, 491, 3891

Peebles P. J. E., 1966, The Astrophysical Journal, 146, 542

Penzias A. A., Wilson R. W., 1965, Astrophysical Journal, 142, 1149

Peters T., Klessen R. S., Low M.-M. M., Banerjee R., 2010, The Astrophysical Journal, 725, 134

Powell K. G., Roe P. L., Linde T. J., Gombosi T. I., De Zeeuw D. L., 1999, Journal of Computational Physics, 154, 284

Price D. J., Bate M. R., 2007, Astrophysics and Space Science, 311, 75

Pringle J. E., 1981, Annual Review of Astronomy and Astrophysics, 19, 137

Prole L. R., Clark P. C., Klessen R. S., Glover S. C. O., 2022a, Monthly Notices of the Royal Astronomical Society, 510, 4019

Prole L. R., Clark P. C., Klessen R. S., Glover S. C. O., Pakmor R., 2022b, Monthly Notices of the Royal Astronomical Society, 516, 2223

Prole L. R., Schauer A. T. P., Clark P. C., Glover S. C. O., Priestley F. D., Klessen R. S., 2023, Monthly Notices of the Royal Astronomical Society, 520, 2081

Reed D. S., Bower R., Frenk C. S., Gao L., Jenkins A., Theuns T., White S. D. M., 2005, Monthly Notices of the Royal Astronomical Society, 363, 393

Regan J. A., Johansson P. H., Wise J. H., 2014, The Astrophysical Journal, 795, 137

Reis I., Fialkov A., Barkana R., 2020, Monthly Notices of the Royal Astronomical Society, 499, 5993

Ripamonti E., Abel T., 2004, Monthly Notices of the Royal Astronomical Society, 348, 1019

Ritter J. S., Safranek-Shrader C., Gnat O., Milosavljević M., Bromm V., 2012, The Astrophysical Journal, 761, 56

Saad C. R., Bromm V., El Eid M., 2022, Monthly Notices of the Royal Astronomical Society, 516, 3130

Salvadori S., Schneider R., Ferrara A., 2007,] 10.1111/j.1365-2966.2007.12133.x, 381, 647

Salvadori S., Ferrara A., Schneider R., Scannapieco E., Kawata D., 2010,] 10.1111/j.1745-3933.2009.00772.x, 401, L5

Schaerer D., 2002, Astronomy & Astrophysics, 382, 28

Schauer A. T. P., Regan J., Glover S. C. O., Klessen R. S., 2017, Monthly Notices of the Royal Astronomical Society, 471, 4878

Schauer A. T. P., Glover S. C. O., Klessen R. S., Ceverino D., 2019, Monthly Notices of the Royal Astronomical Society, 484, 3510

Schauer A. T. P., Drory N., Bromm V., 2020, The Astrophysical Journal, 904, 145

Schauer A. T. P., Glover S. C. O., Klessen R. S., Clark P., 2021, Monthly Notices of the Royal Astronomical Society, 507, 1775

Schive H.-Y., ZuHone J. A., Goldbaum N. J., Turk M. J., Gaspari M., Cheng C.-Y., 2018, Monthly Notices of the Royal Astronomical Society, 481, 4815

Schleicher D. R. G., Banerjee R., Sur S., Arshakian T. G., Klessen R. S., Beck R., Spaans M., 2010, Astronomy & Astrophysics, 522, A115

Schneider R., Salvaterra R., Ferrara A., Ciardi B., 2006, Monthly Notices of the Royal Astronomical Society, 369, 825

Schober J., Schleicher D., Federrath C., Klessen R., Banerjee R., 2012a, Physical Review E, 85, 026303

Schober J., Schleicher D., Federrath C., Glover S., Klessen R. S., Banerjee R., 2012b, The Astrophysical Journal, 754, 99

Schober J., Schleicher D. R. G., Federrath C., Bovino S., Klessen R. S., 2015, Physical Review E, 92, 023010

Seifried D., Banerjee R., Klessen R. S., Duffin D., Pudritz R. E., 2011, Monthly Notices of the Royal Astronomical Society, 417, 1054

Seifried D., Banerjee R., Pudritz R. E., Klessen R. S., 2013, Monthly Notices of the Royal Astronomical Society, 432, 3320

Seifried D., Banerjee R., Schleicher D., 2014, Monthly Notices of the Royal Astronomical Society, 440, 24

Shakura N. I., Sunyaev R. A., 1973, Astronomy and Astrophysics, 24, 337

Shang C., Bryan G. L., Haiman Z., 2010, Monthly Notices of the Royal Astronomical Society, 402, 1249

Sharda P., Federrath C., Krumholz M. R., 2020, Monthly Notices of the Royal Astronomical Society, 497, 336

Silk J., Langer M., 2006, Monthly Notices of the Royal Astronomical Society, 371, 444

Skinner D., Wise J. H., 2020, Monthly Notices of the Royal Astronomical Society, 492, 4386

Smidt J., Whalen D. J., Wiggins B. K., Even W., Johnson J. L., Fryer C. L., 2014, The Astrophysical Journal, 797, 97

Smidt J., Whalen D. J., Chatzopoulos E., Wiggins B., Chen K.-J., Kozyreva A., Even W., 2015, The Astrophysical Journal, 805, 44

Smith R. J., Glover S. C. O., Clark P. C., Greif T., Klessen R. S., 2011, Monthly Notices of the Royal Astronomical Society, 414, 3633

Spaans M., Silk J., 2006, The Astrophysical Journal, 652, 902

Springel V., 2005, Monthly Notices of the Royal Astronomical Society, 364, 1105

Springel V., 2010, Monthly Notices of the Royal Astronomical Society, 401, 791

Stacy A., Bromm V., 2013, Monthly Notices of the Royal Astronomical Society, 433, 1094

Stacy A., Greif T. H., Bromm V., 2010, Monthly Notices of the Royal Astronomical Society, 403, 45

Stacy A., Greif T. H., Bromm V., 2012, Monthly Notices of the Royal Astronomical Society, 422, 290

Stacy A., Pawlik A. H., Bromm V., Loeb A., 2014, Monthly Notices of the Royal Astronomical Society, 441, 822

Stacy A., Bromm V., Lee A. T., 2016, Monthly Notices of the Royal Astronomical Society, 462, 1307

Stacy A., McKee C. F., Lee A. T., Klein R. I., Li P. S., 2022, Monthly Notices of the Royal Astronomical Society, 511, 5042

Stahler S., Palla F., Salpeter E., 1986, The Astrophysical Journal,, 302, 90

Starkenburg E., et al., 2017, Monthly Notices of the Royal Astronomical Society, 471, 2587

Stecher T. P., Williams D. A., 1967, The Astrophysical Journal, 149, L29

Strömgren B., 1939, The Astrophysical Journal, 89, 526

Sugimura K., Omukai K., Inoue A. K., 2014, Monthly Notices of the Royal Astronomical Society, 445, 544

Sur S., Schleicher D. R. G., Banerjee R., Federrath C., Klessen R. S., 2010, The Astrophysical Journal, 721, L134

Susa H., 2019, The Astrophysical Journal, 877, 99

Susa H., Hasegawa K., Tominaga N., 2014, The Astrophysical Journal, 792, 32

Tanaka S. J., Chiaki G., Tominaga N., Susa H., 2017, The Astrophysical Journal, 844, 137

Tanikawa A., Suzuki T. K., Doi Y., 2018, Publications of the Astronomical Society of Japan, 70

Tanvir N. R., et al., 2009, Nature, 461, 1254

Tegmark M., Silk J., Rees M. J., Blanchard A., Abel T., Palla F., 1997, The Astrophysical Journal, 474, 1

Teyssier R., 2010, Astrophysics Source Code Library, p. ascl:1011.007

Tomida K., Tomisaka K., Matsumoto T., Hori Y., Okuzumi S., Machida M. N., Saigo K., 2012, The Astrophysical Journal, 763, 6

Toomre A., 1964, The Astrophysical Journal, 139, 1217

Trenti M., Stiavelli M., 2009, The Astrophysical Journal, 694, 879

Tress R. G., Smith R. J., Sormani M. C., Glover S. C. O., Klessen R. S., Mac Low M.-M., Clark P. C., 2020, Monthly Notices of the Royal Astronomical Society, 492, 2973

Tricco T. S., Price D. J., 2012, Journal of Computational Physics, 231, 7214

Tricco T. S., Price D. J., Bate M. R., 2016, Journal of Computational Physics, 322, 326

Truelove J. K., Klein R. I., McKee C. F., Holliman II J. H., Howell L. H., Greenough J. A., 1997, The Astrophysical Journal Letters, 489, L179

Tseliakhovich D., Hirata C., 2010, Physical Review D, 82, 083520

Tumlinson J., 2006,] 10.1086/500383, 641, 1

Tumlinson J., 2010,] 10.1088/0004-637X/708/2/1398, 708, 1398

Turk M. J., Clark P., Glover S. C. O., Greif T. H., Abel T., Klessen R., Bromm V., 2011, Astrophys.J.726:55,2011, 726

Vainshtein S. I., Zeldovich I. B., Ruzmaikin A. A., 1980, Moscow Izdatel Nauka

Vikaeus A., Zackrisson E., Schaerer D., Visbal E., Fransson E., Malhotra S., Rhoads J., Sahlén M., 2022, Monthly Notices of the Royal Astronomical Society, 512, 3030

Vink J. S., Koter A. d., Lamers H. J. G. L. M., 2001, Astronomy & Astrophysics, 369, 574

Visbal E., Haiman Z., Terrazas B., Bryan G. L., Barkana R., 2014, Monthly Notices of the Royal Astronomical Society, 445, 107

Wadsley J. W., Keller B. W., Quinn T. R., 2017, Monthly Notices of the Royal Astronomical Society, 471, 2357

Weibel E. S., 1959, Physical Review Letters, 2, 83

Whalen D., Abel T., Norman M. L., 2004, The Astrophysical Journal, 610, 14

Whalen D. J., Joggerst C. C., Fryer C. L., Stiavelli M., Heger A., Holz D. E., 2013a, The Astrophysical Journal, 768, 95

Whalen D. J., et al., 2013b, The Astrophysical Journal, 777, 110

White M., Krauss L. M., Silk J., 1993, The Astrophysical Journal, 418, 535

Wilson R. W., Penzias A. A., 1967, Science, 156, 1100

Wise J. H., Abel T., Turk M. J., Norman M. L., Smith B. D., 2012, Monthly Notices of the Royal Astronomical Society, 427, 311

Wolcott-Green J., Haiman Z., Bryan G. L., 2011, Monthly Notices of the Royal Astronomical Society, 418, 838

Wollenberg K. M. J., Glover S. C. O., Clark P. C., Klessen R. S., 2019, arXiv:1912.06377 [astro-ph]

Wollenberg K. M. J., Glover S. C. O., Clark P. C., Klessen R. S., 2020, Monthly Notices of the Royal Astronomical Society, 494, 1871

Wouthuysen S. A., 1952, The Astronomical Journal, 57, 31

Wurster J., Bate M. R., Price D. J., 2019, Monthly Notices of the Royal Astronomical Society, 489, 1719

Wurster J., Bate M. R., Bonnell I. A., 2021, Monthly Notices of the Royal Astronomical Society, 507, 2354

Yoshida N., Abel T., Hernquist L., Sugiyama N., 2003, The Astrophysical Journal, 592, 645

Yoshida N., Omukai K., Hernquist L., Abel T., 2006, The Astrophysical Journal, 652, 6

Yoshida N., Oh S. P., Kitayama T., Hernquist L., 2007a, The Astrophysical Journal, 663, 687

Yoshida N., Omukai K., Hernquist L., 2007b, The Astrophysical Journal, 667, L117

Yoshida N., Omukai K., Hernquist L., 2008, Science (New York, N.Y.), 321, 669

Zackrisson E., Rydberg C.-E., Schaerer D., Östlin G., Tuli M., 2011, The Astrophysical Journal, 740, 13

Zwicky F., 1933, Helvetica physica acta, 6, 110

de Bernardis P., et al., 2001, AIP Conference Proceedings, 555, 85